Investigating Transport of Ethanol within Hydrocarbon Anion Exchange Membranes for CO_2 Electrolysis

by

Jacob Ronen Keffer

B.Sc. (Hons.), McMaster University, 2021

Thesis Submitted in Partial Fulfillment of the
Requirements for the Degree of
Master of Science

in the
Department of Chemistry
Faculty of Science

SIMON FRASER UNIVERSITY
Spring 2024

Declaration of Committee

Name:	**Jacob Ronen Keffer**
Degree:	**Master of Science (Chemistry)**
Title:	**Investigating Transport of Ethanol within Hydrocarbon Anion Exchange Membranes for CO_2 Electrolysis**
Committee:	**Chair:** **Paul Li** Professor, Chemistry
	Steven Holdcroft Supervisor Professor, Chemistry
	Roger Linington Committee Member Professor, Chemistry
	Jeffrey Warren Committee Member Associate Professor, Chemistry
	Byron Gates Examiner Professor, Chemistry

Abstract

A kilowatt-hour produced using renewable energy is rapidly becoming cheaper than equivalent fossil fuel energy production methods. Simultaneously, CO_2 capture technologies are approaching commercialization and are projected to give industry access to a surplus of CO_2. What should be done with abundant clean energy and CO_2? CO_2 electrolysis could be the answer; it is a promising technology that creates commodity chemicals like ethanol, methanol, ethylene, and formic acid from CO_2. Several inefficiencies need to be addressed to advance the technology to commercial relevancy. Within alkaline CO_2 electrolysers, newly formed products diffuse into and across the anion exchange membrane, which is shown to negatively effect the membrane. Five hydrocarbon membranes were compared giving insight into how effectively different membrane chemistries exclude ethanol. Diffusion-ordered spectroscopy and permeability tests were used for measuring the diffusion coefficients of ethanol within these membranes. Crosslinking and zwitterionic functional groups showed potential to abate ethanol diffusion.

Keywords: CO_2 Electrolysis; Anion Exchange Membrane; Diffusion; Permeability; Product Crossover

Dedication

I wish to dedicate my thesis to my grandfather. He was an incredible person and I miss him dearly. He was my inspiration for my love of chemistry. I remember many fun science experiments with him as a child. He worked as a polymer chemist in research and development at Goodyear for over 35 years. My grandfather moved from Israel to the US with his wife at an early age to pursue his master's and PhD in chemistry. He had no family there and his father disapproved of his choices. He faced many hardships through the years and is an inspiration to me. I miss him dearly and love him very much.

Acknowledgements

This work was not possible without help from several colleagues. Dr. Simon Cassegrain synthesized the zwitterion-functionalized HMT-PMBI 75% dm 25% dz that was used for the permeability measurements and tensile measurements. Lucas Clarke, the in-house glass blower, constructed the H-cell, with which the permeability tests would not be possible. All HMT-PMBI 75% dm and HMT-PMBI 89% dm was synthesized by Dr. Andrew Wright. Dr. Marina Bauer and Dr. Alessandra Menandro instructed and gave feedback on the IEC measurements presented. Dr. Torben Saatkamp contributed with many intellectual conversations and troubleshooting that improved understanding of data and methods. Dr. Eric Ye, the NMR facility manager was integral in managing the NMR spectroscopy equipment used and helped modify the W5 water suppression experiment specifically for this project. Dr. Peter Mardle was the first colleague to introduce me to the project and helped to get the process going. Lastly, I acknowledge all the helpful discussions and support from the entire Holdcroft group and Professor Steven Holdcroft for supervising this thesis.

Table of Contents

List of Tables

List of Figures

List of Acronyms and Abbreviations

% df	Percent degree of functionalization
% dm	Percent degree of methylation
% dx	Percent degree of cross-linking
% dz	Percent degree of zwitterionification
ACS	American Chemical Society
AEM	Anion Exchange Membrane
C_1	Molecule containing 1 carbon atom
C_2	Molecule containing 2 carbon atoms
C_3	Molecule containing 3 carbon atoms
CCUS	Carbon Capture Utilization and Storage
CEM	Cation Exchange Membrane
CO_2	Carbon Dioxide
CO_2E	Carbon Dioxide Electrolysis
CO_2R	Carbon Dioxide Reduction
D1	Delay time between repeat NMR experiments
DCX	α,α'-Dichloro-p-xylene
DOSY	Diffusion Ordered SpectroscopY
GDL	Gas Diffusion Layer
HER	Hydrogen Evolution Reaction
HMT	2,2”,4,4”,6,6”-hexamethyl-p-terphenyl-3,3”-diyl
HMT-PMBI	Poly(methylated)[2,2’-(2,2”,4,4”,6,6”-hexamethyl-p-terphenyl-3,3”-diyl)-5,5’-bibenzimidazole]
IEC	Ion Exchange Capacity
IEM	Ion Exchange Membrane
IPCC	Intergovernmental Panel on Climate Change
IPS	In-Plane Swelling
IRENA	International Renewable Energy Agency
LCOE	Levelized Cost Of Electricity
MEA	Membrane Electrode Assembly
NMR	Nuclear Magnetic Resonance

OER	Oxygen Evolution Reaction
PAA	Polyacrylic acid
PBI	Polybenzimidazole
PDMBI	Poly(N1,N3-dimethylbenzimidazolium)
Peakw	Peak width function in TopSpin
PFG	Pulsed Field Gradient
PTFE	Polytetrafluoroethylene
PVDF	Polyvinylidene fluoride
RE	Renewable Energy
SPAES	sulfonated poly(aryl ether sulfone)
SPEEK	sulfonated poly(ether ether ketone)
SU	Solvent Uptake
T_1	Magnetization relaxation constant
TPS	Through-Plane Swelling
WATERGATE	Water Gradient Tailored Excitation
Wt%	Weight percent
WU	Water Uptake

Chapter 1. Introduction

1.1. Motivation

Carbon dioxide (CO_2) is the most produced greenhouse gas by mass and has been identified as the main contributor to the warming of Earth.[1–4] This gas is produced and consumed via the CO_2 cycle, which has begun to fall out of balance since the onset of the industrial revolution.[5–7] CO_2 emission is a metric that countries all over the world are using to determine their contribution to the global carbon cycle. Many of these countries have adopted "net-zero" goals, which give timeframes during which a country intends to reduce its carbon emissions to match its carbon consumption. Canada has a net-zero goal for 2050 and has reviewed available technologies to reach this goal and classified them as "safe bets" and "wildcards".[8] These classifications describe whether a technology is well established and understood and is nearly ready for commercialization or are high risk, high reward technologies, respectively. The Canadian government has asserted that the most effective policy towards closing the carbon cycle is to use many technologies to attack the problem using a diverse collection of technologies.

The affordability of sustainable energy generation technologies such as photovoltaic solar energy, concentrating solar power, offshore wind turbines, and onshore wind turbines has already surpassed, or is soon set to surpass equivalent fossil fuel energy, shown in **Figure 1**.[9] Despite the steadily increasing adoption rate of these affordable energy alternatives[10], two major obstacles remain on the path to net-zero: How are we meant to store massive amounts of excess energy, which is often intermittent, to ensure continuous power? How do we negate carbon emissions from sectors that produce greenhouse gases regardless of being powered by carbon neutral energy? Energy storage and conversion devices could be the answer.

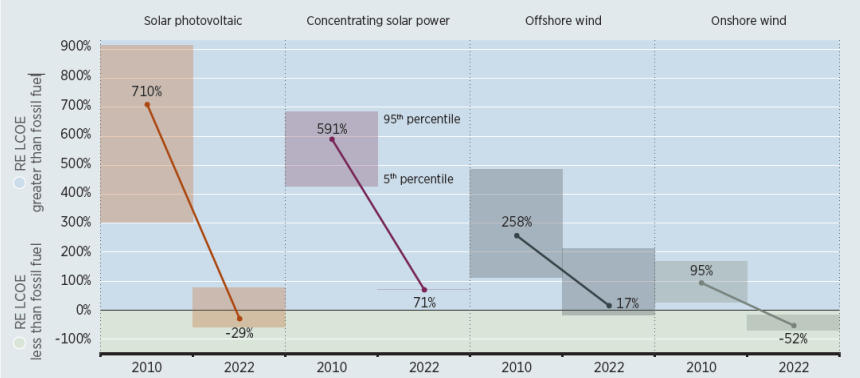

Figure 1. Comparison of the cost of renewable energy (RE) sources from 2010 to 2022, presented in percent relative to the global weighted-average levelised cost of electricity (LCOE). Reprinted from the Renewable Power Generation Costs in 2022 report by the International Renewable Energy Agency (IRENA).[9]

Energy storage and conversion technologies such as grid-scale batteries[11] are starting to come online and factories for grid-scale water electrolysers and fuel cells[12] are being built in North America. These massive projects are set to transform nation-wide energy storage in the coming decades, and research is continuously improving these technologies while simultaneously decreasing operating costs. Despite this, there are a large percent of current CO_2 emitting sectors such as manufacturing, chemicals industry, mining, and cement, that are classified as "hard-to-abate" emission sources. There is no guarantee that innovations to transform these sectors will ever occur, or that they can be adopted in a reasonable time frame and at acceptable costs.

Despite the development and adoption of less emissive power generation methods, manufacturing methods, and industrial practices, CO_2 production will persist in many sectors and will continue to be a waste product that is emitted into the atmosphere. It is likely that many current industries will be unable to transition to net-zero emissions by Canada's 2050 goal. One group of technologies that can help Canada meet its goal is CO_2 capture, utilisation, and storage (CCUS). The basic principle of CCUS is shown in **Figure 2**, where renewable energy and CO_2 captured from industry is converted to commodity chemicals in a CO_2 electrolyser. These products are then fed back into industry.

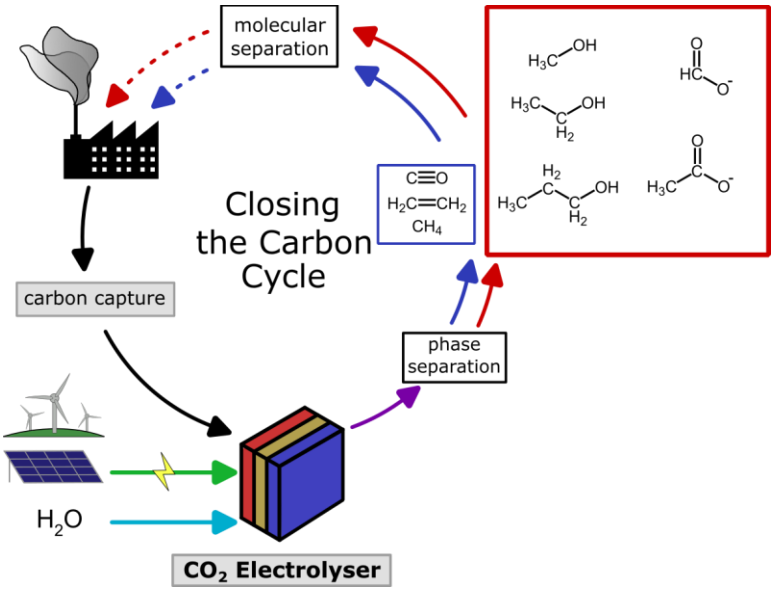

Figure 2. **A simplified schematic of how CO_2 electrolysis can be used to close the carbon cycle in an industry.**

1.2. CO_2 Capture, Utilization, and Storage (CCUS)

Canada has identified CCUS as both a "safe bet" and a "wildcard". This is due to two main factors: 1) CCUS can be applied to concentrated sources of CO_2 (such as flue gas, power generation exhaust, etc.) or to dilute sources of CO_2 (mainly from the atmosphere). CCUS technology is currently much more suited to be used for concentrated sources (which is the safe bet). 2) CCUS technology is separated by the three steps of capture, storage, and utilisation, which are all achieved by very different processes. CO_2 utilisation is a complex technology that is gaining interest rapidly but is still in its infancy, while CO_2 capture is more complex, but is also more advanced. CO_2 storage is simple and has been commercialised, and solutions for long-term storage already exist.

CCUS is an adaptable solution to closing the carbon cycle in a variety of industries, as the only prerequisite for using the technology is the emission of CO_2. This presents a huge advantage of more specific carbon emission reduction technologies, especially for industries that are hard-to-abate emission sources. Highly emissive processes that are critical to the global economy and have become integral to human existence (like the Haber-Bosch process, Petroleum cracking processes, Chlor-alkali process, and others) are excellent candidates for CCUS. As it stands, CCUS is set to be a scalable technology that can be tailored to an industry's emissions.

The Intergovernmental Panel on Climate Change (IPCC) 2005 Special Report of Carbon Dioxide Capture and Storage[13] defines CO_2 utilization as the use of CO_2 at concentrations above atmospheric levels, directly as a feedstock in industrial or chemical processes, to produce valuable carbon-containing products. There are many methods for the utilization of concentrated CO_2, ten of which are outlined in detail by Hepburn *et al*.[14] The ten pathways towards CO_2 utilization reviewed include 1) Chemicals from CO_2, 2) Fuels from CO_2, 3) Products from microalgae, 4) Concrete building materials, 5) CO_2 enhanced oil recovery, 6) Bioenergy with carbon capture and storage, 7) Enhanced weathering, 8) Forestry techniques, 9) Soil carbon sequestration techniques, and 10) Biochar. Of these techniques, 1) Chemicals from CO_2 and 2) Fuels from CO_2 present adaptable and scalable technologies that can be tailored to a specific industry. Both technologies are electrocatalytic processes that reduce CO_2 to chemical products and fuels such as methanol, ethanol, formic acid, methane, ethylene, urea, etc. These products can be used as either chemical feedstocks or as a form of long-term energy storage. The electroreduction of CO_2 is colloquially known as CO_2 reduction (CO_2R) or CO_2 electrolysis (CO_2E). While CO_2 reduction is not a misnomer, the term could also imply the reduction of CO_2 emissions, therefore CO_2 electrolysis will be used for the remainder of this thesis to avoid confusion.

1.3. Explanation of State-of-the-Art CO_2 Electrolysis (CO_2E)

CO_2E is achieved using an electrolyser, which is specifically designed for high efficiency towards the production of a target molecule or molecules. A simple diagram of an electrolyser is shown in **Figure 3**. Many products of the electroreduction of CO_2 have been demonstrated in literature. The difficulty of synthesizing a certain CO_2E product is tied to the number of carbon atoms that must be reduced in sequence. Referred to as C_1 products, carbon monoxide, methane, formic acid, and methanol represent the most common, and thermodynamically favorable CO_2E products. C_2 products include, ethylene, ethanol, and acetate, and C_3 products include n-propanol represent higher value, but more energy-intensive CO_2E products.

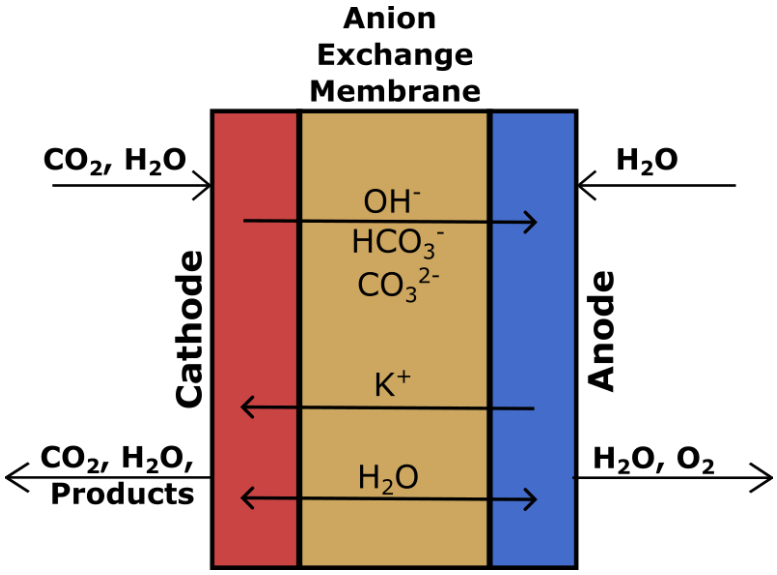

Figure 3. A simple graphic of a CO_2 electrolyser, showing the flow of major reactants, products, and dissolved ions.

While many molecules have been demonstrated as potential products for CO_2E, there are several that are most favorable for a variety of reasons. The motivation behind designing an electrolyser for a specific target product is directly related to the energetic and faradaic efficiency towards that product, and the potential market value of that product.

1.3.1. Target Products and their Economic Importance (or Potential Market Value)

While many possible products of CO_2E exist and have been demonstrated in literature, research currently focuses on those with high market value potential and low energy cost. Several in-depth techno-economic analyses[15–17] highlight the most valuable of the accessible CO_2E products, namely: carbon monoxide, ethylene, methanol, ethanol, n-propanol, methane, formic acid, formaldehyde, and acetic acid. Each product is valuable in different end-use markets. The two main markets that could utilize CO_2E are industrial feedstocks and energy dense fuels. Of the mentioned CO_2E products, alcohols and methane are prime candidates for use as energy dense fuels for energy storage, while ethylene, carbon monoxide, and formic acid present a higher value as commodities for the chemical industry. The balanced reactions for the most common commodity chemicals produced in literature are shown in **Table 1**, with their respective reduction potentials versus the hydrogen evolution reaction (HER).

Table 1. **The standard reduction potentials of seven common CO_2E products and their balanced electrochemical half-cell reactions, all compared to the standard hydrogen electrode.**

BALANCED ELECTROCHEMICAL REACTION	REDUCTION POTENTIALS VS THE HER (V)
$CO_2(g) + 8H^+ + 8e^- \leftrightarrows CH_4(g) + 2H_2O(l)$	+0.169
$3CO_2(g) + 18H^+ + 18e^- \leftrightarrows CH_3CH_2CH_2OH(l) + 5H_2O(l)$	+0.095
$2CO_2(g)\ 12H^+ + 12e^- \leftrightarrows CH_3CH_2OH(l) + 3H_2O(l)$	+0.084
$2CO_2(g) + 12H^+ + 12e^- \leftrightarrows CH_2CH_2(g) + 4H_2O(l)$	+0.064
$CO_2(g) + 6H^+ + 6e^- \leftrightarrows CH_3OH(l) + H_2O(l)$	+0.016
$2H^+ + 2e^- \leftrightarrows H_2(g)$	0.000
$CO_2(g) + 2H^+\ 2e^- \leftrightarrows CO(g) + H_2O(l)$	-0.106
$CO_2(g) + 2H^+ + 2e^- \leftrightarrows HCOOH(l)$	-0.250

While longer chain alcohols provide a higher energy density by mass, they require more catalyzed electron transfers. If the energy densities of alcohols are normalized by the number of electrons needed, the normalized energy density falls rapidly. The motivation behind normalized energy density comes from the fact that energy is an input which must be used efficiently. This normalization allows one to compare alcohol energy density while taking into account the base input energy to create them. Only the synthesis of methanol and ethanol have a net-positive normalized energy density.[15] The synthesis of n-propanol has a slightly net-negative normalized energy density. This implies methanol and ethanol are the only alcohols that yield a net positive

energy return as CO_2E products for fuel use. The formation of ethanol requires two sets of sequential catalyzed proton-coupled electron reactions to occur. The faradaic efficiency towards ethanol is a mere 60%, compared to 90% for methanol, when using state-of-the-art catalysts.[15] This indicates that until high efficiency catalysts become available, methanol is the prime target for energy storage in the form of chemical bonds.

Making chemical feedstocks for industry has been projected to be a market with high potential upon the adoption of CO_2E technology. Industries could reduce their carbon emissions by incorporating CO_2 capture and electrolysis stations on-line. This market would capitalize on the electroreduction of CO_2 to ethylene, carbon monoxide, formic acid, and acetate as building blocks for industrial synthesis.

Figure 4 shows that, of the products discussed, methane produced via electrolysis is the only one which can cannot currently match market prices. This "break-even" point is the strongest motivator for commercial adoption of CO_2E. According to technoeconomic analyses, the market price for methane is far too low in comparison to the cost to produce methane from CO_2. There is little motivation at this time to produce methane due to its commercial abundance.

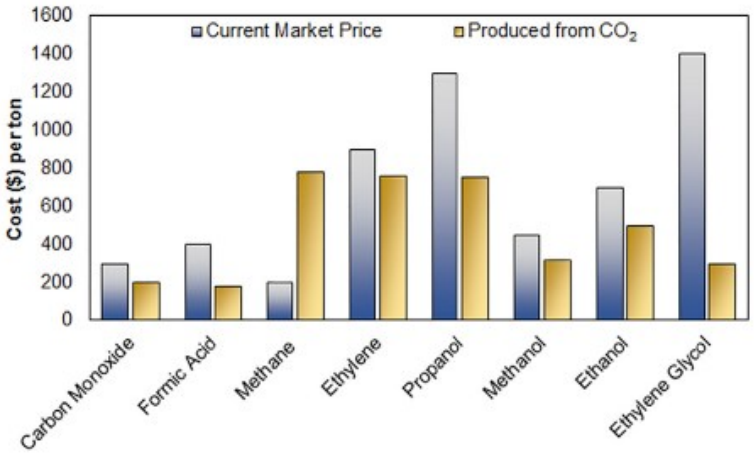

Figure 4. A comparison of the costs of CO_2E products sourced from both electrolysis and the commercial market. This comparison assumes an energy conversion efficiency of 60%, Faradaic efficiency of 90%, electricity cost of 2 ¢/kWh, CO_2 cost of 30 $/ton and an electrolyser cost of 500 $/kW. Reprinted with permission from publisher.[15]

1.3.2. Electrolyser Design and Components

CO_2 electrolysers come in many configurations; however, all possess similar components that are required to electrochemically reduce CO_2. These components are of great interest to materials scientists, as the efficiency of the cell is always dependent on the sum of its parts. Detailed assessments of available designs can be found in literature.[18,19] Here, only anion exchange membrane (AEM)-based membrane electrode assembly (MEA)-type cells are considered. Comprehensive reviews could be written about each component alone, but herein, the focus will be to give a detailed description of the purpose of each component and give examples of materials currently being investigated for each. Below, in **Figure 5**, an example of an AEM-based MEA-type cell is presented. The most relevant components will be discussed in the following text.

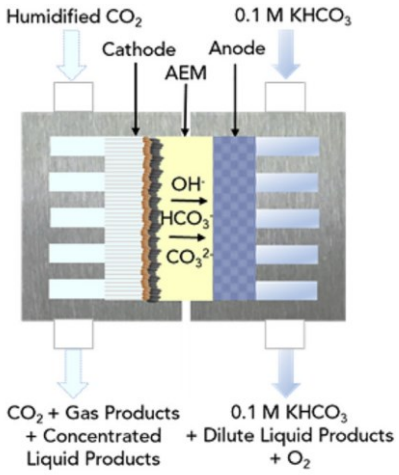

Figure 5. A diagram of an MEA-type CO_2 electrolyser, the curent state-of-the-art electrolyser design. Figure reused with permission from the publisher.[20]

The Cathode

The first component discussed, often referred to as the working electrode, is the cathode. Electrons are delivered to the electrolyser via the cathode, which then facilitates the reduction of CO_2. Therefore, the cathode layer must be electrically conductive, must manage the influx of reagents (CO_2 and water) to catalytic sites efficiently, and allow the outflux of reaction products. Cathodes are often made by finely dispersing catalyst onto a support with a large surface area. These particles are usually held in place with a polymer binder that is permeable to gas and liquid, so that reactants can reach the catalyst. This combination of a high surface area substrate, efficient catalyst, optimal binder loading, and optionally: conductive additives and/or an ionomer

layer to help with the conduction of electrons and ions to catalyst sites, makes up a state-of-the-art cathode layer.

The common choices for a substrate with high surface area are metal foams, carbon papers, and hydrophobic polymer supports. This substrate allows gas to diffuse through, thereby supplying the cathode with continuous access to CO_2. The most common name for this substrate is the gas diffusion layer (GDL).[21] Metal foams and carbon paper are the most common materials. Metal foams are conductive and provide robust structural integrity. Carbon papers are conductive and can possess a higher density of pores and smaller pores, leading to a potential higher internal surface area.[22] Hydrophobic polymer supports using polytetrafluoroethylene (PTFE) have been employed to great success as they are able to encourage enhanced gas diffusion.[23,24]

The most common catalysts used for efficient and selective reduction of CO_2 at the cathode are copper, silver, gold, platinum, tin, and lead.[25,26] Research in using copper and silver is growing for opposing reasons, catalyst promiscuity and selectivity, respectively. Copper has been shown to be active towards many different valuable products, allowing for a diverse range of compounds to be produced, giving commercial users of this technology a range of options to adapt an electrolyser to their needs. While silver is highly selective towards producing carbon monoxide, offering higher faradaic efficiency towards the gaseous product.

Silver and copper are good catalysts for groups that are studying more than just the catalyst layer. It is advantageous to test membranes, electrolyte composition, catalyst layer additives, or novel cell design with both copper and silver. Having consistent catalysts that offer relatively high efficiency towards a single gaseous product or multiple liquid products allows for a more comprehensive study.

Many electrochemical devices including batteries, fuel cells, and electrolysers employ ionically conductive binders to hold catalyst particles to the chosen substrate. The most common binders used in CO_2 electrolysers are Nafion®, (PTFE), polyvinylidene fluoride (PVDF), and polyacrylic acid (PAA), although several others exist.[27–29] Many studies have outlined the critical balance of hydrophobicity and hydrophilicity afforded by binders in cathode layers. This balance achieves necessary management of gas, water, and ions to active catalyst sites.

This balancing act is crucial in sustaining what is commonly referred to as the “triple-phase boundary”. The underlying theory to efficiently reduce CO_2 requires each catalyst site to

have unobstructed access to gaseous CO_2 and water. However, having too much of either results in inactive catalyst, known as drying and flooding of the cathode, respectively.

The Anode

The anode in a CO_2 electrolyser is similar to the cathode, but strictly facilitates the oxygen evolution reaction (OER) similar to water electrolysers, shown in **Equation 1**. Like in many water electrolysers, iridium is a common catalyst for use in the anode. The construction of the anode does not require a triple-phase boundary but does require that generated oxygen escapes quickly and does not occupy pore spaces, thereby obstructing catalyst sites.

$$4OH^- \rightarrow 2H_2O + O_2 + 4e^-$$

Equation 1. The balanced reaction of hydroxide to water and oxygen that occurs at the anode of an alkaline CO_2 electrolyser.

Liquid Electrolyte

Liquid electrolyte is used in conjunction with a solid electrolyte in all room temperature electrolysers. The most common electrolytes for AEM-based MEA-type electrolysers are aqueous KOH, $KHCO_3$, KCl, and K_2SO_4. Interestingly, electrolyte composition is quite important to the efficiency of electrocatalysts and does not simply operate as a charge carrier. Similar to batteries and electrocatalysis devices, the purity of the electrolyte in CO_2E is critical to selectivity of the catalyst and the lifetime of the device. Several studies have demonstrated that pre-electrolysis[30] to remove impurities in the electrolyte, or catalyst regeneration[31] can be used to remedy this issue.

A common issue with current CO_2 electrolysers is the carbonation of aqueous electrolyte. While the dissolution of CO_2 is a necessary step to perform CO_2E, the dissolved CO_2 reacts with water to form carbonic acid (H_2CO_3), this then reacts with hydroxide in the electrolyte to form bicarbonate (HCO_3^-). Due to the high operating pH of alkaline electrolysers, this bicarbonate is converted to carbonate (CO_3^{2-}) through the bicarbonate/carbonate equilibrium. Both bicarbonate and carbonate displace counterions in the polymer electrolyte that are critical to high efficiency electrolysers.[32] Despite the persistence of this issue, for the purposes of this study, only bicarbonate/carbonate systems are considered. Using $KHCO_3$ decreases complexity as the carbonation of the membrane is inevitable with current technology. This issue has been highlighted in literature as a key challenge to overcome.[33] Part of the motivation behind development of GDLs was to reduce the rate at which CO_2 dissolves into the liquid electrolyte.

Polymer Electrolyte

At the heart of the CO_2 electrolyser is the polymer electrolyte, also known as the Ion Exchange Membrane (IEM), typically comprised of polymer, which is electrically insulative, but freely conducts ions. IEMs have fixed charge groups either on the main polymer chain or on sidechains. A counter-ion balances this fixed charge. If the polymer chain has anionic fixed charges it is known as a cation exchange membrane (CEM); conversely, if the polymer chain has cationic fixed charges it is known as an anion exchange membrane (AEM). The word *exchange* is specifically used as these polymers have a unique property known as selective permeability. For example, an AEM has a fixed positive charge and negative counter-ion, which can disassociate when a compatible solvent is able to solvate the counter-ion. The membrane conducts ions of the same charge as the counterions. This conduction occurs via several possible mechanisms that all contribute to overall transport of counter-ions through the membrane. This property makes IEMs critical in technologies in many sectors that rely on the separation of ions from an aqueous environment. Some technologies outside of energy storage and conversion include electrodialysis, membrane distillation, water purification, and chlor-alkali production.

The high pH used in AEM-based alkaline electrolysers has been shown to suppress the hydrogen evolution reaction (HER). Suppressing the HER is critical to maximizing faradaic efficiency towards the desired CO_2E product. The HER is reduced by two orders of magnitude in highly alkaline environment, relative to its rate in acidic media.[34–36] High operating pHs have been detrimental to hydrocarbon based AEMs, which often degrade within hours. Membranes such as Selemion AMV possess pendant quaternary amines, which readily go under nucleophilic attack by hydroxide. This instability poses a massive challenge towards realizing hydrocarbon AEM-based alkaline electrolysers. Herein, a highly stable benzimidazolium-based AEM which enables highly-alkaline electrolyser research is discussed. This polymer was developed over nearly a decade and is still being improved upon, a brief history of its inception follows.

There are several key characteristics that are used to describe membranes. The characteristics that are most relevant for this work are ion exchange capacity (IEC), swelling, water uptake (WU), hydration number (λ), and conductivity (σ). IEC is defined as the moles of mobile charge carriers that can be displaced or exchanged by equivalent charge carriers, divided by the mass of the material with fixed charge groups. Water uptake describes the mass of water that a membrane can absorb, compared to the membrane's mass. From the water uptake, the hydration number can be calculated. This is the number of water molecules per counterion. When

referring to membranes, conductivity measures the electrical conductance of the material. This can vary depending on factors like relative humidity and the counterion bound to the membrane. For most applications, IEC and conductivity should be at a maximum to decrease the internal resistance of a cell, and effectively conduct ions as quickly and efficiently as possible. The desired values for WU and hydration number are highly dependent on the application, and are not necessarily required to be at a minimum.

The AEM used in this thesis is based on methylated poly[2,2'-(2,2",4,4",6,6"-hexamethyl-p-terphenyl-3,3"-diyl)-5,5'-bibenzimidazole], or HMT-PMBI. This membrane exhibits low WU and is highly conductive for various anions, and possesses moderate swelling.[37] The evolution of HMT-PMBI is shown in **Figure 6**, has origins with the use of blends of sulfonated poly(ether ether ketone) (SPEEK) or sulfonated poly(aryl ether sulfone) (SPAES) with commercially available polybenzimidazole (PBI) in order to decrease swelling and increase structural stability of high IEC, crosslinked membranes. These blends were designed to allow for ionic crosslinking. Sulfonated PBI contains a basic and acidic site, which leads to self-neutralization. This leads to near-zero experimental IEC, due to the removal of key hydrogen-conducting acidic sites. Despite this, low-swelling and highly stable sulfonated crosslinked polymers were successfully created.[38]

Modification of PBI via deprotonation and methylation yielded an excellent anion exchange material, specifically poly(dimethyl benzimidazolium) salts $[PDMBI^{2+}]_2[X^-]$. Key membrane parameters, including conductivity and hydration number, were measured for $[PDMBI^{2+}]_2[X^-]$, where X is the counterion (I^-, Br^-, Cl^-, NO_3^-, and HCO_3^-). In the form of $[PDMBI^{2+}]_2[HCO_3^-]$, the material exhibits high IEC and anionic conductivity, while having a relatively low λ. It was also reported that a hydroxide form of PDMBI could not be synthesized as hydroxide begins a ring-opening reaction, decomposing PDMBI.[39]

To afford an AEM that can withstand highly alkaline conditions and hydroxide counterions, the instability of the polymer towards hydroxide had to be solved. A similar, novel polymer was made, with a mesitylene group in place of the previous phenylene group, creating mes-PBI. Again, this polymer was deprotonated and methylated to yield poly[2,2'-(m-mesitylene)-5,5'-bis(N,N'-dimethylbenzimidazolium)], or $[mes\text{-}PDMBI^{2+}]_2[X^-]$. The motivation behind this synthesis was to sterically hinder nucleophilic attack of hydroxide at the C2-position, this was first proven to work on model compounds. A prime limitation of mes-PDMBI is its high water solubility, meaning it cannot be used in aqueous electrolysers. To remedy this a blend of

mes-PBI and mes-PDMBI was prepared. Upon exposure to KOH, the N-H proton is deprotonated by hydroxide, leaving a negative charge to be stabilized by a potassium cation. At the same time, the iodide counter-ion in mes-PDMBI is exchanged for hydroxide. The potassium and hydroxide counter-ions are washed off, allowing for a strong ionic interaction between the positive charge of mes-PDMBI and the negative charge of mes-PBI. The resulting polymer is insoluble in water, has good mechanical strength, and is stable in 2 M KOH at 60 °C for at least 13 days.[40]

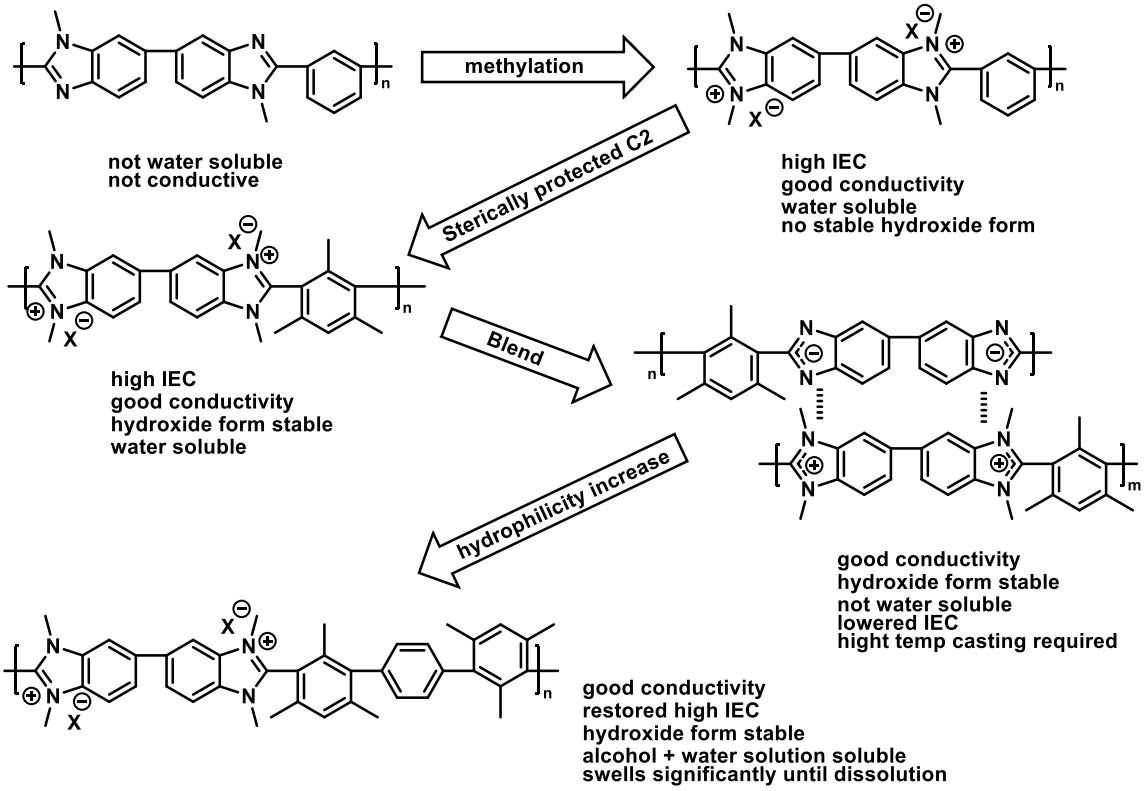

Figure 6. The evolution of poly[2,2'-(2,2",4,4",6,6"-hexamethyl-p-terphenyl-3,3"-diyl)-5,5'-bibenzimidazole], known as HMT-PMBI, and the relevant design choices between generations.

While the introduction of the mes-PBI and mes-PDMBI polymer blend solved the impracticality of mes-PDMBI, it also decreased the IEC from 4.5 mequiv·g^{-1} to 1-2 mequiv·g^{-1}. The blend requires DMSO for casting, meaning evaporation requires higher temperature. The next goal in advancing mes-PDMBI required retaining the protection of the C2 position and increasing polymer hydrophobicity without decreasing IEC. To do this, 2,2", 4,4",6,6"-hexamethyl-p-terphenylene (HMT) was used in place of mesitylene. HMT provides the steric protection of the previous mesitylene, while also increasing the hydrophilicity of the repeating

unit to an extent that it is not soluble in water, thus creating the polymer poly[2,2'-(2,2",4,4",6,6"-hexamethyl-p-terphenyl-3,3"-diyl)-5,5'-bibenzimidazole] (HMT-PBI). Methylation yields the AEM, HMT-PMBI. Unfortunately, fully methylated HMT-PMBI in its hydroxide form is slightly soluble in water, and swells over time before dissolving.[41] Reducing the degree of methylation was shown to alleviate this problem,[42] so a synthesis scheme was designed to achieve varying degrees of methylation. These modified membranes showed decreased water uptake at lower degrees of methylation, and lower λ. This benefit is not without cost, as decreasing the degree of methylation decreases IEC and σ. An optimal degree of methylation of 89% was determined.[41] Water uptake (WU), dimensional swelling, ionic conductivity, anion concentration, mechanical strength, and chemical stability were all assessed in addition to testing of the membrane for AEM fuel cell and water electrolyser operation.[37]

The IEC of HMT-PMBI 75% dm and HMT-PMBI 89% dm are reported in literature as 1.49 and 2.3 mmol•g^{-1}, respectively. For comparison, a commercially available membrane, Selemion AMV, has been found to have an experiment IEC of 1.85 mmol•g^{-1}.[43] The IEC directly effects parameters such as swelling, σ, morphology, λ, and WU. While there are no definitive equations or laws that explain the relationship between these parameters, they are interlinked and generally increase together. However, it has been shown that similar membranes with equivalent IECs can have varying WU and λ.[44,45] One of the strengths of HMT-PMBI is the ease of controlling its IEC. The methylation of the nitrogen atoms is stoichiometrically controlled, allowing for a membrane to have an average degree of methylation (% dm). This membrane is made of a distribution of the three repeat units shown in **Figure 7**. This characteristic provides a method for optimizing the membrane chemistry for the device, and conditions it will be used in.

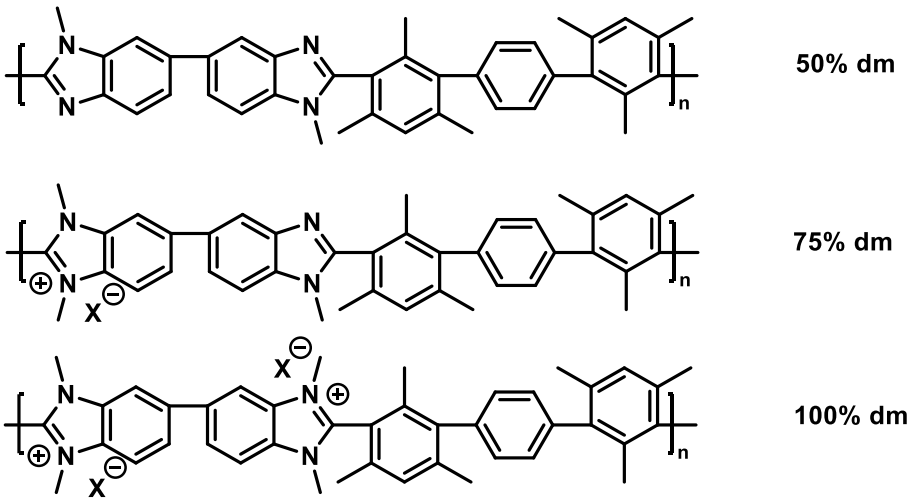

Figure 7. **HMT-PMBI has three possible structures for repeat units in a given polymer. The degree of methylation (% dm) is a measure of how many of the four nitrogen atoms are methylated. At 50% dm, the polymer is ideally neutral, however, the dm is a statistical distribution of all three units above.**

Dimensional swelling and WU measurements are used to understand how different membranes expand or contract when exposed to pure water, electrolyte solutions, or in the context of CO_2E, possible membrane solvents. The expansion of membranes indicates that the free volume of the polymer is increasing due to solvent-polymer interactions overpowering polymer-polymer interactions. This expansion can have devastating effects on the performance of a membrane, as many characteristics that make membranes so invaluable in electrochemical devices are inherently dependent on the narrow ion channels that they form. The dimensional swelling and WU and swelling of HMT-PMBI increases dramatically as IEC increases.[37]

The choice of membrane based on swelling, σ, λ, and WU, is highly dependent on its use. Characterising membranes using these parameters are necessary to understanding the interactions between the polymer and the environment it is used in.

The Assembled electrolyser

The electrolyser itself is the fully assembled device including the aforementioned components, and additional structural components to deliver power and reactants to the cell. The choice of components is more than just using the most efficient and longest lasting materials. Components are chosen based on the type of electrolyser being built. Several device layouts exist, each with benefits and drawbacks.

The MEA-based alkaline electrolyser is the current state-of-the-art for electrolysers that utilize AEMs. The thin form-factor achieves lower internal resistances and favourable kinetics compared to other electrolysers. Many electrolyser designs achieve higher efficiencies by decreasing the energy needed for reactants, products, water, and ions to travel within the cell. There are several publications[22,46–55] that quantify the movement of these species through the cell. Designing electrolysers that carefully control the transport of mass is a persistent challenge. While the membrane is not the only way to control mass transport in an electrolyser, it is one of the most integral. The selectivity of a membrane to conduct reactants, water and ions, and exclude everything else is the main determining factor regulating mass transport.

1.4. Product Crossover

The transport of molecules produced via CO_2E across the IEM is an inefficiency of CO_2E that has been studied as early as 2017.[55] The process of "product cross-over" is described as the process of organic molecules diffusing or being transported across a membrane in an electrochemical conversion or storage device. This phenomenon is primarily a result of concentration gradient across an IEM. In electrochemical devices, the application of a voltage creates an electric field that initiates the flow of ions and water, which can drag across neutral molecules via intermolecular interactions. Charged molecules, such as formate and acetate, that are produced by CO_2E, are drawn to the anode due to the electric field established across the device. The cross-over of neutral and charged products within a CO_2E cell splits the stream of products, increases separation costs in addition to potentially detrimental interactions between products and the IEM. There has been a rapid increase in publications studying product cross-over within CO_2E cells.[52,56–58] These articles prioritize the study of mass transport to explain what factors influence the rate of product cross-over. One study has correlated physical parameters such as applied potential, CO_2 pressure, membrane thickness, membrane porosity, and membrane charge, to decreased carbonate and product cross-over.[58] The most common strategy for decreasing product cross-over in literature is the use of Bipolar membranes[53–55,59] There are very few studies regarding product cross-over through AEMs, the modification of these AEMs to determine chemical structure dependence of product cross-over, and simultaneous membrane characterisation of membranes exposed to CO_2E products. This presents a void in literature that must be explored to evaluate potential solutions to abate product crossover.

Whether driven by a concentration gradient or by an electric field, the movement of molecules and ions within an electrochemical device are not always in the designer's control.

This transport increases the operating costs and decreases the efficiency and/or lifetime of a device; chemical modification of the membrane could be the key to mitigating unfavourable product cross-over in CO_2E cells.

The modification and directed evolution of successful existing membrane structures, such as HMT-PMBI, allow researchers to elucidate connections between polymer chemistry and *in situ* performance. Building on an already proven foundation, Weissbach *et al*[60], and Cassegrain *et al*[61], performed a crosslinking and zwitterionification of HMT-PMBI, respectively. These modifications were both motivated by observations in literature showing that traditional crosslinking[62–65] and zwitterionic crosslinking[66–72] could decrease swelling and WU, and increase the selectivity of the membrane. These modified membranes have been chosen for a comparative study, with the objective of evaluating their efficacy on abating product crossover. The crosslinking performed by Weissbach *et al*[60] is shown below in **Figure 8**. Massive decreases in WU and swelling were observed in crosslinked samples, compared to pristine HMT-PMBI. This crosslinking was achieved using α,α'-dichloro-*p*-xylene in a single step reaction. The membrane shown below represents a repeat unit with nitrogen atoms that are fully functionalized and has a degree of crosslinking (dx) of 25%. Polymers were prepared with a degree of functionalization (df) lower than 100%, where df = dm + dx.

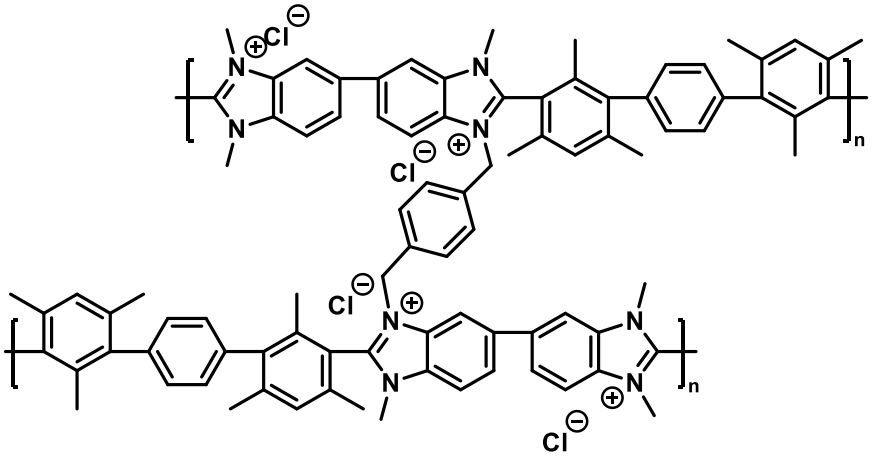

Figure 8. Crosslinked HMT-PMBI, using α,α'-dichloro-*p*-xylene as the crosslinking agent.

Figure 9 shows the zwitterion-functionalized HMT-PMBI synthesized by Cassegrain *et al*.[61] This polymer is synthesized using a single step reaction with 1,3-propane sultone. This leads to a polymer with both positive and negative charges. These zwitterion chains are hypothesized to

crosslink ionically, neutralizing their charge using polymer-polymer interactions, instead of using labile ions.

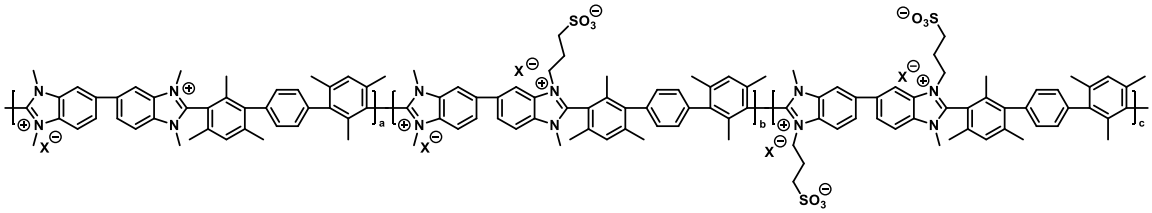

Figure 9. The full structure of zwitterion-functionalized HMT-PMBI. All nitrogens are either methylated or functionalized with the alkyl sulfonate. A statistical distribution of unit a, b, and c exists.

For the zwitterion-functionalized material, HMT-PMBI 75% dm 25% dz, there are two possible theoretical IECs, depending on whether the polymer has ionically crosslinked (1.24 mmol•g^{-1}) or is fully ionized (2.49 mmol•g^{-1}).

Evaluating the changes in product crossover rates in membranes within the same family, but with different functionalities, such as the two polymers above, could elucidate relationships between membrane chemistry, membrane properties, and product crossover.

1.5. Objectives

Current studies aiming to develop AEMs for efficient and durable CO_2 electrolysers often do not investigate the negative effects of product crossover on the integrity and efficiency of the cell. This area of research is critical for understanding how membranes fail in devices with a high production rate of CO_2E products. It is important to determine which membrane properties relate to lower product cross-over, to guide new researchers to make membranes that are designed to decrease product cross-over and improve the durability of the membrane. To achieve this, a robust and comprehensive testing strategy must be created and evaluated with membranes that provide a good foundation to build on. Upon this foundation, tuning of IEC, functionalization and crosslinking can be investigated as potential solutions to abate product crossover.

Target CO_2E products such as ethanol pose a complicated relationship with the membranes that are required to operate CO_2Es efficiently. Ethanol is a relatively good solvent of hydrocarbon membranes, such as HMT-PMBI 89% dm, which dissolves at a concentration of 2.5

M. This poses a significant threat to the longevity, permeability, and performance of CO_2Es which operate with hydrocarbon membranes.

Literature concerning the transport of ions and molecules in CO_2 electrolysers has just recently been published in the last 5 years, with rapidly increasing interest. This highlights the relevance of exploring techniques for evaluating novel membranes' ability to conduct and reject the preferred ions and molecules. Several articles have shown that membrane design can have a significant effect on the extent of product crossover, but more detail is required to evaluate *why* different membrane chemistries are effective at abating product crossover. These studies prove that intentional modification of membrane chemistry is an effective tool for combatting product crossover.

At the time of writing, only a handful of studies attempt to relate the rate of crossover with measurable membrane characteristics. Finding a correlation between product crossover and membrane characteristics such as IEC, swelling, SU, and chemical structure, are critical in explaining why certain membranes perform significantly better than others. The goal of this work is to assess the diffusion of ethanol in an established membrane chemistry, HMT-PMBI, with and without chemical and electric potential gradients, and compare these findings to commonly measured membrane characteristics.

Chapter 2. Methods and Theory

2.1. Mass Transport and Diffusion

Fick's first law of diffusion is the simplest description of transport driven by a concentration gradient, described by **Equation 2**. It is intrinsic to CO_2E that a high concentration gradient will be established, especially in a high current density/efficiency cell. Due to the current trend towards thinner "zero-gap" membranes such as in an MEA-type cell, the gradient is increased further as *dx* decreases. Fick's first law is expanded, as electrolysers will also have an electric potential gradient established when current is applied. To account for this, the Nernst-Planck flux equation must be used. In its simplest form, **Equation 3**, adds a term to Fick's law to account for the transport of charged molecules due to an electric potential gradient.

$$J_i = -D_i \frac{dC_i}{dx}$$

Equation 2. **Fick's first law describes the flux of a species (J_i) as a function of the diffusion coefficient of the species (D_i) and the concentration gradient (dC_i) of the species across a membrane of a defined thickness (dx).**

One additional modification to **Equation 2** adds a term for the chemical activity of the molecule, shown in **Equation 3**. In this work, the activity of the species/molecule being described is assumed to be constant across the membrane, meaning this term reduces to zero. This yields **Equation 4**, shown below.

$$J_i = -D_i \left[\frac{dC_i}{dx} + z_i C_i \frac{F}{RT}\frac{d\psi}{dx} + C_i \frac{d \ln \gamma_i}{dx}\right]$$

Equation 3. **The Nernst-Planck flux equation defines the flux (J_i) of a species (i) through a membrane driven by a concentration gradient ($\frac{dC_i}{dx}$), and elecritc field gradient ($\frac{d\psi}{dx}$), with a correction for chemical activity ($C_i \frac{d \ln \gamma_i}{dx}$). The Faraday constant (F), temperature in Kelvin (T), molar gas constant (R), and the charge of the species (z_i) are required values to satisfy the equation.**

$$J_i = -D_i \left[\frac{dC_i}{dx} + z_i C_i \frac{F}{RT}\frac{d\psi}{dx}\right]$$

Equation 4. **The Nernst Planck flux equation which has been simplified by removing the chemical activity correction.**

At this point it is possible to describe the transport of charged molecules caused by a concentration gradient and an electric potential gradient. This form of the Nernst-Planck flux equation cannot account for the transport of uncharged molecules caused by an electric potential gradient. A final term must be added which describes the motion of uncharged molecules (often acting as solvent) due to the motion of charged molecules across an IEM. This is known as the convection of pore liquid.[73] The Nernst-Planck flux equation takes the final form in **Equation 5**. The term $\bar{C}_i V^*$ is further described in **Equation 6**. This term relies on measuring physical properties of the membrane that are difficult to measure and beyond the scope of this project. All versions of the Nernst-Planck flux equation used in this work are based on the review by N. Lakshminarayanaiah.[74]

$$J_i = -D_i \left[\frac{dC_i}{dx} + z_i C_i \frac{F}{RT} \frac{d\psi}{dx} \right] + \bar{C}_i V^*$$

Equation 5. The Nernst-planck equation with a term that describes convection, a driving force which depends on the concentration of a species inside the membrane ($\bar{C}_i$) and the velocity of movement of the center of gravity of the pore liquid (V^*).

$$\bar{C}_i V^* = \bar{C}_i * \frac{\omega X F}{\rho_0 \upsilon_0} \frac{d\psi}{dx}$$

Equation 6 Advection term is dependent on the velocity of movement of the center of gravity of the pore liquid (V^*). This is dependent on the electric field gradient across the membrane ($\frac{d\psi}{dx}$), the Faraday constant (F), the sign (+ or -, ω) and concentration (X) of fixed charges within the membrane, the specific flow resistance of the membrane (ρ_0), and the fractional pore volume (υ_0).

The Nernst-Planck flux equation, as shown above in **Equation 5**, can be broken down for use on charged and uncharged molecules. For charged molecules, the third term is not needed as it deals solely with motion imparted by charged molecules on uncharged molecules, yielding **Equation 7**. For uncharged molecules, the variable describing the valence of the molecule, "z", is zero. This reduces the whole term to zero, yielding **Equation 8**.

$$J_i = -D_i \left[\frac{dC_i}{dx} + z_i C_i \frac{F}{RT}\frac{d\psi}{dx}\right]$$

Equation 7 **The form of the Nernst-Planck flux equation which describes the flux of charged species through a membrane, driven by a concentration and electric field gradient.**

$$J_i = -D_i \left[\frac{dC_i}{dx}\right] + \bar{C}_i V^*$$

Equation 8 **The form of the Nernst-Planck flux equation which describes the flux of neutral species through a membrane, driven by a concentration and convection dependent on the an electric field gradient across the membrane.**

The Nernst-Planck flux equation uses the diffusion coefficient to account for interactions between the membrane and the transported molecules. If a membrane is non-ideal, using this form of the Nernst-Planck flux equation to calculate a diffusion coefficient causes it to change over time. This ideal membrane assumption also neglects interactions of uncharged molecules which could have strong interactions with the polymer membrane or charged species fixed or bound to the membrane. This is counterintuitive to the intentional design of IEMs, which are made to specifically reject ions whose charge is the same sign as the fixed charge.

Another assumption is that the diffusion coefficient does not change as a function of the concentration gradient, also known as a steady-state assumption. After a concentration gradient is established in a CO_2 electrolyser, the gradient should remain constant as long as the catalyst is not poisoned, the membrane is not fouled, degraded, or changed in any way, and the applied current density, and therefore electric field across the cell, does not change. While these are processes that are present in current CO_2E devices, this work hopes to contribute to the understanding of how the membrane changes due to diffusion of ethanol though the membrane.

Non-steady state diffusion cannot be described by the forms of the Nernst-Planck flux equations shown above. This type of diffusion requires flux equations in the form of Fick's second law, as shown in **Equation 9**.

$$\frac{\partial C_i}{\partial t} = D\frac{\partial^2 C_i}{\partial x^2}$$

Equation 9. **Fick's second law describes the change in concentration over time as function of the diffusion coefficient (*D*) and the second-order partial differential equation of the concentration gradient across the membrane.**

There are several solutions to the partial differential equation of Fick's second law, however, the boundary conditions used assume characteristics about the concentration, volume and/or membrane thickness, to be infinite. There are few studies[75] which compare a second-order Nernst-Planck flux equation applied for non-steady state conditions to experimental data. These have been found to accurately model simple diffusion processes like Donnan dialysis. The caveat to using such equations is the necessity of measuring all terms present in the Nernst-Planck flux equation throughout the experiment. Attempts to do this are not made in this project. The knowledge of these equations that describe observed diffusion processes in and across membranes gives the background necessary to infer what processes are responsible for observations in this work.

2.2. Materials and Chemicals

The H-cell used in this project was made by Lucas Clarke at the Simon Fraser University glass shop using borosilicate glass. Reference electrodes were sourced from Pine Analytical, both used were Ag/AgCl double junction electrodes with 10 wt% KNO_3 filling solution. All 18 MΩ water used was made with a Synergy UV ultrapure (type 1) water maker. Ethanol used in this study was 95% and sourced from Commercial Alcohols by Greenfield Global. $KHCO_3$ (99.7% pure ACS reagent) was sourced from Sigma Millipore and was dried for 2 days at 80 °C before use. KOH and NaCl used was sourced from Fischer Scientific (both ACS certified reagents). The DC power source used was an Agilent E3631A. The tensile testing device used was an Instrom Standard Height Standard Width 1 Test Space. Any other instruments used are described as they are discussed. Platinum wires (0.25 mm diameter) were sourced from Sigma-Aldrich (purity 99.99% trace metals basis).

CO_2 used was sourced from Praxair Canada and had a purity of 99.998%. HMT-PMBI 75% dm and 89% dm were synthesized by Dr. Andrew Wright and used as received. HMT-PMBI 75% dm 25% dz was synthesized by Dr. Simon Cassegrain and additional polymer was synthesized using his synthesis scheme, as needed. HMT-PMBI 75% dm 5% dx was synthesized using HMT-PMBI 75% and α,α'-dichloro-*p*-xylene (Sigma Millipore 99.9% pure), with DMSO as solvent sourced from Fischer Bioreagent with an assay purity of 99.7%. D_2O used was sourced from Sigma Aldrich with 99.9% deuterium atom. 1,3-propane sultone was sourced from Combi-blocks at 98% purity and was dried at 60 °C before use.

2.3. Synthesis

2.3.1. Synthesis of Zwitterion-functionalized HMT-PMBI 75% dm 25% dz

The synthesis of HMT-PMBI 75% dm 25% dz was carried out using HMT-PMBI 75% dm. HMT-PMBI membrane previously synthesized by Wright[37] was dissolved (10 wt%) in dimethyl sulfoxide (DMSO, 99.9%, FischerBioreagent) in a closed pressure vessel and constantly stirred at 80 °C overnight. Once the polymer was fully dissolved, a molar excess of 1,3-propane sultone (98%, combi-blocks) was added to the pressure vessel. The vessel was resealed, and the reaction mixture was stirred at 80 °C overnight to allow complete functionalization of the nitrogen highlighted in red in **Figure 10**. These steps adhere to previously published methods that have led to the reproducible synthesis of the polymer shown in **Figure 9**.[61]

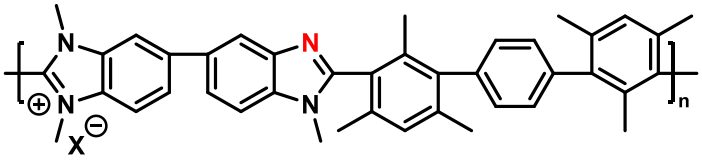

Figure 10. A single repeat unit of HMT-PMBI 75% dm, with one nitrogen (in red) available for electrophilic attack by 1,3-propane sultone.

The obtained polymer solution was then cast onto a clean glass plate using an automatic doctor blade set to 370 microns to achieve a membrane with a nominal thickness of ~33 μm.

2.3.2. Synthesis of Crosslinked HMT-PMBI 75% dm 5% dx

The synthesis of HMT-PMBI 75% dm 5% dx was carried out using previously synthesized stock of HMT-PMBI 75% dm.[37] As described by Weissbach *et al*[60], **Equation 10** was used to calculate the necessary mass required of α,α'-dichloro-*p*-xylene (DCX, 99%, Sigma Aldrich) needed to complete the crosslinking.

$$m_{DCX} = \frac{2 \cdot Mw_{DCX} \cdot m_{HMT} \cdot dx}{Mw_{HMT} + Mw_{MeCl} \cdot (4 \cdot dm - 2)}$$

Equation 10. The required mass of DCX needed (m_{DCX}) for a degree of crosslinking (dx) can be calculated using the molecular weight of DCX (Mw_{DCX}), one repeating chain of HMT-PMBI 50% dm (Mw_{HMT}), and MeCl (Mw_{MeCl}), and the mass of HMT-PMBI (m_{HMT}).

This equation differs in one way from literature, in that the molecular weight of MeCl is used instead of MeI. This is because the stock HMT-PMBI 75% dm was exchanged to chloride form and dried before crosslinking, exchanging iodide counterions (from MeI) with chloride. The only other modification to the synthesis was the using HMT-PMBI 75% dm as a base to crosslink, rather than the neutral polymer (HMT-PMBI 50% dm). The mass of weighed HMT-PMBI 75% dm was converted to moles, then that value was converted to a mass of neutral HMT-PMBI 50% dm for use in **Equation 10**.

To perform the crosslinking, a known mass of dry HMT-PMBI 75% dm was dissolved in DMSO overnight with gentle heating (<60 °C). DCX was dissolved in a minimal amount of DMSO and then combined with the polymer in a pressure vessel. The reaction mixture was sealed tight and heated to 80 °C for 30 minutes. The reaction mixture was then poured onto a glass plate and cast using an automatic doctor blade set to a height of 450 μm. The film was then placed in an oven set at 85 °C for 12 hours. The obtained membrane was wet to assist with peeling it off the glass, then soaked in 4 L of 18 MΩ water 3 times to remove any excess DMSO or unreacted DCX. The membrane was dried in a vacuum oven at 80 °C for 24 hours. A membrane with a nominal thickness of ~34 μm was obtained.

2.4. Ex-Situ Characterisation of Membranes

2.4.1. Exchanging Counterions in HMT-PMBI

For the following measurements, membranes were all exchanged using the same process. Each membrane was exchanged from chloride counterions to hydroxide counterions by soaking the membrane in 3 M potassium hydroxide at a ratio of at least 10 mL per 100 mg of membrane. The solution was replaced with fresh solution each day for 3 days. This was followed by exchanging the membrane from hydroxide counterions to bicarbonate counterions by soaking the membrane in 1 M potassium bicarbonate at a ratio of at least 10 mL per 100 mg of membrane. A final rinsing step was conducted to remove excess salt by soaking the membranes in pure 18 MΩ water several times until the conductivity of the surrounding solution was undetectable (under 1 μS) using a handheld OMEGA conductivity/TDS/Salt/temp waterproof tester (CDH-7021).

2.4.2. Ion Exchange Capacity

Ion exchange capacity measurements are an important metric when studying and comparing any IEMs. IEC is a measure of the average number (moles) of charged groups per gram of polymer. This metric tends to have a direct impact on water uptake, water transport, hydration number and conductivity, in non-crosslinked membranes. The intent of measuring the IEC of each membrane was to discover any trends in ethanol diffusion that match IEC increases. Theoretical IEC is the maximum capacity of ionically bound charged groups balancing the opposing charge of the membrane. This differs from experimental IEC which is lower due to inaccessibility of all ionically bound charges, whether due to steric bulk preventing ion dissociation and/or regions of poor solubility. Measuring the IEC of the HMT-PMBI type membranes explored in this work is an important first step in characterizing each of the four membranes. This allows trends that are observed later, to be compared to their relative IECs.

Ion exchange capacity was measured via titration of exchanged chloride ions, using a method previously described.[76] Three samples of each membrane were cut using a hammer and rectangular die, measuring just under 20 mm x 50 mm, the area of a punch of paper using the die was 10.057 cm^2. The membranes were exchanged to chloride form over three days, exchanging ~25 mL of 3 M NaCl solution daily. Excess NaCl was rinsed from the membranes over 12 hours with 18 MΩ water several times until the conductivity of the surrounding solution was undetectable (under 1 μS) using a handheld OMEGA conductivity/TDS/Salt/temp waterproof tester (CDH-7021). The membranes were dried under vacuum at 80 °C for 12 hours, and then immediately weighed to obtain a dry mass, using an OHAUS Explorer Pro precision balance. These samples were soaked twice in 20 mL of 2.3 M $NaNO_3$ for 5 hours. This ensured a complete exchange of chloride ions with nitrate ions. Both 20 mL solutions were collected and combined. The solutions were then acidified with 2 mL of 1 M HNO_3 and titrated against a standardized $AgNO_3$ of 0.01 M in 18 MΩ water. The titration was conducted with a Tetrino Plus automatic titrator by Metrohm, using a chloride selective electrode. The IEC was then calculated for each membrane using the measured volume of $AgNO_3$, as described in **Equation 11**.

$$IEC_{Cl^-} = \frac{[AgNO_3] \cdot V_{AgNO_3}}{m_{dry}}$$

Equation 11. The Ion Exchange Capacity (IEC) of a membrane is measured in chloride form to yield IEC_{Cl^-}, using the concentration of the standardized silver nitrate solution ($[AgNO_3]$), volume of silver nitrate solution (V_{AgNO_3}), and the dry mass of the membrane (m_{dry}).

To compare experimental IEC to theoretical IEC, the theoretical IEC for all four membrane types were calculated. For HMT-PMBI 89% dm and 75% dm, **Equation 12** was used. For HMT-PMBI 75% dm 25% dz, two separate equations were used to calculate the case in which it is fully ionized **[Equation 13]**, and the case where it is ionically cross-linked [**Equation 14**]. Lastly, **Equation 15** is used to calculate the theoretical IEC_{Cl^-} of HMT-PMBI 75% dm 5% dx. The calculated values are compared with experimentally obtained IEC in the Results and Discussion chapter.

$$IEC_{Cl^-} = \frac{(1000\ \text{mmol}\cdot\text{mol}^{-1}) \cdot 2 \cdot [2(dm - 0.5)]}{Mw_{100\%\,dm} \cdot 2(dm - 0.5) + Mw_{50\%\,dm}\big(1 - 2(dm - 0.5)\big)}$$

Equation 12. The equation for calculating the theoretical IEC of HMT-PMBI with a value for the degree of methylation (dm): 50 ≤ dm ≤ 100. The molecular masses of an uncharged repeat unit ($Mw_{50\%\,dm}$) and a fully charged repeat unit ($Mw_{100\%\,dm}$) of HMT-PMBI are required to correctly calculate the average molecular weight of the polymer.

$$IEC_{Cl^-} = \frac{(1000\ \text{mmol}\cdot\text{mol}^{-1}) \cdot 2}{Mw_{50\%\,dz} \cdot 2(dz) + Mw_{0\%\,dz}(1 - 2(dz))}$$

Equation 13. The equation for calculating the theoretical IEC of HMT-PMBI with the zwitterion functionalization dicussed in detail in Chapter 1. The equation assumes the polymer is completely ionized, and no ionic crosslinking has occurred.

$$IEC_{Cl^-} = \frac{(1000\ \text{mmol}\cdot\text{mol}^{-1}) \cdot [2 - (4(dz))]}{Mw_{50\%\,dz} \cdot 2(dz) + Mw_{0\%\,dz}(1 - 2(dz))}$$

Equation 14. The equation for calculating the theoretical IEC of HMT-PMBI with zwitterion functionalization discussed in detail in Chapter 1. The equation assumes that all sulfonated alkyl chains in HMT-PMBI 75% dm 25% dz are ionically crosslinked.

$$IEC_{Cl^-} = \frac{(1000\ \text{mmol}\cdot\text{mol}^{-1}) \cdot 4 \cdot (dm + dx - 0.5)}{Mw_{HMT} + 4 \cdot Mw_{MeCl} \cdot (dm - 0.5) + 2 \cdot Mw_{DCX} \cdot dx}$$

Equation 15. The equation for calculating the theoretical IEC of HMT-PMBI crosslinked using DCX as discussed in detail in Chapter 1. The equation uses the molecular weight of a single repeat unit of HMT-PMBI 50% dm (Mw_{HMT}), the molecular weight of the methylating agent used (Mw_{MeCl}) and the molecular mass of the crosslinking agent used (Mw_{DCX}).

2.4.3. Solvent Uptake

Solvent uptake (SU) was measured by converting membranes to their bicarbonate form then rinsing before drying the membranes in a vacuum oven at 75 °C for at least 12 hours under static vacuum. Each membrane was then cut using the previously mentioned rectangular die, ensuring that every membrane was as dry as possible when cut. This was done with the same rectangular die used for the above IEC measurements. The membranes were then dried again under active vacuum in the oven at 75 °C for at least 4 hours. Membranes were weighed immediately on a precision balance to obtain their dry weight (m_{dry}). Three membranes of each type were soaked four different solutions containing 0.5 M $KHCO_3$ and 0 M, 0.5 M, 1.5 M, or 2.5 M ethanol, totalling 12 samples of each membrane type. Each sample was soaked in 20 mL of their solution. The samples were soaked for 24 hours before they were removed from their vial and surface liquid was dried using a Kimwipe. Each membrane was weighed on the same precision balance to obtain a wet mass (m_{wet}). The membranes were then replaced in their solutions to be used for the following dimensional swelling tests. To calculate the solution uptake (SU) of each membrane, **Equation 16** was used.

$$SU = \frac{m_{wet} - m_{dry}}{m_{dry}}$$

Equation 16. The equation for calculating Solution Uptake (SU) uses the change in mass between the membrane's wet mass and dry mass and normalizes it with the membrane's dry mass.

The SU measurements are a contextual version of similar water uptake measurements routinely completed in literature[37,41,60,61] Uptake measurements are *ex situ* tests that give an estimate of the volume of solution that will be absorbed by the membrane *in situ*. WU values correlate with higher hydration numbers, in this project however, SU is more contextual, and useful when examining how ethanol absorbs into the membranes.

2.4.4. Dimensional Swelling

Dimensional swelling measurements were conducted on the same membranes as used for SU. Through-plane swelling (TPS) was measured right after they were weighed to obtain a dry thickness (x_{dry}). After the membranes were soaked and weighed, their wet thickness (x_{wet}) was measured. **Equation 17** was used to calculate TPS as a percentage. The thickness measurements were performed with a Mitutoyo (model #293-676) micrometer accuracy of ±0.0005 mm. In-plane swelling (IPS) was measured by using Inkscape to digitally measure the area of each membrane from an image taken by an Epson Perfection V39 scanner. Membranes were kept wet during the time it took to position and scan them with a couple drops of their respective solutions. This wet surface area (a_{wet}) was compared to the dry surface area (a_{dry}), which is taken to be the dimensions of the rectangular die. **Equation 18** was used to calculate the IPS as a percentage. This method cannot be used to differentiate any differences in swelling along the x- and y-axes, which was assumed to be identical in this study.

$$TPS = \frac{x_{wet} - x_{dry}}{x_{dry}}$$

Equation 17. The equation for through-plane swelling (TPS) normalizes the difference in wet and dry membrane thickness using the dry thickness. This gives an indication into how much the membrane swells upon exposure to a solution, given as a percentage.

$$IPS = \frac{a_{wet} - a_{dry}}{a_{dry}}$$

Equation 18. The equation for in-plane swelling (IPS) normalizes the difference in wet and dry membrane area using the dry area. This gives an indication into how much the membrane swells upon exposure to a solution, given as a percentage.

2.4.5. Tensile Measurements

Tensile measurements were employed to determine the changes in structural integrity upon exposure to ethanol solutions. Twelve standard ISO 527 dog bone shape samples were punched from HMT-PMBI 89% dm, HMT-PMBI 75% dm, HMT-PMBI 75% dm 25% dz, HMT-PMBI 75% dm 5% dx and Selemion AMV, all exchanged to bicarbonate counterions. An Instron tensile measurement instrument was then used to measure the force and elongation of three pristine samples of each membrane as control experiments. The remaining samples were then

soaked in 0.5 M ethanol, 1.5 M ethanol, and 2.5 M ethanol solutions for 24 hours, three samples of each membrane in each solution. The samples were rinsed several times in a large volume of 18 MΩ water to remove any excess ethanol, and dried under ambient conditions for 24 hours, after which their tensile strength was measured.

Tensile measurements are plotted stress versus strain, in MPa and percent elongation, respectively. The stress is calculated by dividing the collected force values by the cross-section of the membrane. To calculate the yield strength, a line was drawn parallel to the slope of a linear section of the linear elastic region and offset to the positive direction of the x-axis by 0.2%. This is widely used as a consistent way to measure the yield strength. The Young's modulus for each sample is calculated from the linear elastic region. The ultimate strength and elongation at break are also reported.

2.5. Pulsed Field Gradient NMR

Diffusion Ordered SpectroscopY (DOSY) or other pulsed field gradient (PFG) NMR spectroscopies to study IEMs are potent techniques for measuring dynamics and morphological phenomena that otherwise cannot be accessed through traditional analytical techniques. Specifically, these measurements are suited for measuring short-range diffusion of NMR-active nuclei in molecules and ions of interest. These experiments are only able to measure the self-diffusion of a molecule or ion. PFG experiments use gradients within or surrounding the probe of a spectrometer to spatially encode nuclei by applying a magnetic field gradient along the z-axis of the sample. This is delivered via a pulse over a short time, δ (s), which leads to precession similar to a normal pulse. Nuclei precess at defined phases dependent on their position along the z-axis of the sample. **Equation 19** defines the total precession frequency (ω_{tot}) as a function of position (z) equal to the negative product of the nuclei's gyromagnetic ratio (γ) and the sum of the external magnetic field (B_0) and the gradient magnitude ($g(z)$).

$$\omega_{tot}(z) = -\gamma\big(B_0 + g(z)\big) = -\omega_0 - \gamma g(z)$$

Equation 19. The equation which describes the total precession frequency, dependent on the gyromagnetic ratio, external magnetic field used, and the magnitude of the gradient used.

After time, Δ(s), another gradient pulse that is equal and opposite to the initial pulse is used to refocus the nuclear spins. If there is no molecular motion along the z-axis, or the diffusion

time Δ is too short, the second gradient will effectively refocus all spins. The usefulness of PFG experiments comes from the diffusion of molecules or ions within the sample along the z-axis during the diffusion time Δ. Any nuclei that have moved during Δ will not be refocused by the second gradient pulse, and the resulting total precession frequency will change from its initial value.

DOSY measurements are a particular type of *pseudo* 2-dimensional PFG NMR that uses a second dimension made up of multiple 1-dimensional spectra with increasing gradient strength until the target nuclei's signal is nearly completely attenuated. This experiment relies on changing the gradient strength (g) in defined steps and observing the change in signal intensity (S) to solve **Equation 20**. The terms for initial signal intensity (S_0), gyromagnetic ratio (γ), gradient strength (g), gradient pulse length/duration (δ), and corrected diffusion time (Δ') are all known or set values, meaning the independent variable is observed signal intensity (S) and the dependent variable is the diffusion coefficient (D).

$$S = S_0 e^{-(\gamma g \delta)^2 \Delta' D}$$

Equation 20. The equation which describes the relationship between the diffusion coefficient of a nuclei corresponding to a signal a defined chemical shift.

Over 16 experiments, the intensity (S) of the signal of interest, is plotted to obtain a curve where the y-axis is the natural log of the ratio of the intensity to the initial intensity, $ln(S/S_0)$. The x-axis is the positive of term in the exponential, $((\gamma g \delta)^2 \Delta')$. The slope of the linear regression of this curve is the diffusion coefficient for the nucleus that corresponds to the signal. The slope of the linear fit of this curve is the diffusion coefficient for the nucleus that corresponds with the signal *S*. diffusion coefficient and/or the concentration of ethanol in the membrane decreases. The NMR analysis program MestrReNova has a built-in DOSY algorithm which converts the data such that the diffusion coefficient is on the y-axis and the chemical shift is on the x-axis.

It is important to note that a dedicated diffusion probe was unavailable for these tests, so the internal gradients (with a maximum strength of 50 G/cm) were used. Dedicated diffusion probes exist and are highly specialized instruments for use in PFG experiments with slowly diffusing samples. For comparison, the "Diff50" probe from Bruker has a gradient strength of up to 30 T/m.[77] For slow-diffusing molecules, higher strength gradients are needed for the most accurate results.

2.6. Permeability Measurements

According to the Nernst-Planck flux equations, the diffusion coefficient of a species through a membrane should be independent of the concentration gradient across the membrane. The figures in **3.3** are constructed from permeability tests used to compare the diffusion rate of ethanol across a membrane as a function of three chosen ethanol concentrations, 0.5 M, 1.5 M, and 2.5 M.

To evaluate the diffusion coefficients of CO_2E product transport through hydrocarbon-based membranes, this work employed permeability tests using an H-cell **[Figure 11]**. The H-cell consisted of two glass vessels that mate to one another in such a way that a membrane can separate each container's contents. The H-cell used in this work has special fittings to allow reference electrodes to be placed up against each side of the membrane to measure the voltage across the membrane. Three other ports on each vessel allowed for bubbling of CO_2 in the catholyte to saturate the solution with dissolved gaseous CO_2 and allow for platinum electrodes to be introduced to apply current to the cell.

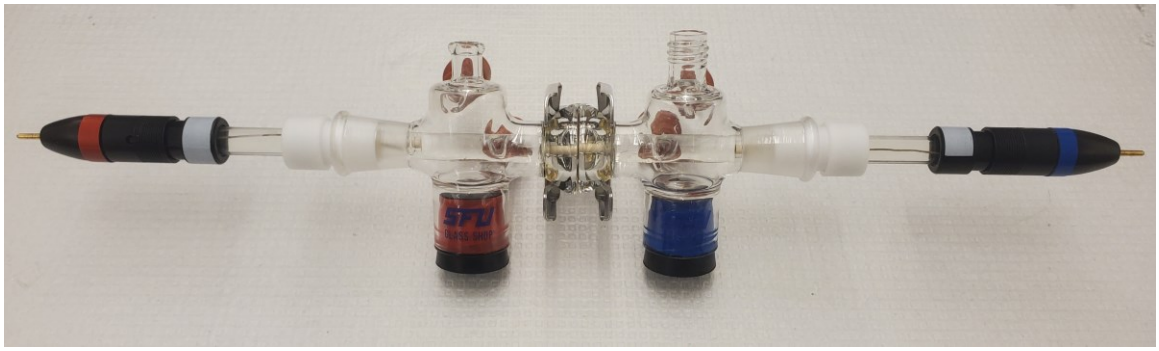

Figure 11. The H-cell used in this work was made by the Simon Fraser University glass blowing shop. A metal clamp and O-ring seal a membrane inbetween the two compartments. Openings in the top allow for CO_2 to be bubbled in. Ag/AgCl reference electrodes are shown, as sourced from Pine Analytical.

The H-cell was an excellent device for isolating the membrane and its interactions with catholyte and anolyte solutions. It facilitates introducing concentration gradients and electric potential gradients similar to those that are present in CO_2 electrolysers. The area of the exposed membrane was determined to be 2.37 cm^2 by fastening the membrane using an O-ring and metal ball and socket clamp, then subjecting the membrane to water with green food coloring. This

yielded the membrane shown in **Figure 12**. The area was then measured digitally using Inkscape's measuring tool.

Figure 12. **Using green food coloring, the cross-section of the membrane that is exposed to catholyte and anolyte in the H-cell was measured. The dyed section shows the region that was exposed to solution. The membrane was scanned and the area was measured using Inkscape.**

For all permeability experiments in this work, the reference electrodes were connected to a Rigol 3058 digital multimeter in DC voltage mode. The reference electrodes are Pine Analytical double-junction Ag/AgCl electrodes with a filling solution of 10% KNO_3 (aq.). Before and after each experiment both electrodes were connected to the digital multimeter and their tips were submerged in filling solution to determine the average voltage difference. This acted as a baseline for any voltage drift that occurred during the experiment due to the catholyte and anolyte solutions permeating the interior of the reference electrodes.

Once the reference electrodes were attached and aligned with the membrane the H-cell was assembled and catholyte and anolyte was added. The catholyte contained 0.5 M $KHCO_3$ and either 0.5, 1.5, or 2.5 M ethanol. The anolyte only contained 0.5 M $KHCO_3$. Using a needle and flow control device, CO_2 (99.995% purity) was bubbled at a rate of 20 cm^3 per minute for 30 minutes. At the end of this 30-minute period, a sample of 250 μL was taken from each side of the cell and combined with 250 μL of an internal standard of acetonitrile in deuterium oxide. The internal standard added to catholyte samples had a concentration of 1.5 M acetonitrile, while a concentration of 0.1 M acetonitrile was used for the anolyte samples. A sample was taken every

hour, for four hours. This experiment monitored the flux through the membrane for a given starting concentration gradient.

Acetonitrile was chosen as an internal standard as it is inert in this system, produces a sharp singlet signal in ^{1}H NMR that is far from water's proton signal. All volumes were measured using a Finnpipette 100 to 1000 μL micropipette.

The use of 0.5 M $KHCO_3$ was chosen because it is one of the most common and best performing supporting electrolytes in literature, other than hydroxide. As discussed in **1.3.2**, membranes currently are plagued by carbonation, which would add another independent variable to this study of hydroxide was used. Starting the entire system in bicarbonate form minimizes effects from this phenomenon.

2.6.1. Quantification of CO_2E Products in Permeability Measurements

The concentration of ethanol in catholyte and anolyte samples were determined using quantitative ^{1}H NMR, using a Bruker 600 MHz Avance II with a 5 mm QNP cryo-probe. Samples from the H-cell were aqueous and thus had a significant and overwhelming water ^{1}H signal when a simple π/2 pulse was used. This necessitated the use of a pulse sequence that sufficiently suppressed water's proton signal while retaining quantification of analyte signals. The prime candidate for such a pulse sequence was the WATER suppression by GrAdient Tailored Excitation (WATERGATE) experiment[78], specifically the enhanced W5 version.[79] This experiment selectively suppresses the water proton while maintaining the intensity and integration of all other signals. The D1 delay for this experiment must be at least five times the slowest T_1 of the system. Spectra were acquired using increasing D1 delays until no further change in integration was observed. A delay of 10 seconds was found to be sufficient. Other acquisition and processing parameters were optimized according to literature to prioritize quantification of the ethanol and acetonitrile (internal standard) signals.[80] One of the keys to proper quantification was consistent integration. It has been calculated that 99% of the integral of a signal will be within ±25 times the linewidth of a signal. The linewidth of a signal is the width at half of the maximum intensity. Accepting a 1% error, TopSpin's *peakw* command was used to calculate the linewidth, which was used to find the optimal integration regions.

2.6.2. Extracting Diffusion Coefficients from Permeability Experiments

The diffusion coefficients from the permeability experiments are calculated using the following procedure. The integral of the CH_3 proton signal from ethanol are normalized to the CH_3 proton signal from the internal standard, acetonitrile. The integral value is converted to the measured concentration of ethanol in the sample. With accurate timings of when each sample was taken and ethanol concentration values, a graph of concentration versus time can be constructed. To calculate the flux of ethanol over the experiment, the slope of the change in ethanol concentration for either the catholyte or anolyte is found using linear regression. The slope represents the change in concentration over time. To convert this to flux, the slope must be multiplied by the volume of the catholyte or anolyte (both being 20 mL), and divided by the cross-section of the membrane, as calculated in **Figure 12**. To calculate the concentration gradient, the difference between the ethanol concentration measured in the catholyte and corresponding ethanol concentration in the anolyte is used. This is divided by the thickness of the membrane, as measured at the end of each experiment. This gives a unique diffusion coefficient for each moment a sample was taken.

Chapter 3. Results and Discussion

3.1. Ex-Situ Measurements

Membrane chemistries are unique and effect important characteristics such as the IEC, solution uptake, dimensional swelling, and tensile strength. Ethanol diffusion though a membrane is directly related to the membrane chemistry. Investigating the nature of this relationship is critical to understanding what chemical modifications can decrease ethanol cross-over in CO_2 electrolysers. Measuring the diffusion of ethanol through different HMT-PMBI-type membranes and comparing these diffusion coefficients with characteristic measurements can elucidate connections between the two.

3.1.1. Ion Exchange Capacity Measurements

The theoretical IEC_{Cl^-} of each membrane was calculated and compared to the experimentally measured IEC. Using **Equation 12**, **Equation 13, Equation 14**, and **Equation 15**, the theoretical IEC_{Cl^-} of each membrane type was calculated and shown below in **Table 2**. The IEC_{Cl^-} for all four HMT-PMBI-type membranes were measured experimentally as outlined in **2.4.2**. The results are shown below in **Figure 13**.

Table 2. The calculated theoretical IEC_{Cl^-} are compared to the experimentally measured IEC_{Cl^-}. The IEC_{Cl^-} of HMT-PMBI 75% dm 25% dz can vary depending on the extent of ionic crosslinking. Ionic crosslinking leads to neutralization of charge, thereby decreasing the IEC_{Cl^-}. The theoretical IEC_{Cl^-} for HMT-PMBI 75% dm 25% dz is shown for the fully ionized form* and for the fully ionically crosslinked form. † Standard deviation from these experiments are calculated from triplicate measurements.

Membrane Type	Theoretical IEC_{Cl^-} ($mmol \cdot g^{-1}$)	Experimental IEC_{Cl^-} ($mmol \cdot g^{-1}$)	SD
HMT-PMBI 89% dm	2.39	1.97	0.07
HMT-PMBI 75% dm	1.60	1.51	0.06
HMT-PMBI 75% dm 25% dz	2.49*	1.19	0.02
HMT-PMBI 75% dm 25% dz	1.24†		
HMT-PMBI 75% dm 5% dx	1.87	1.43	0.02

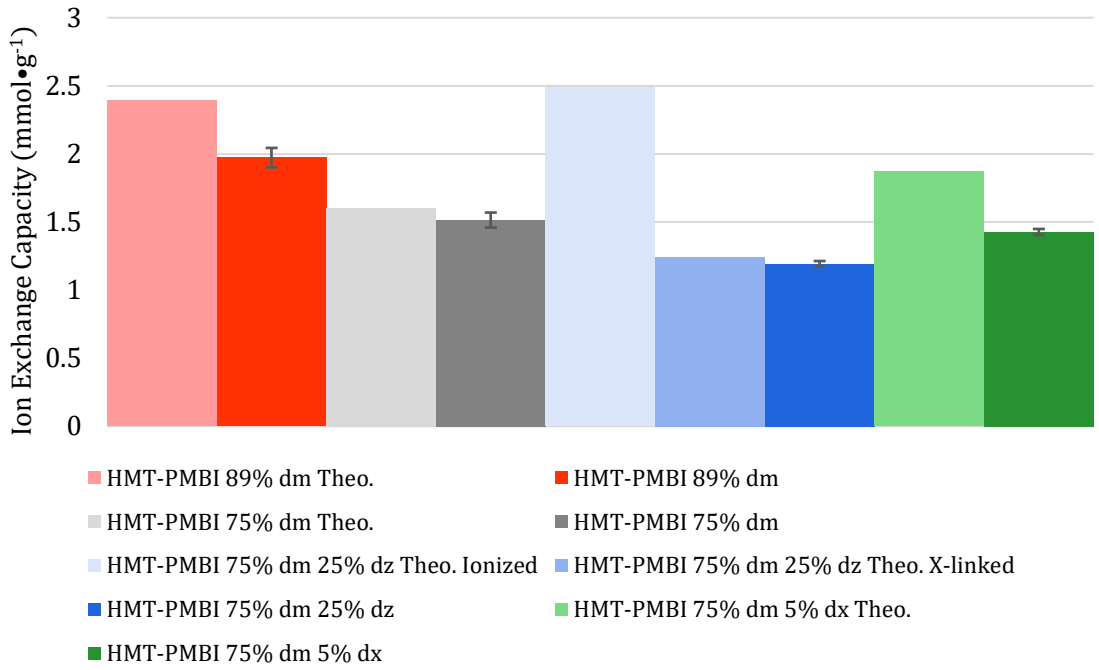

Figure 13. **Ion Exchange Capacity (IEC) values for four variations of HMT-PMBI. HMT-PMBI 89% dm has the highest IEC, at 1.97 mmol•g^{-1}. Functionalization of HMT-PMBI 75% dm (1.51 mmol•g^{-1}) with zwitterionic functional groups decreased the IEC to 1.19 mmol•g^{-1}. Cross-linking of HMT-PMBI with α,α'-dichloro-p-xylene to achieve 5% crosslinking decreased the IEC to 1.43 mmol•g^{-1}. The theoretical IECs are shown in lighter colors, grouped by their membrane type.**

The measurements showed a significant decrease in experimental IEC_{Cl^-} upon the modification of HMT-PMBI 75% dm to HMT-PMBI 75% dm 25% dz and HMT-PMBI 75% dm 5% dx. It was expected that the IEC would increase as more nitrogen groups were increased from two carbon bonds to three carbon bonds, elevating the nitrogen from neutral to a +1 charge. This would require an additional counterion, thereby increasing the IEC_{Cl^-}. However, this was not observed during these IEC_{Cl^-} measurements. This could have been due to inaccessible sites within the polymer network that are too sterically constrained, due to crosslinking. The measured IEC_{Cl^-} of HMT-PMBI 75% dm 25% dz may be lower than the actual IEC, as the experimental method only measures anionic exchange capacity, specifically accessible chloride. As shown in **Table 2**, HMT-PMBI 75% dm 25% dz can theoretically have an IEC_{Cl^-} anywhere from 1.24 to 2.49 mmol•g^{-1}, which is hypothesized in literature to depend on the degree of ionic cross-linking.[61] Due to measured IEC_{Cl^-} of 1.19 mmol•g^{-1}, it is assumed that the degree of ionic crosslinking is significant.

If ethanol uptake and thereby diffusion are directly related to IEC_{Cl^-}, a minimum D_{EtOH} may be found for the membrane with the lowest IEC_{Cl^-}. While the experimental IEC_{Cl^-} measurements indicated HMT-PMBI 75% dm 25% dz to have the lowest IEC_{Cl^-}, the test did not account for sodium ions bound to the sulfonate groups. The next lowest measured IEC_{Cl^-} was that of HMT-PMBI 75% dm 5% dx. However, as discussed, the experimental data does not match the IEC_{Cl^-} expected for HMT-PMBI 75% dm 5% dx. The next lowest experimental IEC_{Cl^-} is that of HMT-PMBI 75% dm. Using experimental IEC_{Cl^-} as a guide, HMT-PMBI 75% dm 25% dz is hypothesized to possess the smallest ethanol diffusion coefficient. Conversely, based on theoretical IEC_{Cl^-}, HMT-PMBI 75% dm is hypothesized to possess the smallest ethanol diffusion coefficient.

3.1.2. Solution Uptake and Swelling Measurements

Three samples of each membrane were subjected to 24-hour soaks in four different aqueous solutions containing 0.5 M $KHCO_3$ and either 0, 0.5, 1.5, or 2.5 M ethanol. Average solution uptake and swelling measurements of three samples for each test are shown, with their error bars representing standard deviation of the three samples. These tests were used to obtain accurate measurements of the average mass of solution took up during the preceding permeability measurements. **Figure 14** shows the average percent change in mass of membranes, where the increase in mass was purely due to the uptake of their surrounding solution. This uptake also corresponds to changes in dimensions of the membranes, shown later.

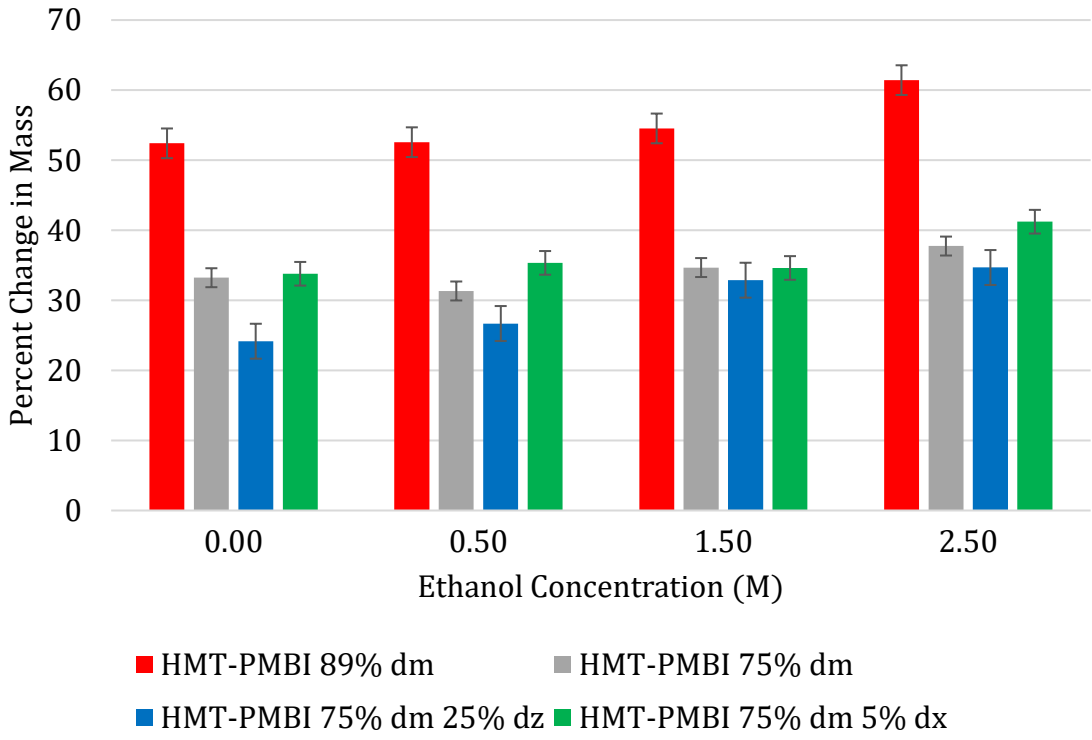

Figure 14. Solution uptake measurements using aqueous 0.5 M $KHCO_3$ solutions with 0 M, 0.5 M, 1.5 M, and 2.5 M solutions of ethanol.

Across all four membrane types, HMT-PMBI 89% had the highest solvent uptake at each ethanol concentration, increasing in mass by as much as 61% in 2.5 M ethanol. The membrane with the lowest experimental IEC, HMT-PMBI 75% dm 25% dz, also had the lowest percent change in mass at all ethanol concentrations, at nearly half that of HMT-PMBI 89% dm. HMT-PMBI 75% dm and HMT-PMBI 75% dm 5% dx showed comparable solvent uptake, with the crosslinked membrane having slightly higher solvent uptake. These findings show that a strong relationship between IEC and solvent uptake exists.

Using the same membranes, through-plane swelling was measured, yielding the average percent change in thickness in dry and wet membranes when exposed to the same four solutions as above. These changes are shown in **Figure 15**, below.

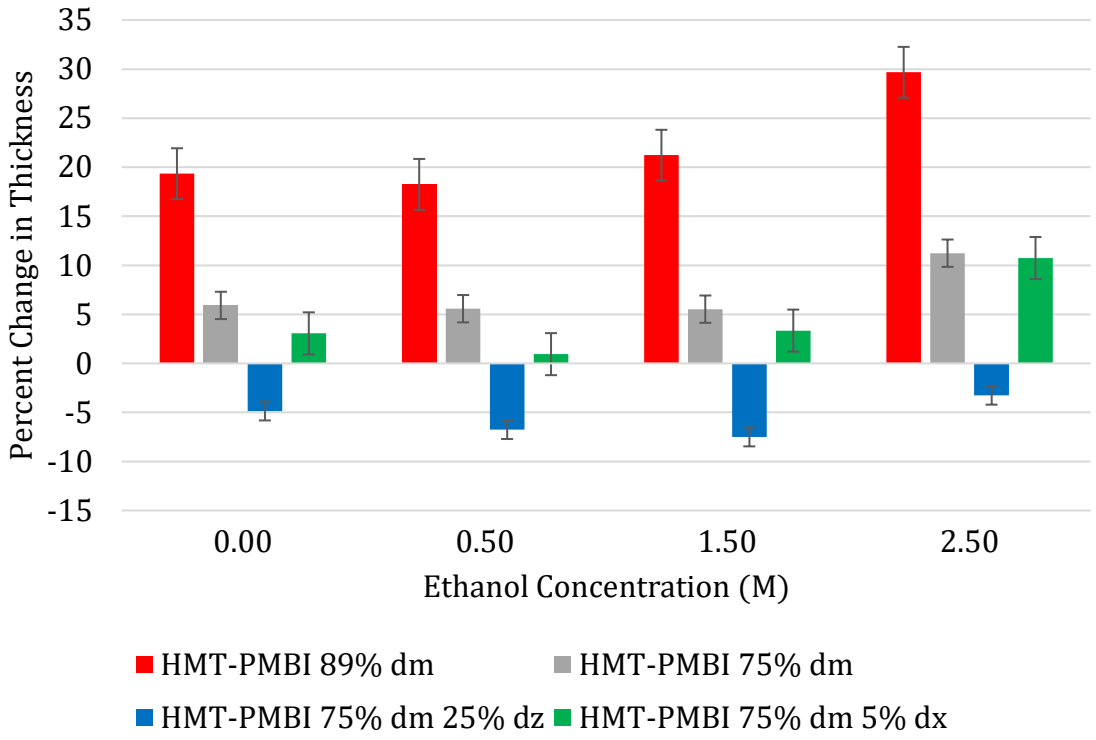

Figure 15. **In-plane swelling measurements were performed to measure the percent change in thickness of HMT-PMBI 89% dm (red), HMT-PMBI 75% dm (grey), HMT-PMBI 75% dm 25% dz (blue), and HMT-PMBI 75% dm 5% dx (green), when exposed to 0 M, 0.5 M, 1.5 M, and 2.5 M ethanol solutions with 0.5 M $KHCO_3$. Error is calculated by propagating the standard deviation on three measurements per membrane and three membranes for each membrane type at all four concentrations.**

HMT-PMBI 89% dm shows significant through-plane swelling, increasing in thickness by nearly 30% in 2.5 M ethanol. This is an increase in comparison to the swelling observed in the solution without ethanol, where HMT-PMBI 89% dm showed a swelling of nearly 20%. For HMT-PMBI 75% dm, a relatively large increase in swelling was seen from 0 M to 2.5 M ethanol, nearly doubling, from 5.9% to 11.2%. The difference in through-plane swelling between cross-linked HMT-PMBI 75% dm 5% dx and HMT-PMBI 75% dm was most notable in the 0.5 M ethanol solution, where the cross-linked membrane is significantly less. This indicates that the membrane contracted or condensed upon exposure to low concentrations of ethanol. There was no significant difference between HMT-PMBI 75% dm and cross-linked HMT-PMBI 75% dm 5% dx in 2.5 M ethanol. By far the most interesting result was the contraction of the zwitterion-functionalized HMT-PMBI 75% dm 25% dz. The membrane decreased in thickness for all solutions tested, with 1.5 M ethanol have a change in thickness of -7.5%. While this result could

decrease ethanol diffusion due to decreased free volume, this could also impede transport rate of water or ions that rely on osmotic drag as a means of conduction. Finally, the in-plane swelling in-plane swelling measurements are shown below in **Figure 16**.

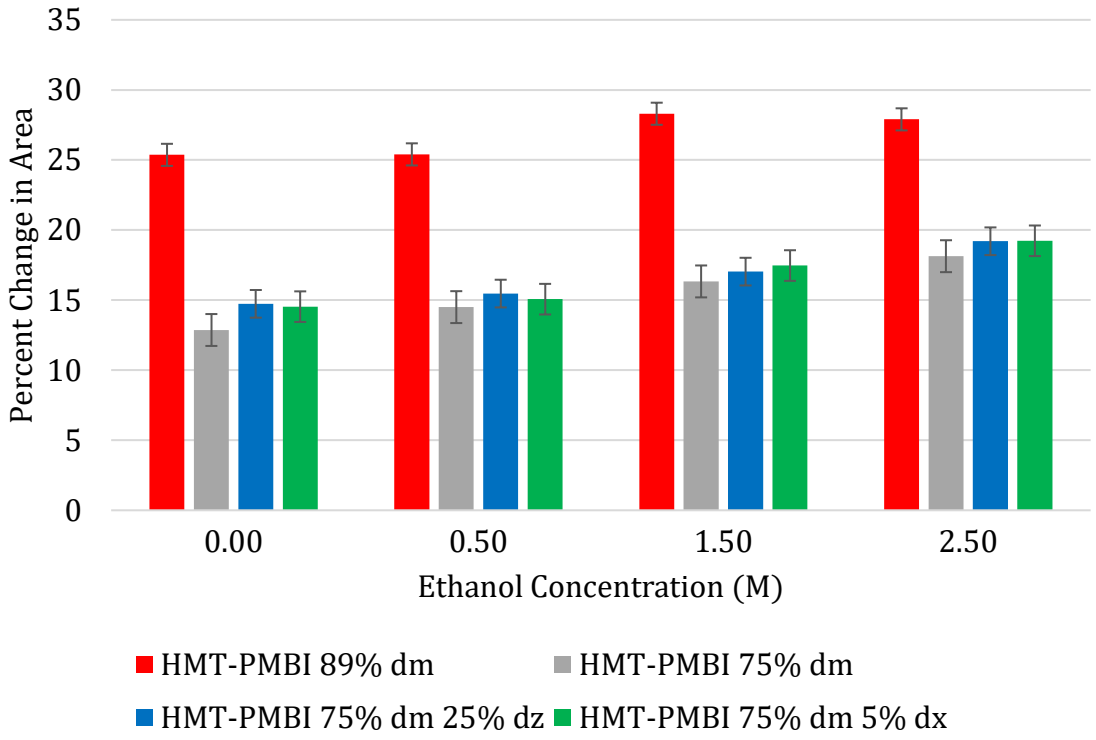

Figure 16. **The in-plane swelling (IPS) of each membrane was measured for membranes soaked in 0, 0.5, 1.5, and 2.5 M ethanol solutions. HMT-PMBI 89% dm showed the most significant swelling, at over 25% for each ethanol concentration. The other three membranes swelled very similarly all increasing with concentration of ethanol.**

HMT-PMBI 89% dm swelled significantly more in-plane in 0, 0.5, and 1.5 M ethanol, than compared to its through-plane swelling. The other three membranes swelled similarly in-plane for all ethanol concentrations and all increased with concentration.

These differences in in-plane swelling and through-plane swelling show there is directional dependence when HMT-PMBI membranes uptake ethanol solutions. This could be associated with the casting method used in this project. Morphology of membranes has shown to be influenced by casting methods and can be directionally unique.[81] One possible point of error comes from the device used to measure membrane thickness. The micrometer used has a mechanism which allows consistent pressure to be used on the sample being measured. This is an

excellent feature for stiff samples but could introduce bias with samples that are softer. HMT-PMBI is much less rigid and stiff when wet than when it is dry, which could suggest it softens. If HMT-PMBI 75% dm 25% dz softens significantly more than the other membranes tested, this could account for the interesting shrinking observed.

3.1.3. Tensile Measurements

The results for the tensile tests are presented below, first comparing the samples of the pristine membranes in **Figure 17**. Force is normalized by the cross-section of each membrane in the center of the dog bone shape. Elongation is given as a percent of the starting distance between the grips of the tensile measurement instrument. In almost all cases, Young's modulus, yield strength and ultimate strength are the average of three tests.

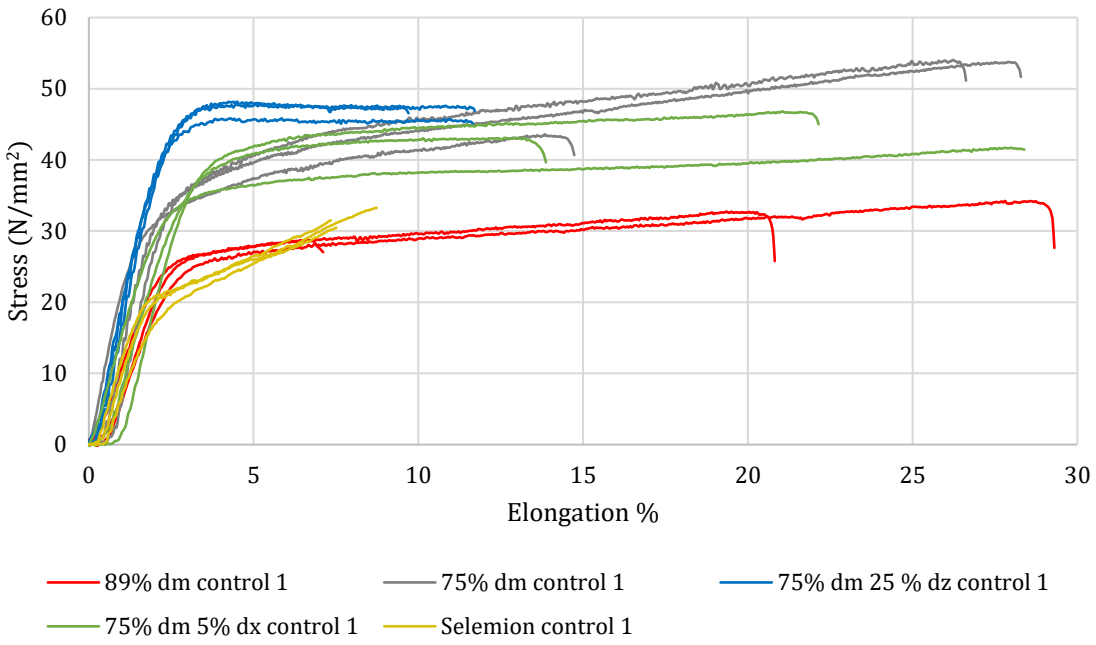

Figure 17. **Three samples of each membrane (HMT-PMBI 89% dm (red), HMT-PMBI 75% dm (dark grey), HMT-PMBI 75% dm 25% dz (blue), HMT-PMBI 75% dm 5% dx (green), and Selemion AMV (dark yellow)) are shown. Selemion has little ductile character, and a strain hardening effect is observed. HMT-PMBI 75% is both the strongest and most ductile of the three. HMT-PMBI 89% dm has higher strength than Selemion AMV and fails at a similar applied force, but has a lesser but similar ductility to HMT-PMBI 75% dm.**

Selemion AMV showed significant strain hardening when compared to HMT-PMBI-type membranes. Of the other membranes, HMT-PMBI 75% dm and 89% dm also showed some

strain-hardening. The two functionalized materials, HMT-PMBI 75% dm 25% dz and HMT-PMBI 75% dm 5% dx, showed very little or no strain-hardening. Selemion AMV had a lower yield strength of 18 MPa, when compared to the next weakest, HMT-PMBI 89% dm, at 23 MPa. HMT-PMBI 75% dm had a slightly lower yield strength compared to the cross-linked HMT-PMBI 75% dm 5% dx, at 29 and 32 MPa respectively. The zwitterion-functionalized membrane had the highest yield strength of all the membranes tested at 37 MPa.

Selemion AMV fractures at an elongation percent of around 7.3 – 8.6%, significantly lower than the zwitterion-functionalized HMT-PMBI 75% dm 25% dz, at around 11.5% elongation. Of the HMT-PMBI-type membranes, the weakest is HMT-PMBI 89% dm, with a yield strength around 25 $N \bullet mm^{-1}$. HMT-PMBI 89% dm has excellent elongation before fracture at 29%. HMT-PMBI 75% dm and HMT-PMBI 75% dm 5% dx also have similar elongation before fracture, around 28% for both. The zwitterion functionalization results in a significant reduction in elongation before fracture, with HMT-PMBI 75% dm 25% dz failing at around 11.7%.

The ultimate strength of most membranes presented just before a rapid onset of necking, followed by fracture. Selemion AMV and HMT-PMBI 75% dm 25% dz did not show signs of necking before fracture. Selemion AMV's ultimate strength was 31 MPa, just before fracture. HMT-PMBI 75% dm 25% dz had an ultimate strength of 47 MPa. The crosslinked HMT-PMBI 75% dm 5% dx had an ultimate strength of 43 MPa, just before rapid necking, and failure. The membrane with the highest ultimate strength was HMT-PMBI 75% dm at 50 MPa, just before failure.

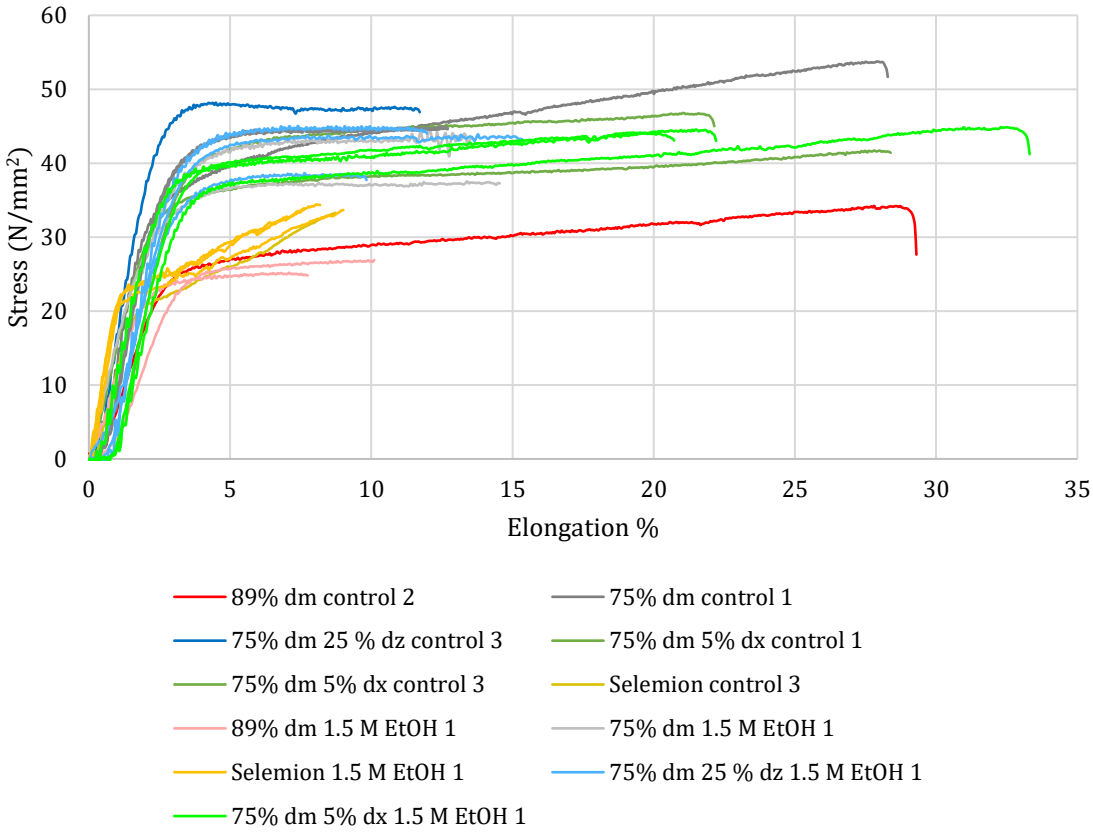

Figure 18. **After soaking in 1.5 M ethanol solution for 24 hours, then dried in ambient conditions. Three samples of each soaked membrane were tested, HMT-PMBI 89% dm shown in light red, HMT-PMBI 75% dm shown in light grey, and Selemion AMV shown in bright yellow.**

Figure 18 compares selected strength-strain curves for the control set of membranes to the same membranes after being soaked in 1.5 M ethanol. Evaluating the effects of soaking in ethanol gives insight into structural changes in the polymer that might occur in devices. Selemion AMV increases in strength upon exposure to ethanol, with an ultimate yield strength of 33 Pa, and nearly no change in elongation before failure. HMT-PMBI 89% dm suffers a significant loss in elongation before failure, occurring at a meager 10%, compared to the pristine membrane's nearly 30%. The yield strength and ultimate strength are only slightly decreased. HMT-PMBI 75% dm is affected similarly to 89% dm, with an elongation at break of half that of the pristine. It is important to note that over the course of drying Selemion samples in ambient conditions, some yellowing occurred, which could indicate degradation and loss in structural integrity. Nevertheless, it was the ideal choice to test the samples dry instead of wet, as each membrane could have a different rate of ethanol evaporation. Drying the samples decreased the number of uncontrollable variables.

Increased concentrations of ethanol solvate the membranes better. It is reasonable to assume a direct relationship between the concentration of ethanol a membrane is soaked in, and the change in strength and ductility from the pristine membrane. In **Figure 19**, the strain-stress curves of Selemion AMV membranes soaked in 0.5, 1.5, and 2.5 M ethanol solutions are shown.

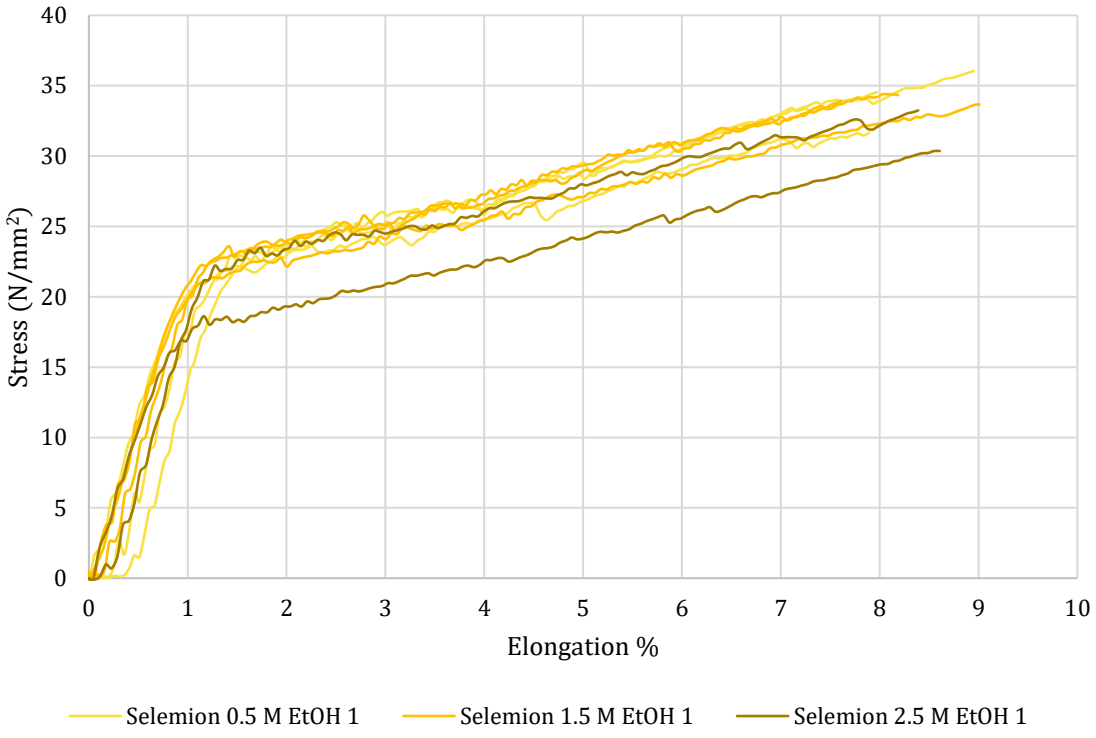

Figure 19. **Selemion samples exposed to 0.5, 1.5 and 2.5 M ethanol present a strengthening that seems to be unrelated to the concentration of ethanol solution. Selemion retains its significant strain hardnening, compared to HMT-PMBI. There is little difference in the elongation before failure of between each sample, within ~1%.**

Selemion AMV seems to be affected by all three concentrations of ethanol soak similarly. There is no trend in yield strength, ultimate strength, or elongation before failure between the samples. Selemion AMV membranes are crosslinked and have robust structural characteristics. This likely helps the membranes resist negative effects due to ethanol exposure.

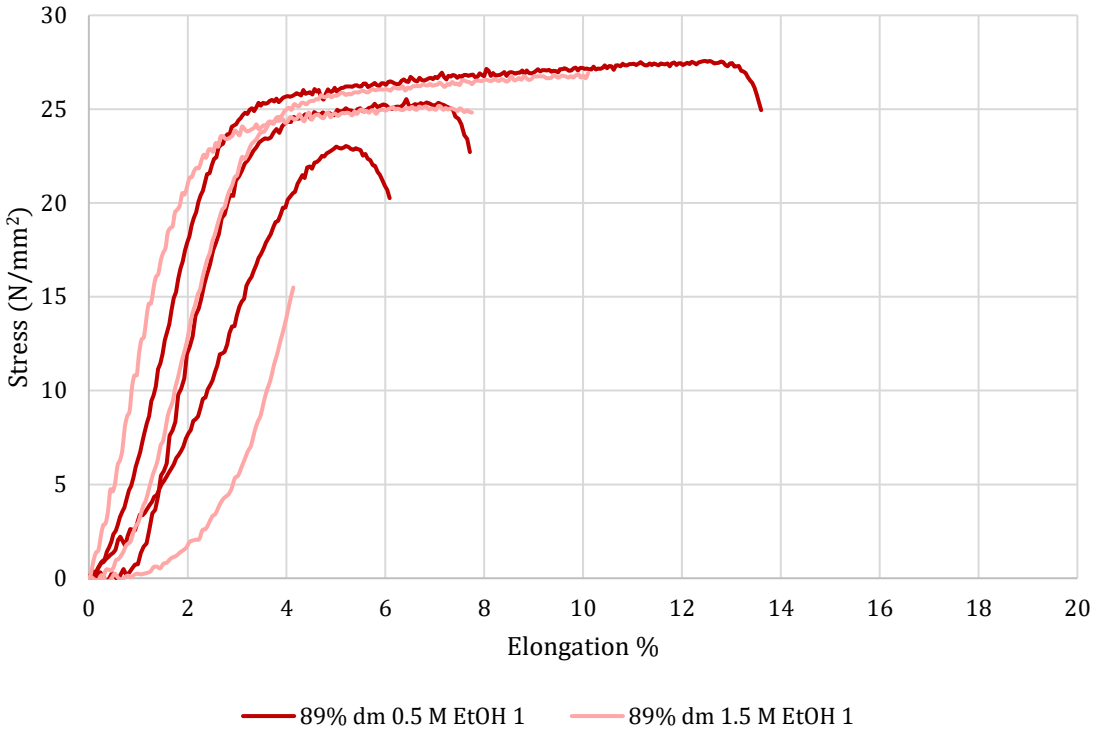

Figure 20. **The weakening effect on HMT-PMBI 89% dm of ethanol exposure is similar in both concentrations of ethanol, 0.5 (dark red) and 1.5 M (light red). HMT-PMBI 89% dm dissolved completely in 2.5 M ethanol over the course of about an hour, so there is no data for this case.**

Observed in **Figure 20**, HMT-PMBI 89% dm is weakened by both 0.5 M and 1.5 M ethanol soaks, both having similar yield strengths and ultimate strengths. The difference is observed in the elongation before failure, with the membranes soaked in 1.5 M ethanol having an elongation of 10.1%, and those soaked in 0.5 M ethanol having an elongation of 13.6%. The membranes soaked in 2.5 M ethanol were two weak to load into the instrument and had fused together during their soak and drying process.

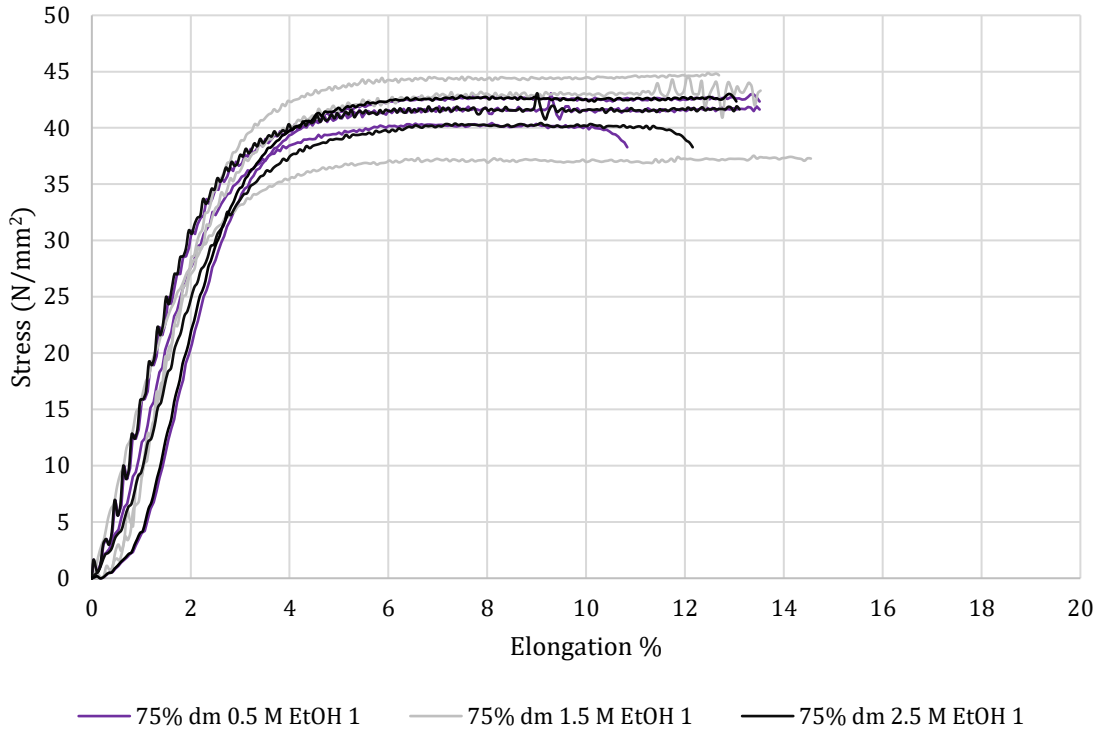

Figure 21. **Among the samples of HMT-PMBI 75% dm exposed to 0.5 (purple), 1.5 (light grey) and 2.5 M (black) ethanol, there is no obvious trend that relates to the concentration of ethanol. All samples exhibit a significant reduction in ductility and present a much flatter ductile region than the pristine sample.**

HMT-PMBI 75% dm membranes performed very well after exposure to ethanol of all three concentrations. Their stress-strain curves were largely independent of ethanol soaking. Despite seeing solvent uptake and swelling due to ethanol, the morphology or structure of the polymer chains within the membrane may resist change due to solvation better than HMT-PMBI 89% dm.

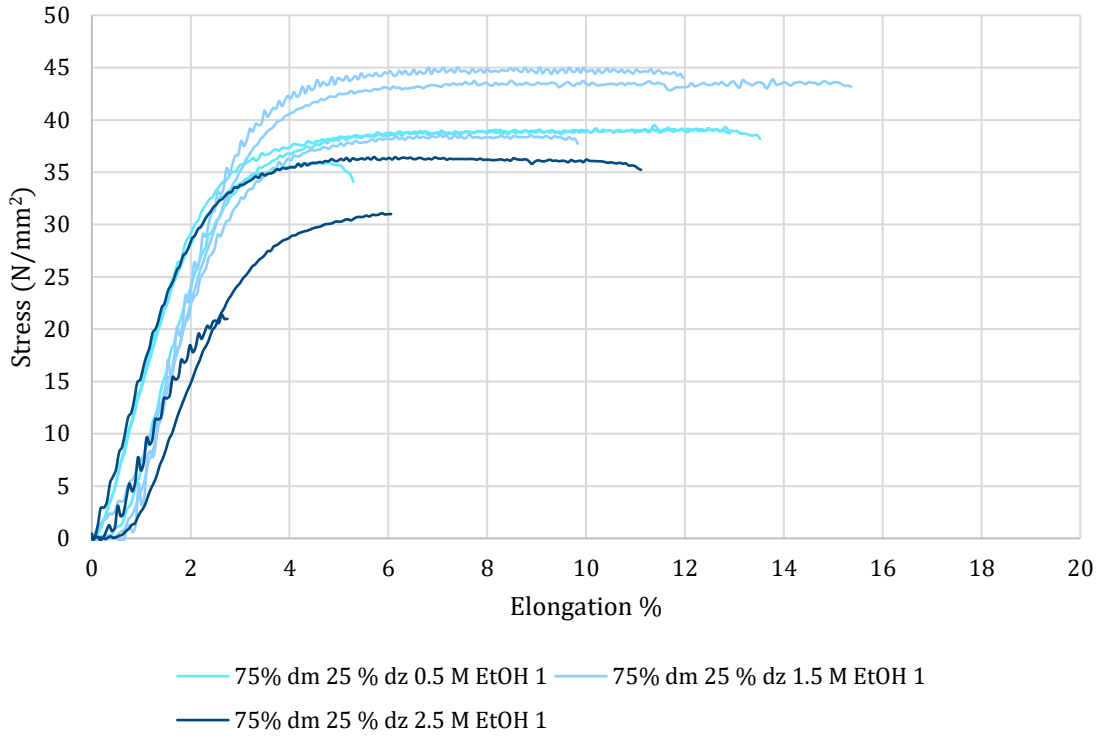

Figure 22. **Tensile tests were completed with HMT-PMBI 75% dm 5% dx after samples were soaked in 0.5 M, 1.5 M, and 2.5 M ethanol solutions. Three membranes were soaked in each concentration, with 0.5 M shown in neon blue, 1.5 M shown in light blue, and 2.5 M shown in dark blue.**

In contrast to the previous data, the zwitterion-functionalized HMT-PMBI 75% dm 25% dz **[Figure 22]** membrane shows significant decreases in the yield strength, ultimate strength, and elongation before failure, when exposed to ethanol solutions. Similar to the solution uptake experiment, the most interesting data comes from HMT-PMBI 75% dm 25% dz when exposed to 1.5 M ethanol. The membrane is more effected than 0.5 M and 2.5 M ethanol soaks than 1.5 M ethanol.

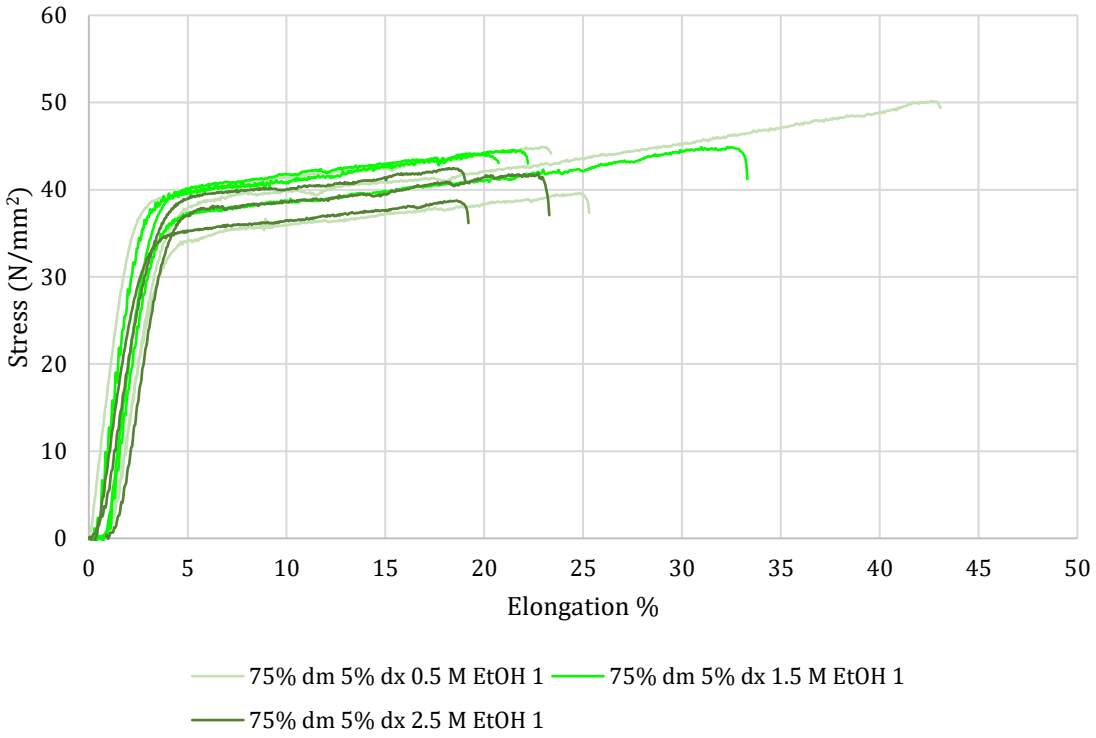

Figure 23. **HMT-PMBI 75% dm 5% dx was soaked in 0.5, 1.5, and 2.5 M ethanol solutions to assess the effects of ethanol on the tensile strength of the membrane upon exposure to ethanol.**

Lastly, the crosslinked HMT-PMBI 75% dm 5% dx **[Figure 23]** membranes proved to be robust and stable regardless of which concentration of ethanol they were soaked in. The crosslinking of HMT-PMBI 75% dm was expected to yield a membrane with increased yield strength and retain or improve on the robustness of the membrane upon exposure to ethanol. Unfortunately, this was not the case. This could be due to casting the crosslinked membrane as the crosslinking reaction is taking place, which could have significant effects on the morphology of the membrane, compared to pristine HMT-PMBI 75% dm.

A summary of all Young's moduli, yield strengths, and ultimate strengths are shown below in **Table 3**.

Table 3. All Young's moduli, yield strengths, and ultimate strengths have been averaged and are presented, with their respective standard deviations.

Membrane	Young's Modulus (N/m^2)				Yield Strength (MPa)				Ultimate Strength (Mpa)			
Ethanol Concentration	0	0.5	1.5	2.5	0	0.5	1.5	2.5	0	0.5	1.5	2.5
HMT-PMBI 89% dm	13 ±1	10 ±2	11 ±1	-	23 ±1	21 ±0	21± 1	-	31± 2	25± 2	26± 1	-
HMT-PMBI 75% dm	21 ±0	17 ±1	18 ±2	17 ±1	29 ±2	33 ±1	29± 3	31± 0	50± 5	42± 1	42± 3	42± 1
HMT-PMBI 75% dm 25% dz	22 ±0	17 ±0	17 ±2	13 ±2	37 ±1	29 ±0	32± 1	23± 4	47± 1	22± 0	42± 3	29± 7
HMT-PMBI 75% dm 5% dx	16 ±1	16 ±2	17 ±1	15 ±0	32 ±2	30 ±2	31± 1	29± 1	43± 2	44± 5	44± 0	41± 1
Selemion AMV	14 ±1	23 ±0	23 ±0	22 ±1	18 ±1	21 ±0	21± 0	19± 2	31± 1	34± 2	33± 0	31± 2

Over each of the membranes studied, HMT-PMBI 89% dm showed the harshest decrease in elongation before break, a metric that remains important to resisting the harsh environments within electrolysers. This is especially important for membranes like HMT-PMBI which could swell in CO_2 electrolysers, pushing themselves against the solid catalyst layers. While HMT-PMBI 75% dm 5% dx presented yield strengths and ultimate strengths compared to the uncrosslinked membrane, its elongation at break increased when exposed to ethanol, potentially increasing its robustness in an electrolyser. The zwitterion functionalized membrane possessed higher strength compared to all other membranes, which could prove useful during handling and assembly of electrolysers. However, its elongation before break is quite decreased compared to the other membranes studied.

3.2. Pulsed-Field Gradient NMR Experiments

Initial DOSY experiments with HMT-PMBI-type membranes were unsuccessful, as no useable signal was obtained. This was hypothesized to be due to: 1) membranes soaked in ethanol solutions were too thin and did not take up enough ethanol to quantify via NMR, and/or 2) membranes were too thin and while transferring them into the NMR tube, ethanol evaporated and continued to evaporate into the headspace of the NMR tube. The membranes were then dissolved and cast significantly thicker (roughly 300-400 μm). The thicker membranes solved issues with all HMT-PMBI membranes except HMT-PMBI 75% dm and Selemion AMV, which still had very weak signals for ethanol and water in the ^1H NMR spectra.

Before utilizing TopSpin's built-in DOSY experiment, two 1-dimensional experiments with a gradient strength (***gpz6***) of 2% and 95% were used to calibrate the values for Δ (**d20**) and δ (**p30**). This calibration method is discussed in detail in TopSpin's manual on DOSY experiments. Optimizing these parameters ensures that calculated diffusion coefficients are with as little error as possible, as shown in **Figure 24**.

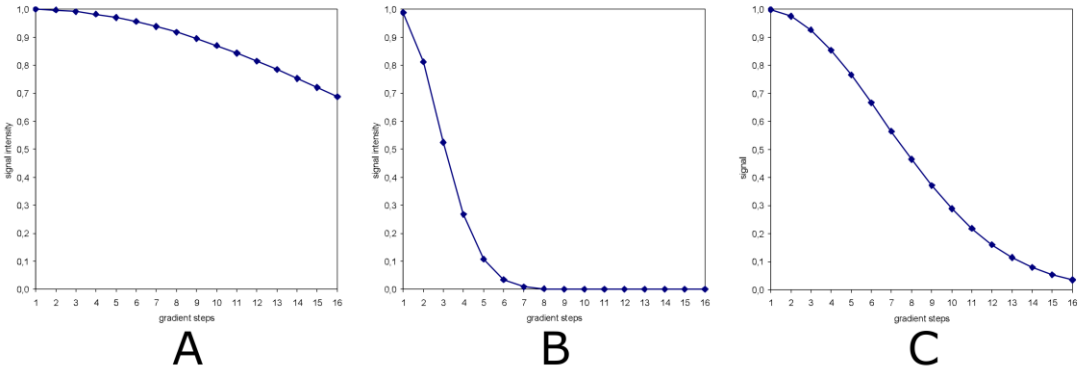

Figure 24. **As instructed in the TopSpin NMR manual for DOSY experiments (as of version 4.1.1), collecting spectra with too little signal attenuation (graph A) over the gradient steps, or too quick signal attenuation (graph B) can lead to poor accuracy when calculating the diffusion coefficient. Attenuation from 100% signal intensity to ~5% signal intensity over the number of gradient steps used is ideal for maximizing accuracy. The image is taken directly from the Bruker manual for DOSY experiments.**[82]

It is important to note that the gradients available were those built into the probe (Bruker 5mm QCI cryoprobe) and could not exceed 10 ms of total gradient use. This limited some of the experiments causing the ethanol's proton signals to not be fully attenuated, which could increase error on those measurements. The optimal parameters where chosen that maximized accuracy without overloading the gradient coils.

After optimal parameters were chosen, the DOSY experiment for each membrane type and varying concentration of ethanol was performed, the results are shown in **Figure 25**.

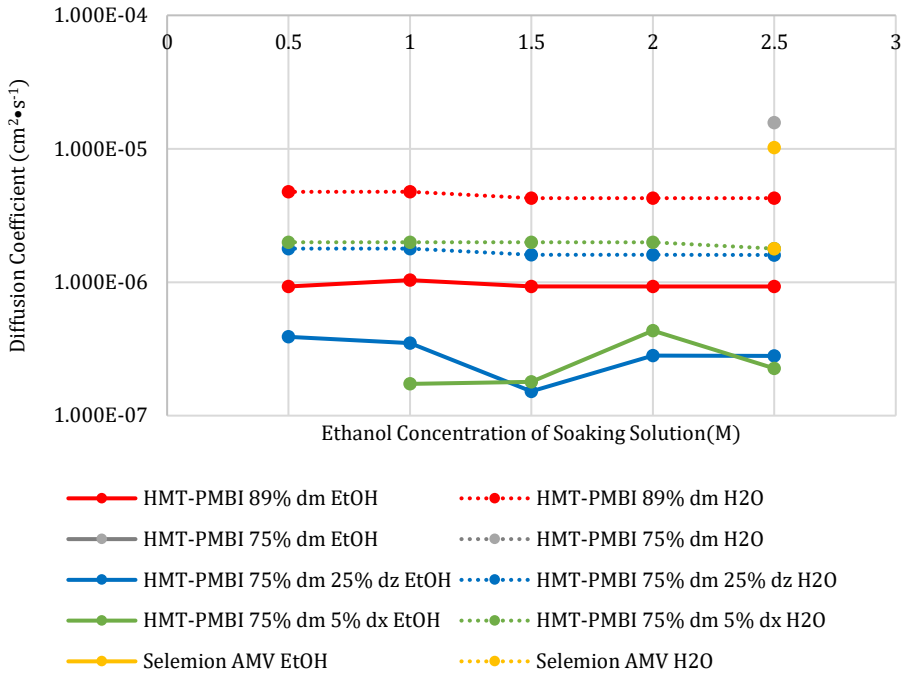

Figure 25. **A comparison of the diffusion coefficients of water and ethanol in HMT-PMBI type membranes and Selemion AMV. These coefficients are organized by membrane and are displayed as a function of the concentration of ethanol in the aqueous solution each membrane was soaked in before analysis. Unfortunately, Selemion AMV and HMT-PMBI 75% dm did not have strong enough ethanol and water signals to perform DOSY experiments on them more than what is displayed. This is also true for HMT-PMBI 75% dm 5% dx at 0.5 M ethanol.**

Diffusion coefficients change significantly for each of the functionalized materials. These DOSY measurements have highlighted that when no external forces are driving diffusion, ethanol has a variable diffusion coefficient that is not linearly dependent on the concentration of ethanol in which the membrane was soaked in before the experiment. While not immediately applicable to *in operando* conditions, the local minimum that is observed for both HMT-PMBI 75% dm 25% dz and HMT-PMBI 75% dm 5% dx, allows us to determine that these modifications do impede ethanol transport to some degree. An interesting result is that the diffusion coefficient for water appears not to change significantly over the ethanol concentration range tested.

Several studies that employed similar experimental methods with PFG NMR exist; successfully measuring diffusion coefficients of mobile ions and water in IEMs. With more specialized equipment, stronger gradients and quadrupolar nuclei, the orientation of water conduction channels have been proven to be dependent on the membrane casting conditions.[81] These experiments highlight the importance of spectroscopic techniques when studying molecular

dynamics in IEMs developed for electrochemical systems. It is likely that *in operando* PFG NMR techniques will be possible on functioning electrolysers in the future, as several groups around the world have developed such methods for lithium-ion battery systems.[83]

3.3. Permeability Measurements

3.3.1. Diffusion Driven by Concentration Gradients

Permeability measurements were completed using the H-cell shown in **Figure 11**. An ethanol solution of 0.5, 1.5, or 2.5 M with 0.5 M $KHCO_3$ was used as simulated catholyte, and 0.5 M $KHCO_3$ was used as simulated anolyte. Each experiment started with an initial ethanol concentration gradient (ΔC_i) of 0.5 M ($\Delta C_{i=0.5}$), 1.5 M ($\Delta C_{i=1.5}$), or 2.5 M ($\Delta C_{i=2.5}$). The membranes tested separated the catholyte (high ethanol concentration) from the anolyte (0 ethanol concentration). The concentration gradient introduced drove ethanol to diffuse from high to low concentration, as shown in **Figure 26**. The concentration of ethanol in both sections of the H-cell was monitored every hour, for four hours, using quantitative NMR. As mentioned in **2.6.2**, the flux of ethanol (J_{EtOH}) is either the rate of ethanol leaving the catholyte or the rate of ethanol entering the anolyte. This is due to the uptake of ethanol observed in the previous chapters. For clarity, when referring to flux, the distinction will be made between the flux as calculated using the rate of ethanol leaving the catholyte ($J_{EtOH\text{-}Cat}$) and flux calculated using the rate of ethanol entering the anolyte ($J_{EtOH\text{-}An}$).

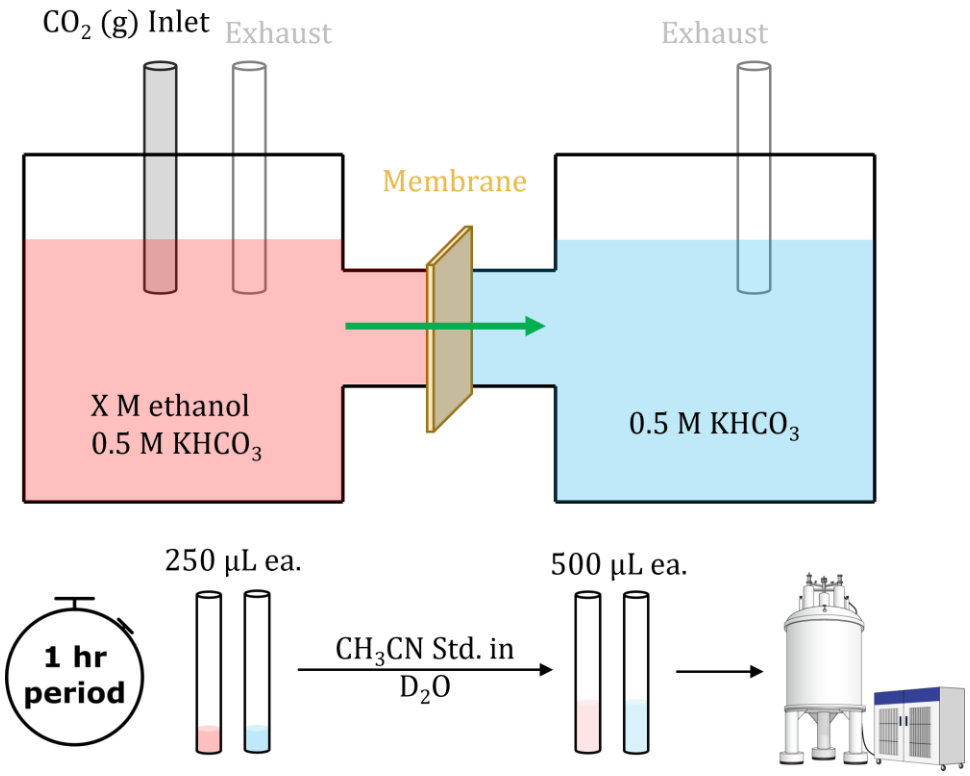

Figure 26. **A diagram showing the workflw of the permeability experiments. The red section on the left represents the catholyte which has, for example, "X" M ethanol and 0.5 M $KHCO_3$ to simulate the catholyte in an electrolyser. CO_2 is bubbled throughout the experiment into the catholyte, similar to a working electrolyser. The blue section on the right represents the anolyte which begins each experiment with no ethanol, and only 0.5 M $KHCO_3$, simulating the anolyte in an electrolyser. A membrane, shown in yellow, separates the two solutions. The concentration gradient established across the membrane drives the diffusion of ethanol in the direction of the green arrow, from high to low concentration. The concentration of ethanol in the high concentration and low concentration sections is monitored every hour, over four hours, using quantitative NMR.**

The first set of permeability measurements evaluate diffusion driven by a concentration gradient. The dependence of the diffusion coefficient of ethanol on the magnitude of the concentration gradient was evaluated for each membrane type. Results are presented first as two graphs for each membrane type, showing the concentration of ethanol in the catholyte and anolyte at three different concentration gradients. Due to ethanol-water solutions being effective plasticizers of HMT-PMBI, it is expected that the membrane's morphology will change upon exposure to these solutions. These morphological changes could decrease the membrane's ability to prevent ethanol transport. To assess this, permeability tests using HMT-PMBI 89% dm, HMT-PMBI 75% dm, HMT-PMBI 75% dm 25% dz, HMT-PMBI 75% dm 5% dx, and Selemion AMV

were performed with initial concentration gradients $\Delta C_{i=0.5}$, $\Delta C_{i=1.5}$, and $\Delta C_{i=2.5}$. . The graphs show the catholyte and anolyte ethanol concentrations during each of the three tests, for each membrane. The diffusion coefficient calculated for ethanol for each ΔC_i is shown, for each membrane.

Three permeability tests with using HMT-PMBI 89% are shown below in **Figure 27**, with the upper three sets of data corresponding to the measured ethanol concentration in the catholyte of the tests with $\Delta C_{i=0.5}$, $\Delta C_{i=1.5}$, and $\Delta C_{i=2.5}$ (from bottom to top, respectively). The lower three sets of data correspond to the measured ethanol concentration in the anolyte of the same three tests. One immediate observation is that the measured ethanol concentration in the catholytes do not match the actual concentrations of the solutions. This was later determined to be due both the high vapour pressure of ethanol and to the high partial pressure of CO_2 dissolved in the catholyte, due to the bubbling of CO_2 before and during the experiment. Later experiments have significantly more accurate measured concentrations once methods to acclimatize the micropipette were used. Another observation that coincides with this is the low surface tension observed of samples taken from the catholyte versus the anolyte. Calculating the diffusion coefficient of ethanol depends on knowing the concentration gradient across the membrane. This observed bias must be corrected for before calculating diffusion coefficients. The bias introduced is fairly consistent throughout the entire experiment due to the linearity of the data. A correction to the y-values for the permeability experiments is discussed after review of the first data sets.

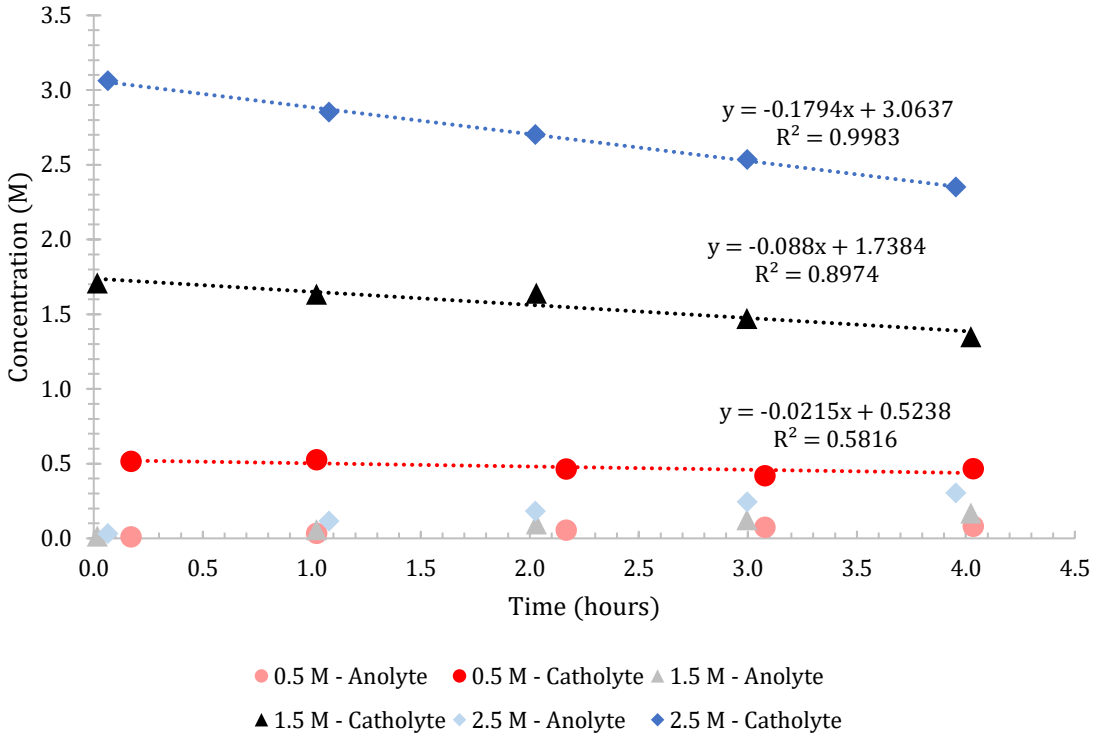

Figure 27. **Ethanol concentrations in the catholyte and anolyte as it diffused across HMT-PMBI 89% dm with catholytes having ethanol concentrations of 0.5, 1.5, & 2.5 M, with a supporting electrolyte of 0.5 M $KHCO_3$ and continuous bubbling of CO_2 in the catholyte. No current was applied, the only driving force for diffusion is the concentration gradient across the membrane. The bottom set of data points that lack linear trendlines are the concentrations of ethanol in the anolytes, with matching emblems.**

As is expected, increasing ethanol concentrations cause a higher rate of ethanol diffusion. From the Nernst-Planck flux equations, this relationship should be linear. Above in **Figure 27**, the rate of ethanol transport, as measured by the ethanol concentration in the catholyte, increases by just over four times, despite the starting ethanol concentration only increasing to $\Delta C_{i=1.5}$ from $\Delta C_{i=0.5}$, a three-fold increase. The increase from $\Delta C_{i=1.5}$ to $\Delta C_{i=2.5}$ would be expected to bring 1.66 times increase in the rate of ethanol diffusion, however, an increase of over 2 times is observed. These are the first indications that HMT-PMBI 89% dm suffers to effectively prevent ethanol permeation, the permeability increases nonlinearly as ethanol concentration increases. Shown below in **Figure 28** is a magnified view of the anolyte concentrations from **Figure 27**. Overall, significantly higher linearity is observed in anolyte concentration measurements.

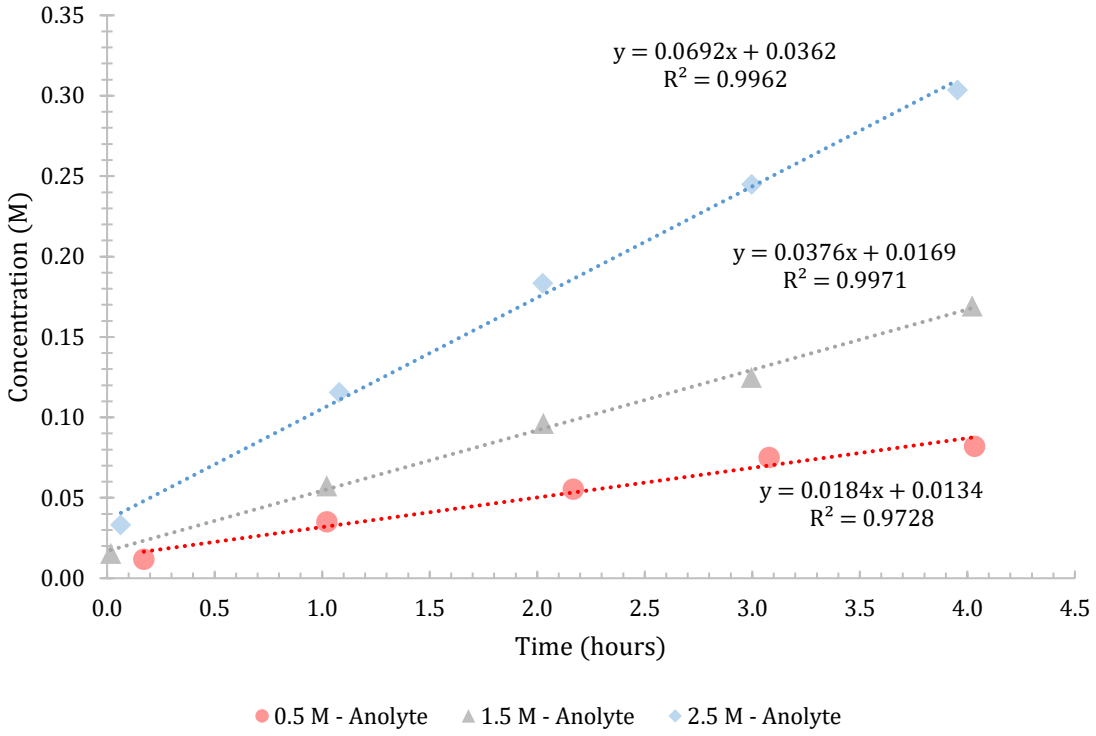

Figure 28. **The ethanol concentration in the anolyte as it diffused through HMT-PMBI 89% dm with starting catholyte concentrations of 0.5, 1.5, & 2.5 M ethanol. No current was applied, the only driving force for diffusion was the concentration gradient across the membrane.**

Interestingly, when looking at the same permeability tests as in **Figure 27**, but measuring the ethanol concentration in the anolyte, very different rates of diffusion were observed. The rate of ethanol influx to the anolyte ($J_{EtOH\text{-}An}$) should be equal and opposite of the rate of outflux from the catholyte ($J_{EtOH\text{-}Cat}$). For the test using $\Delta C_{i=0.5}$ ethanol, $J_{EtOH\text{-}An}$ is 85% that of $J_{EtOH\text{-}Cat}$. This discrepancy is quite large and becomes more severe with the tests with $\Delta C_{i=1.5}$ and $\Delta C_{i=2.5}$ ethanol. Initially, this discrepancy was thought to be due to ethanol evaporation, but a control test without a membrane discounted that theory. Without a membrane present in the H-cell, the total amount of ethanol in the H-cell remained constant. This confirmed that the membrane was absorbing ethanol from the catholyte. As observed in the preceding solvent uptake measurements, HMT-PMBI 89% dm absorbs higher amounts of ethanol solution when exposed to higher concentrations, which could be the cause of the non-linear behaviour regarding the ethanol transport rate observed in both the catholyte and anolyte.

When comparing the $J_{EtOH\text{-}Cat}$ to $J_{EtOH\text{-}An}$, the discrepancy between these values increases with concentration rapidly. This is proposed to be due to higher solvent uptake of these membranes at increasing ethanol concentrations, presented in **3.1.2**.

As detailed in **2.6.2**, calculating the diffusion coefficient relies on the slope of either the catholyte or anolyte ethanol concentration and the concentration gradient across the membrane, which necessitates accurate values for the concentration of ethanol in both the catholyte and anolyte. The bias introduced by dissolved CO_2 and/or ethanol vapour pressure had to be corrected.

To counteract the bias that caused the apparent increase in ethanol concentration in catholyte samples, the y-values were decreased by a fixed value, equal to the difference between the first measurement and their true starting concentration (0.5, 1.5, or 2.5 M). The concentration of the catholyte stock solutions were confirmed as accurate over the course of the project. The slope for the raw data was retained and the slope-intercept form of the linear regression was used to calculate the y-value at the beginning of the experiment, 30 minutes before the first data point ($x = -0.5$). The difference between this value and the stock solution concentration was used to offset all points. After this correction was applied to all experiments, **Figure 27** and **Figure 28** are reproduced as **Figure 29** and **Figure 30** below. This correction allowed for accurate calculation of the diffusion coefficients for all experiments, without altering the rate of diffusion observed in the experiments.

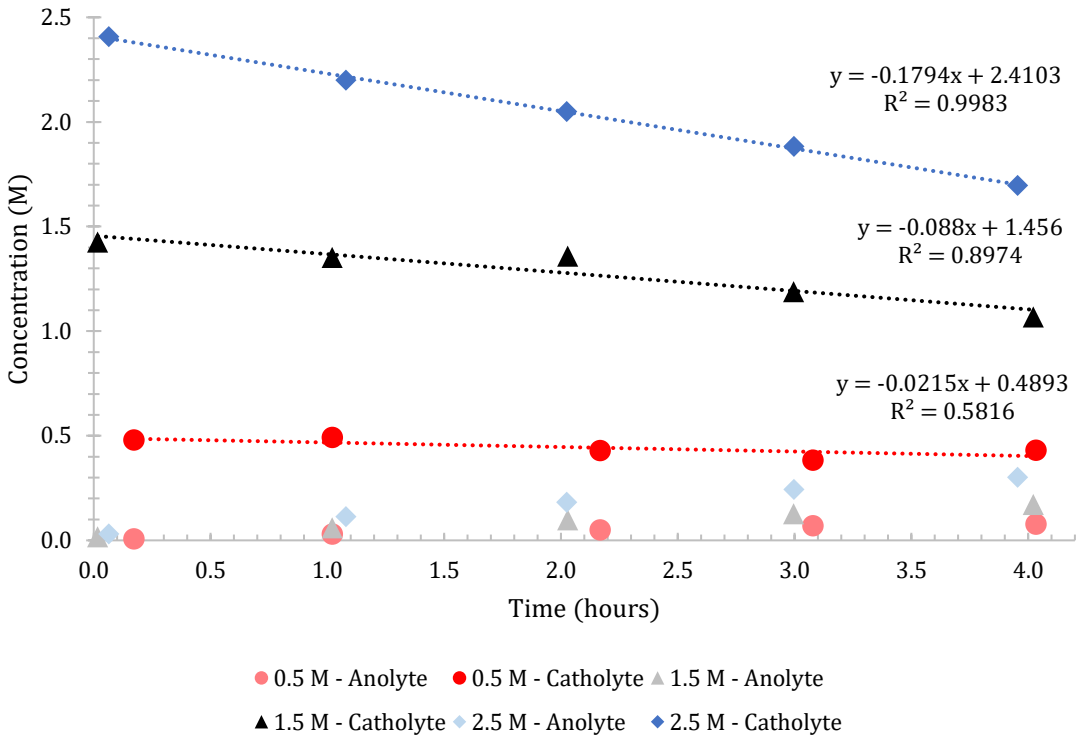

Figure 29. **Permeability tests of ethanol through ~25 µm HMT-PMBI 89% dm with 0.5, 1.5, & 2.5 M ethanol concentration gradients. The top three data sets in red, black, and blue, represent the concentration of ethanol in the catholyte. The bottom three data sets in rose, grey, and light blue, represent the concentration of ethanol in the anolyte of the experiments with corresponding colors. No electric current was used. A supporting electrolyte of 0.5 M $KHCO_3$ was used and continuous bubbling of CO_2 in the catholyte.**

After applying the correction, the starting ethanol concentrations in the catholyte matched the measured ethanol concentrations in the stock solutions. For the test which used $\Delta C_{i=0.5}$, the difference in concentration of ethanol in the catholyte and anolyte at each time interval was minimal. This changes drastically when comparing the tests that used $\Delta C_{i=1.5}$ and $\Delta C_{i=2.5}$, where the sum of ethanol in both the catholyte and anolyte do not account for the ethanol initially introduced into the H-cell. This further confirmed that despite the correction used, ethanol from the catholyte became trapped in the membrane on its way to the anolyte.

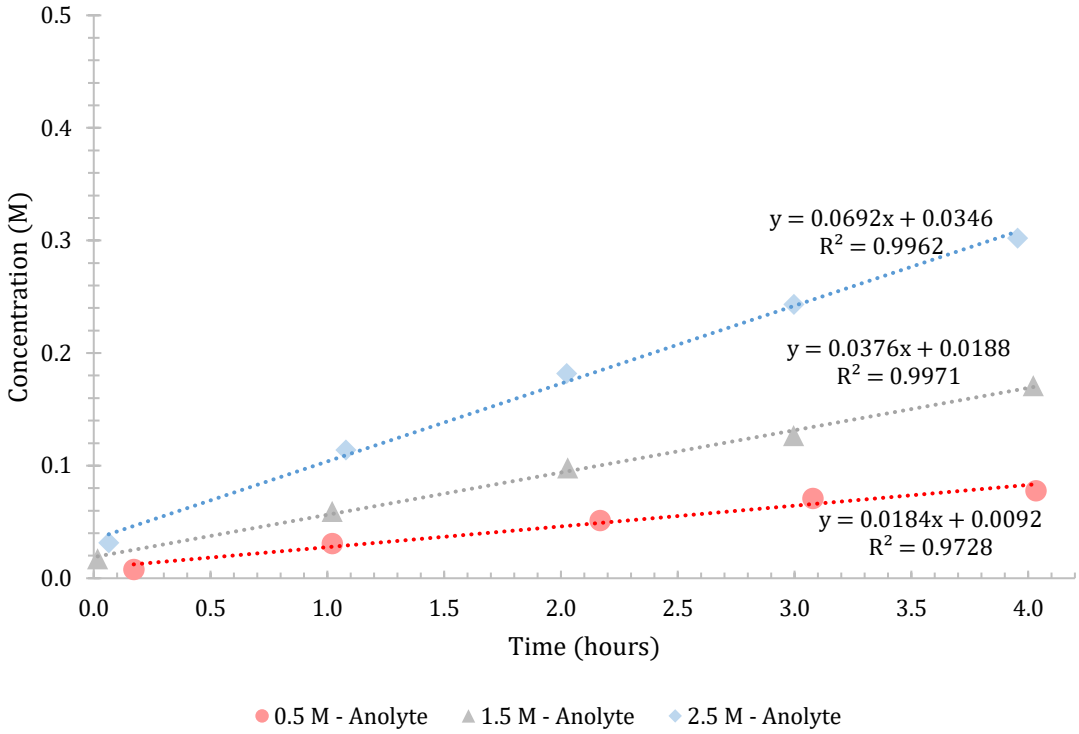

Figure 30. **Permeability tests of ethanol through ~25 µm HMT-PMBI 89% dm with 0.5, 1.5, & 2.5 M ethanol concentration gradients. The three data sets in rose, grey, and light blue, represent the concentration of ethanol in the anolyte of the experiments with corresponding colors. No electric current was used. A supporting electrolyte of 0.5 M $KHCO_3$ was used and continuous bubbling of CO_2 in the catholyte.**

With the corrections made to all data from the permeability measurements collected, a diffusion coefficient of ethanol was calculated for each period, using **Figure 30**.

$$D = -J\frac{dC}{dx} = -\frac{m \cdot 0.02}{0.000237}\frac{(C_n - C_{n-1})}{x_{mem}}$$

Equation 21. **The differential equation that describes the diffusion coefficient using Fick's first law can be simplified such that the flux is equal to the slope of the change in ethanol concentration in the catholyte (or anolyte) over time (in seconds), multiplied by the volume of vessel (in this case 20 mL), and divided by the area of membrane through which the ethanol diffused. The change in concentration from one point to the next (C_n-C_{n-1}) is divided by the thickness of the membrane (x_{mem}) to yield the diffusion coefficient.**

Diffusion coefficients calculated using both the catholyte flux ($D_{EtOH\text{-}Cat}$) and anolyte flux ($D_{EtOH\text{-}An}$) were compared. Drastically different values are observed and are plotted in **Figure 31** as a function of experiment run-time.

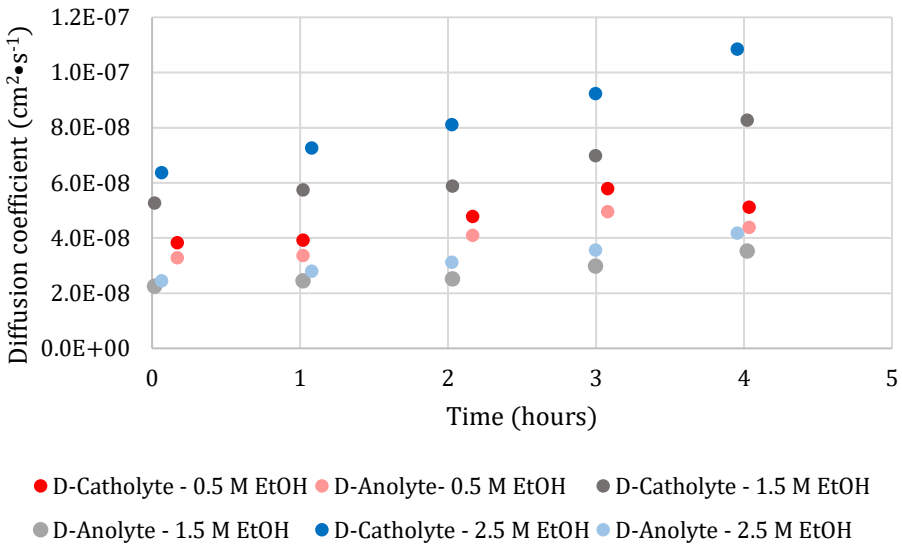

Figure 31. **Diffusion coefficients of ethanol through HMT-PMBI 89% dm as a function of time. Diffusion coefficients are calculated using either the flux using the anolyte or catholyte concentration, and are shown as either a faded or darker color, depending on whether they are caluclated using flux calculated from the anolyte or catholyte, respectively.**

This was the first evidence that the diffusion of ethanol through HMT-PMBI type membranes does not occur at a steady state. Steady state diffusion results in a single diffusion coefficient no matter the time which has passed. Steady state diffusion follows Fick's first law. For some systems, diffusion can begin as non-steady state but stabilizes at a single diffusion coefficient as time increases. What was observed in HMT-PMBI 89% dm is a diffusion coefficient which is changing nonlinearly, as observed in **Figure 31**. This confirms that diffusion of ethanol through HMT-PMBI 89% dm is non-steady state. This drastic change in diffusion coefficient indicates that processes within the membrane have taken place over the four-hour period which have increased the rate at which ethanol can diffuse. To evaluate the intensity of this change in diffusion for other membrane chemistries, each membrane type was submitted to a similar set up experiments.

The set of data in **Figure 31** showing the diffusion coefficient calculated using $J_{EtOH\text{-}Cat}$ shows a correlation between ΔC_i and calculated diffusion coefficient. This is not observed in the diffusion coefficients calculated using $J_{EtOH\text{-}An}$. $D_{EtOH\text{-}An}$ was highest for the test with $\Delta C_{i=0.5}$. For this same test, $D_{EtOH\text{-}Cat}$ and $D_{EtOH\text{-}An}$ were closest, suggesting that at low ethanol concentration, HMT-PMBI 89% acted closer to an ideal membrane. This is not observed in the tests with $\Delta C_{i=1.5}$ and $\Delta C_{i=2.5}$.

Based on the findings of the ex-situ measurements, it was expected that the difference between $D_{EtOH\text{-}An}$ and $D_{EtOH\text{-}Cat}$ for the test with $\Delta C_{i=1.5}$ should increase, it was not expected for $D_{EtOH\text{-}An}$ to decrease compared to the test with $\Delta C_{i=0.5}$. This finding was even more puzzling after observing an increase in D_{EtOH} for the test with $\Delta C_{i=2.5}$, that was, until the findings of the DOSY experiments were reviewed. It was found that at 1.5 M ethanol, HMT-PMBI 89% did have a minimum D_{EtOH}. This may suggest that both the DOSY and permeability experiments corroborate the finding that HMT-PMBI 89% dm has decreased ethanol permeability when exposed to 1.5 M ethanol.

Permeability tests with HMT-PMBI 75% dm are shown below in **Figure 32**, and demonstrates that HMT-PMBI 75% dm was less permeable to ethanol than HMT-PMBI 89% dm, especially at higher ethanol concentrations. There was a smaller difference between the rate of diffusion in the tests with 1.5 M ethanol and 2.5 M ethanol for HMT-PMBI 75% dm, compared to HMT-PMBI 89% dm. This could indicate that HMT-PMBI 75% dm retains its ability to exclude ethanol at higher concentrations than HMT-PMBI 89% dm.

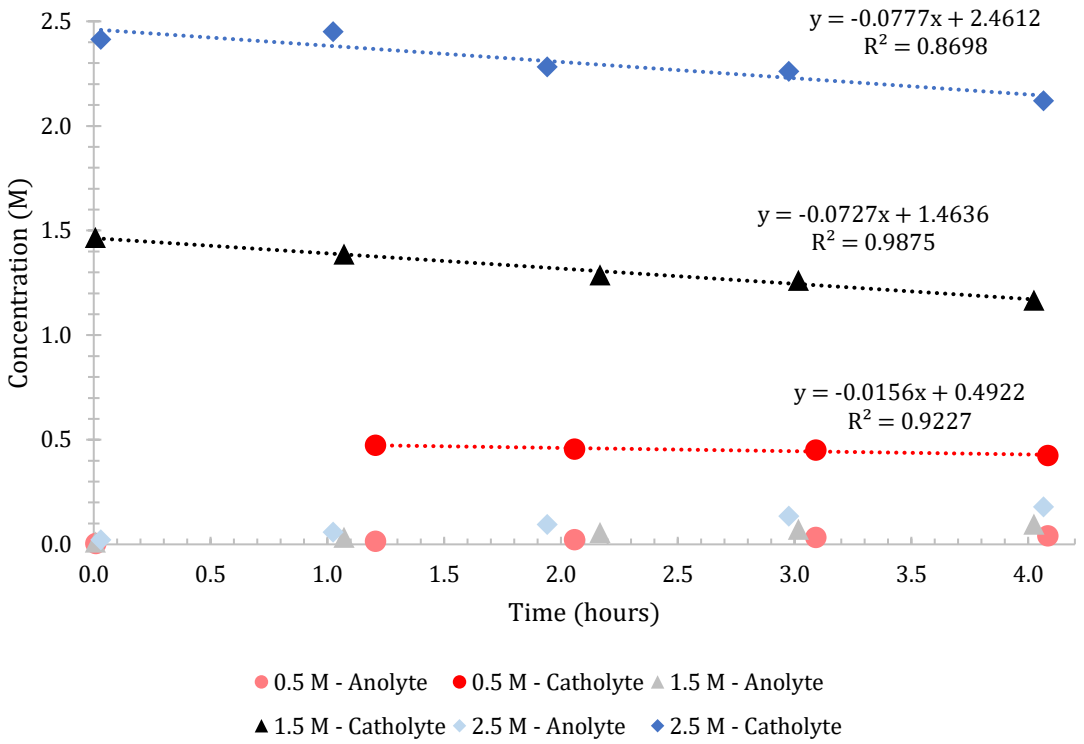

Figure 32. **Permeability tests of ethanol through ~25 µm HMT-PMBI 75% dm with 0.5, 1.5, & 2.5 M ethanol concentration gradients. The top three data sets in red, black, and blue, represent the concentration of ethanol in the catholyte. The bottom three data sets in rose, grey, and light blue, represent the concentration of ethanol in the anolyte of the experiments with corresponding colors. No electric current was used. A supporting electrolyte of 0.5 M $KHCO_3$ was used and continuous bubbling of CO_2 in the catholyte.**

The first point in the permeability test with $\Delta C_{i=0.5}$ was rejected as an outlier. An increase in $J_{EtOH\text{-}Cat}$ was observed between the experiment with $\Delta C_{i=0.5}$ and $\Delta C_{i=1.5}$. There was a significantly smaller difference observed in $J_{EtOH\text{-}Cat}$ between the experiment with $\Delta C_{i=1.5}$ and $\Delta C_{i=2.5}$. This may imply that HMT-PMBI 75% dm requires a higher ethanol concentration to observe the flux increases seen in the HMT-PMBI 89% [**Figure 29**]. However, this could also suggest an error in either the 1.5 M or 2.5 M test.

As seen with HMT-PMBI 89% dm, the R^2 of the anolyte ethanol concentration curves are significantly higher than their catholyte counterparts. $J_{EtOH\text{-}An}$ observed in **Figure 33**, doubles as ethanol concentration increases, similar to what is observed in $J_{EtOH\text{-}An}$ for HMT-PMBI 89% dm [**Figure 30**], but with lower values.

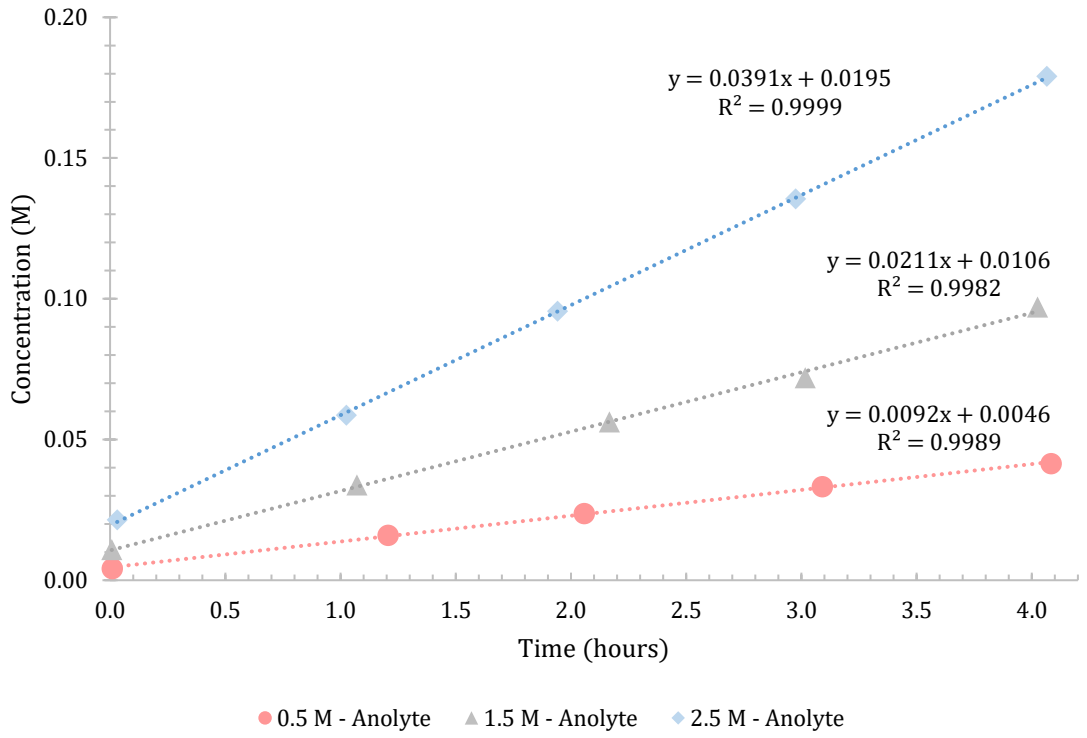

Figure 33. **Permeability tests of ethanol through ~25 µm HMT-PMBI 75% dm with 0.5, 1.5, & 2.5 M ethanol concentration gradients. The three data sets in rose, grey, and light blue, represent the concentration of ethanol in the anolyte of the experiments with corresponding colors. No electric current was used. A supporting electrolyte of 0.5 M $KHCO_3$ was used and continuous bubbling of CO_2 in the catholyte.**

As with the previous membrane, the diffusion coefficient changed over the course of the 4-hour experiment, as is illustrated in **Figure 34**. The change in diffusion coefficient for HMT-PMBI 75% dm was found to be more linear over the time scale of the experiment. The largest increase in diffusion coefficient for HMT-PMBI 75% dm over four hours was ~1.2×10^{-8} cm^2/s, compared to nearly 4.6×10^{-8}. This suggests that the processes which occurred in HMT-PMBI 89% dm, which drastically increased the diffusion coefficient, could be slowed or reduced in HMT-PMBI 75% dm.

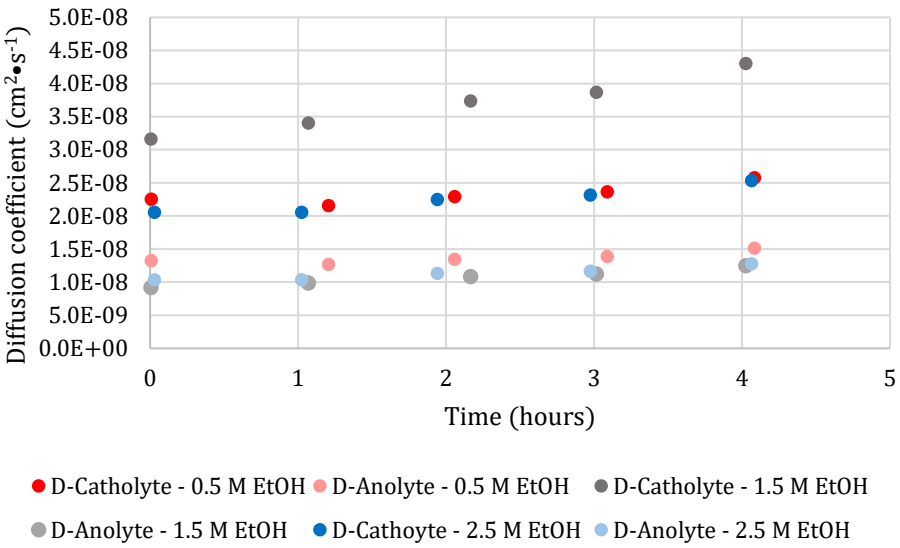

Figure 34. **Diffusion coefficients of ethanol through HMT-PMBI 75% dm as a function of time. Diffusion coefficients are calculated using either the flux using the anolyte or catholyte concentration, and are shown as either a faded or darker color, depending on whether they are caluclated using flux calculated from the anolyte or catholyte, respectively.**

As was observed with the $J_{EtOH-Cat}$ in **Figure 32**, a large discrepancy between the curves for the tests with $\Delta C_{i=1.5}$ and $\Delta C_{i=2.5}$ is observed. The data in **Figure 34** is a function of $J_{EtOH-Cat}$. This could imply an error in either test, however, a pinhole in the membrane used in the $\Delta C_{i=1.5}$ test could account for increased flux, drastically inflating the diffusion coefficient. Permeability tested using the zwitterion-functionalized HMT-PMBI 75% dm 25% dz were conducted to evaluate its effectiveness at abating ethanol crossover. Due to the low experimental IEC_{Cl-}, the membrane is hypothesized to ionically crosslink, neutralizing by polymer-polymer ionic bonds, rather than ionic bonds with sodium and chloride. As discussed in **1.4**, zwitterion-functionalized membranes have shown increased effectiveness at decreasing neutral product crossover. HMT-PMBI 75% dm 25% dz showed low solution uptake and swelling measurements, which was hypothesized to translate to lower ethanol diffusion. The results for permeability tests using HMT-PMBI 75% dm 25% dz are shown below in **Figure 35**, **Figure 36**, and **Figure 37**.

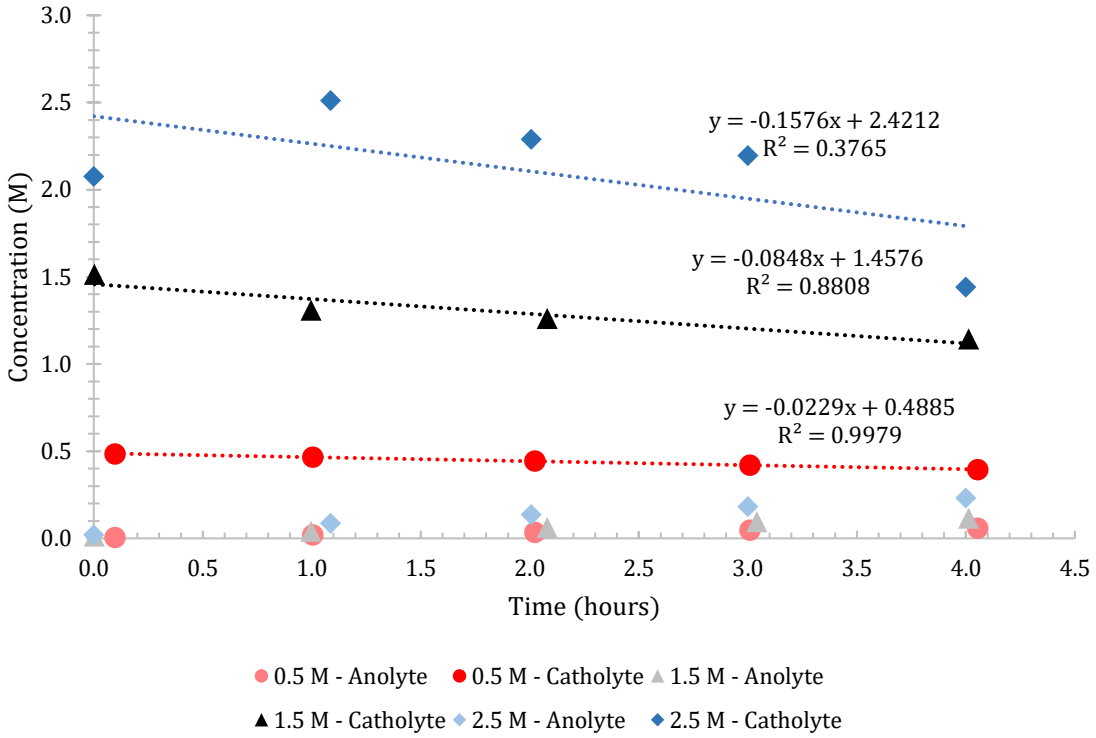

Figure 35. **Permeability tests of ethanol through ~25 µm HMT-PMBI 75% dm 25 % dz with 0.5, 1.5, & 2.5 M ethanol concentration gradients. The top three data sets in red, black, and blue, represent the concentration of ethanol in the catholyte. The bottom three data sets in rose, grey, and light blue, represent the concentration of ethanol in the anolyte of the experiments with corresponding colors. No electric current was used. A supporting electrolyte of 0.5 M $KHCO_3$ was used and continuous bubbling of CO_2 in the catholyte.**

Unfortunately, the data collected for the ethanol concentration in the catholyte of the experiments that used $\Delta C_{i=1.5}$ and $\Delta C_{i=2.5}$ was sub-optimal, as some of the sample at 0 and 4 hours was collected incorrectly. Nevertheless, it seems that $J_{EtOH\text{-}Cat}$ about doubled as ΔC_i increased. The values for $J_{EtOH\text{-}Cat}$ were similar to that of HMT-PMBI 89%. It is difficult to make conclusions regarding the rate at which ethanol diffused into the membrane from the catholyte due to the poor R^2 values for the experiments with $\Delta C_{i=1.5}$ and $\Delta C_{i=2.5}$. Luckily, as was observed with the previous tests, the data for the ethanol concentrations in the anolyte is significantly better, as shown in **Figure 36**.

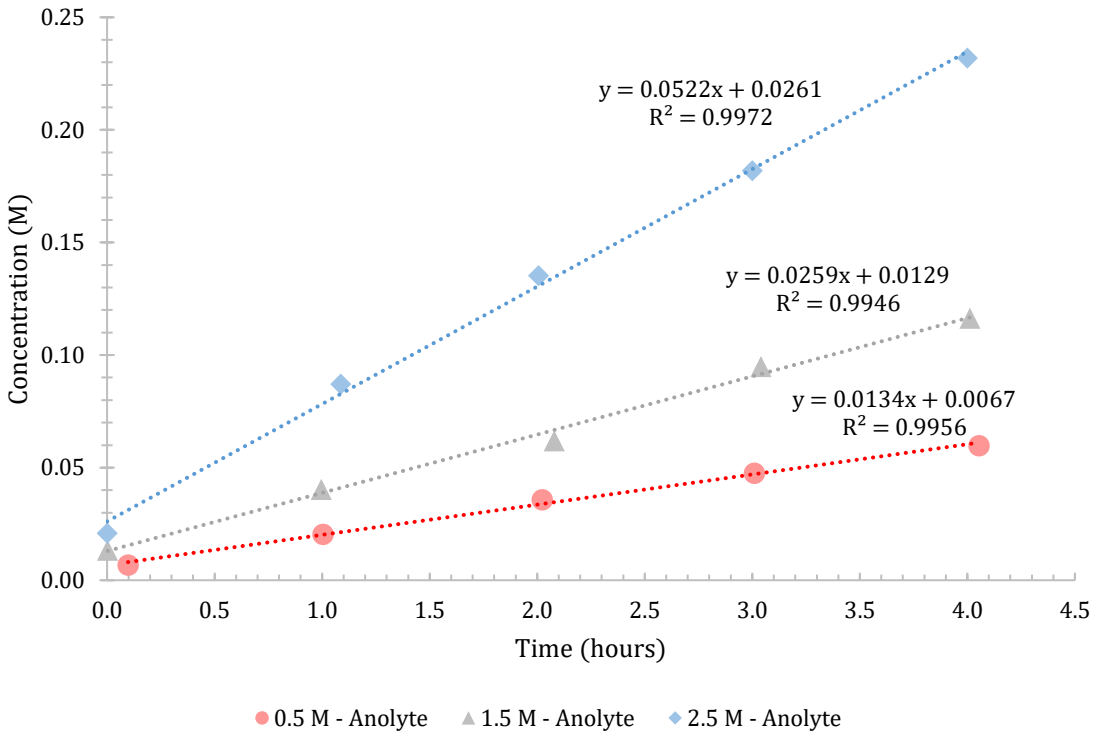

Figure 36. **Permeability tests of ethanol through ~25 µm HMT-PMBI 75% dm 25 % dz with 0.5, 1.5, & 2.5 M ethanol concentration gradients. The three data sets in rose, grey, and light blue, represent the concentration of ethanol in the anolyte of the experiments with corresponding colors. No electric current was used. A supporting electrolyte of 0.5 M $KHCO_3$ was used and continuous bubbling of CO_2 in the catholyte.**

The measured $J_{EtOH\text{-}An}$ for all three tests shown above present excellent linearity. In agreement with the $J_{EtOH\text{-}Cat}$, the values for $J_{EtOH\text{-}An}$ doubled as ΔC_i increased. The values for J_{EtOH} fall in-between those for HMT-PMBI 75% dm and HMT-PMBI 89% dm, suggesting that (based on $J_{EtOH\text{-}An}$) HMT-PMBI 75% dm 25% dz presents as a middle-ground. The change in diffusion coefficients was plotted and is shown below in **Figure 37**.

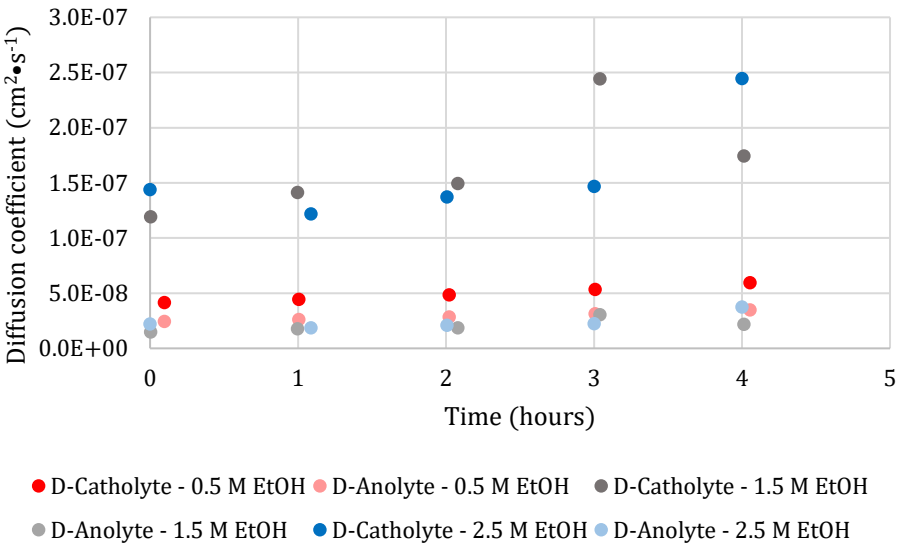

Figure 37. Diffusion coefficients of ethanol through HMT-PMBI 75% dm 25% dz as a function of time. Diffusion coefficients are calculated using either the flux using the anolyte or catholyte concentration, and are shown as either a faded or darker color, depending on whether they are caluclated using flux calculated from the anolyte or catholyte, respectively.

The calculated $D_{EtOH\text{-}Cat}$ are based on using $J_{EtOH\text{-}Cat}$, and likewise have poor linearity, however, of the data points that seem to fall on a linear curve, this trend seems more characteristic of HMT-PMBI 75% dm, and not of a parabolic shape like HMT-PMBI 89% dm. $D_{EtOH\text{-}Cat}$ for the experiment using $\Delta C_{i=0.5}$ is less than half that of $D_{EtOH\text{-}Cat}$ for the experiments using $\Delta C_{i=1.5}$ and $\Delta C_{i=2.5}$. $D_{EtOH\text{-}An}$ for all three tests are quite similar, with no clear trend. The value of the diffusion coefficients for HMT-PMBI 75% dm 25% dz are quite high compared to HMT-PMBI 75% dm. The diffusion coefficients for HMT-PMBI 75% dm range from $1.0\text{x}10^{-8}$ $cm^2 \bullet s^{-1}$ to $4.5\text{x}10^{-9}$ $cm^2 \bullet s^{-1}$, whereas the bulk of diffusion coefficients for HMT-PMBI 75% dm 25% dz range from $1.5\text{x}10^{-8}$ $cm^2 \bullet s^{-1}$ to $1.7\text{x}10^{-7}$ $cm^2 \bullet s^{-1}$. This range is close to the range of diffusion coefficients for HMT-PMBI 89% dm, from $2.4\text{x}10^{-8}$ $cm^2 \bullet s^{-1}$ to $1.1\text{x}10^{-7}$ $cm^2 \bullet s^{-1}$. It can be concluded that despite promising results in the solvent uptake and swelling measurements, and in the apparent flux in permeability experiments, HMT-PMBI 75% dm 25% is less effective at abating ethanol crossover than HMT-PMBI 75% dm, and slightly better than HMT-PMBI 89% dm.

With the same motivation of abating ethanol crossover, HMT-PMBI 75% dm 5% dx was also evaluated using permeability tests. The crosslinked membrane performed adequately compared to the pristine HMT-PMBI 75% dm membrane during *ex situ* tests and tensile tests.

Most notably, HMT-PMBI 75% dm 5% dx had significantly decreased through-plane swelling in 1.5 M ethanol and presented a minimum diffusion coefficient in 1.5 M ethanol during the DOSY experiments. The results from the permeability tests completed with HMT-PMBI 75% dm 5% dx are shown below in **Figure 38**, **Figure 39**, and **Figure 40**.

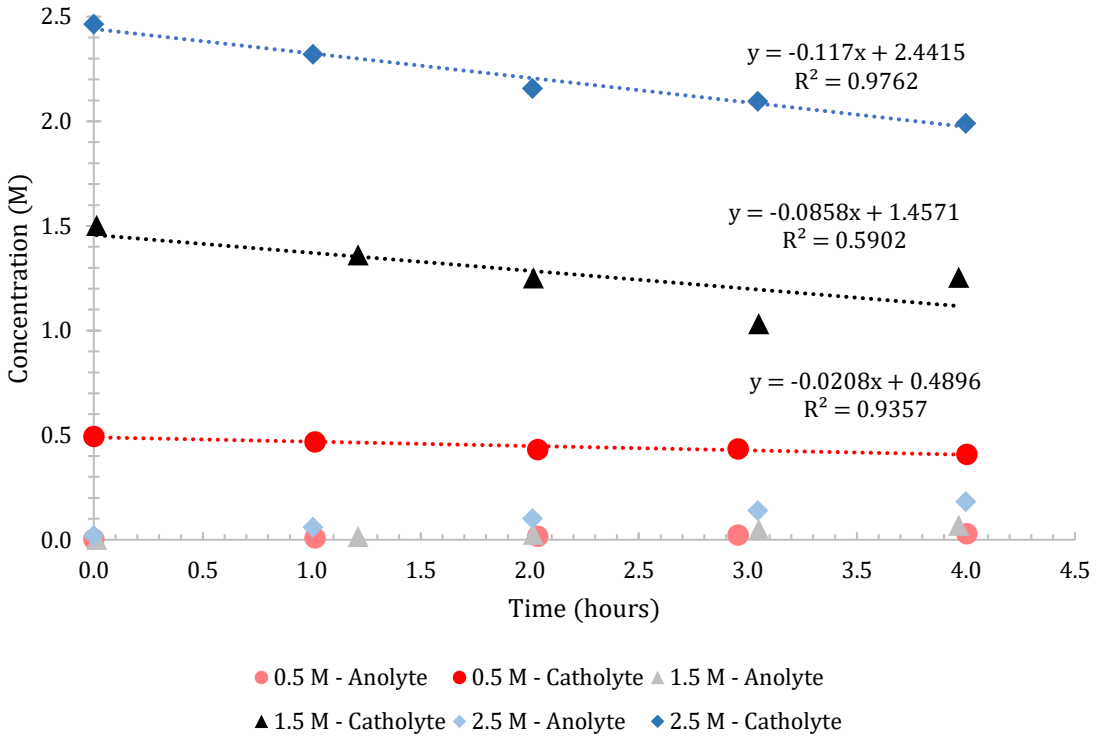

Figure 38. **Permeability tests of ethanol through ~25 µm HMT-PMBI 75% dm 5 % dx with 0.5, 1.5, & 2.5 M ethanol concentration gradients. The top three data sets in red, black, and blue, represent the concentration of ethanol in the catholyte. The bottom three data sets in rose, grey, and light blue, represent the concentration of ethanol in the anolyte of the experiments with corresponding colors. No electric current was used. A supporting electrolyte of 0.5 M $KHCO_3$ was used and continuous bubbling of CO_2 in the catholyte.**

Besides the test which had $\Delta C_{i=1.5}$, $J_{EtOH\text{-}Cat}$ trendlines show good linearity. The $J_{EtOH\text{-}Cat}$ values for HMT-PMBI 75% dm 5% dx are similar to those of HMT-PMBI 75% dm 25% dz. In agreement with the established trend, the linearity of the $J_{EtOH\text{-}An}$ values is much greater than for the $J_{EtOH\text{-}Cat.}$

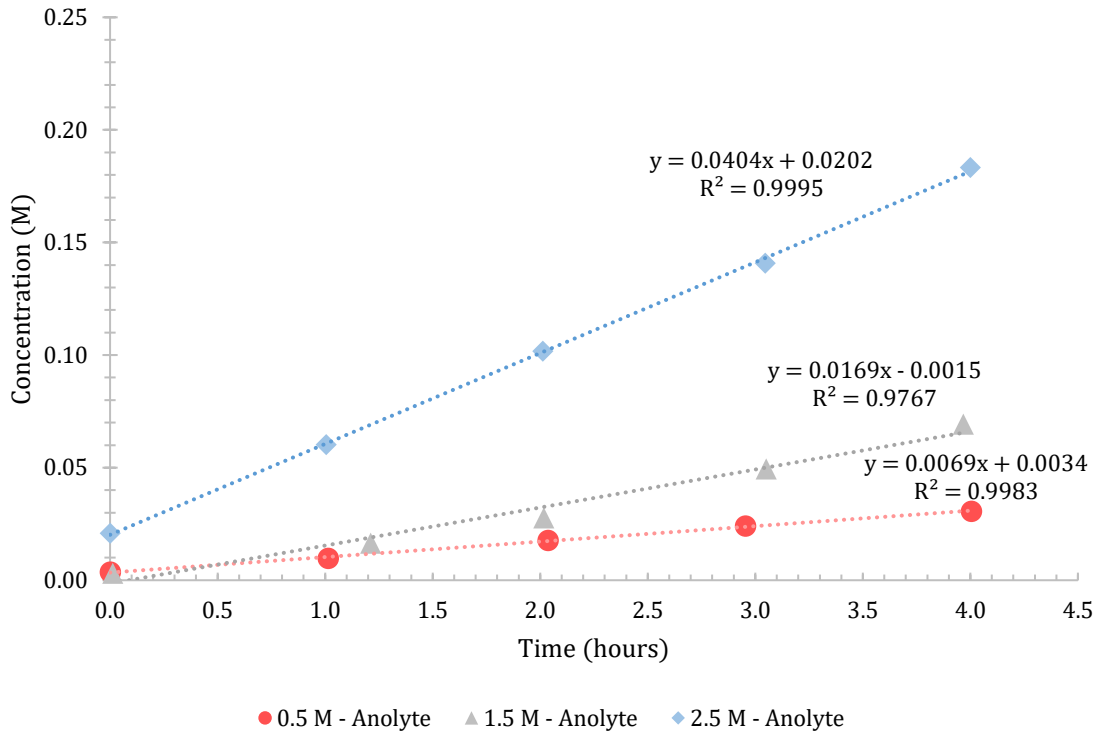

Figure 39. **Permeability tests of ethanol through ~25 µm HMT-PMBI 75% dm 5% dx with 0.5, 1.5, & 2.5 M ethanol concentration gradients. The three data sets in rose, grey, and light blue, represent the concentration of ethanol in the anolyte of the experiments with corresponding colors. No electric current was used. A supporting electrolyte of 0.5 M $KHCO_3$ was used and continuous bubbling of CO_2 in the catholyte.**

The $J_{EtOH\text{-}An}$ for HMT-PMBI 75% dm 5% dx presents as quite susceptible to increasing ΔC_i, nearly tripling between the three tests. Despite the decreased swelling observed in the earlier tests, a decrease in ethanol transport was not realized, compared to HMT-PMBI 75% dm. This implies that ethanol crossover is not solely due to swelling. Since the IEC_{Cl^-} measurements were not done in ethanol solutions, it is unknown if the number of soluble counterions increases upon exposure to ethanol. This increased number of soluble counterions could increase the membrane's affinity for ethanol, counteracting the benefits of crosslinking.

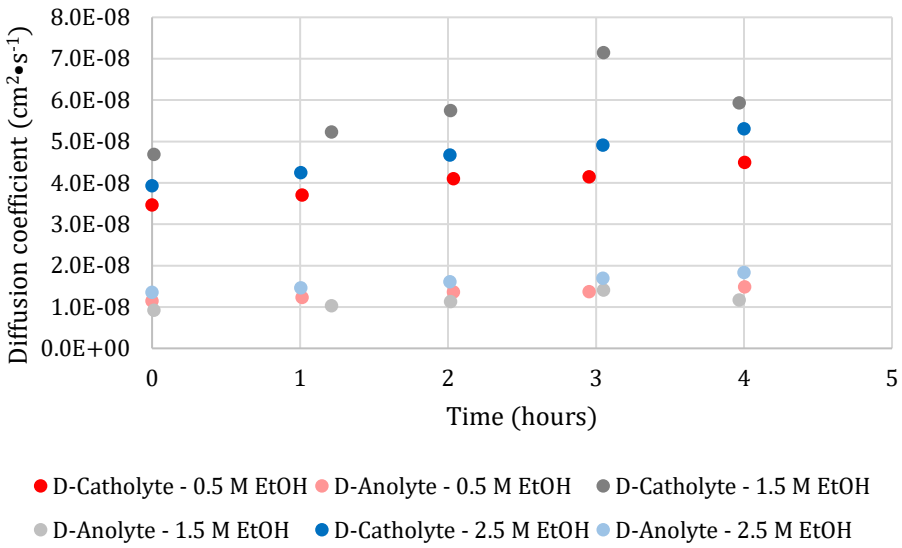

Figure 40. Diffusion coefficients of ethanol through HMT-PMBI 75% dm 5% dx as a function of time. Diffusion coefficients are calculated using either the flux using the anolyte or catholyte concentration, and are shown as either a faded or darker color, depending on whether they are caluclated using flux calculated from the anolyte or catholyte, respectively.

Overall, HMT-PMBI 75% dm 5% dx performed comparable to HMT-PMBI 75% dm 25% dz and presented no significant benefit over HMT-PMBI 75% dm, specifically in the permeability tests.

All three membranes with a dm of 75% have had a maximum diffusion coefficient for 1.5 M. This is opposite to the findings of the DOSY experiments, which showed a minimum diffusion coefficient at 1.5 M ethanol for several membranes. A discrepancy between the DOSY measurements and the permeability was expected, specifically an increase in diffusion coefficient for the permeability measurements due to the concentration gradient introduced. This is not observed, D_{EtOH} for the DOSY experiments are from 1 to 2 orders of magnitude higher than that calculated with the permeability test. Other than the concentration gradient, the other most major difference would be that the permeability tests were performed in ethanol and $KHCO_3$ solutions, rather than just ethanol solutions for the DOSY tests. Solution uptake is highly dependent on dissolved salts and their concentration. DOSY measurements were unable to be performed on membranes soaked in ethanol and $KHCO_3$ solutions due to the precipitation of salt over the course of the experiment.

3.3.2. Diffusion Driven by Concentration Gradients and Electric Field Gradients

To evaluate the effect of applying an electric field to the membrane during the permeability measurements, platinum electrodes were introduced to the H-cell apparatus, as shown in **Figure 41**.These were used to apply current via a direct current power supply. Two current densities were used, 12.5 mA/cm^2 and 25 mA/cm^2.

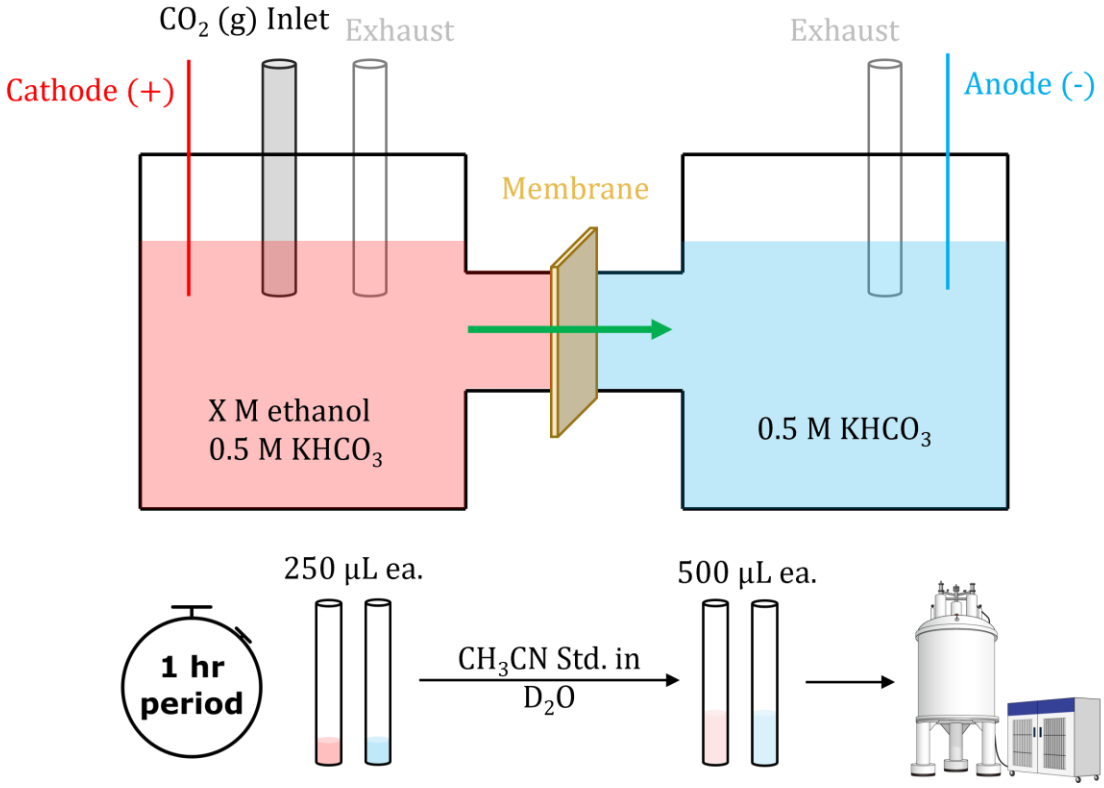

Figure 41. Identical to the previous H-cell set up, except for the addition of a platinum wire as cathode and anode, the diagram above describes the workflow for the permeability tests presented in this chapter.

HMT-PMBI 75% dm was chosen to conduct tests with a concentration and electric field gradient, as it performed best among the membranes during *in situ* tests. An initial concentration gradient of 2.5 M ethanol was chosen to exacerbate any increased diffusion due to the applied field. The results for both current densities are shown in **Figure 42**, as well as the data set for the test with HMT-PMBI 75% dm from the previous section with $\Delta C_{i=2.5}$. This addition the case with no current applied allows facile comparison of how the diffusion coefficients change due to an addition of an electric field. The electric field across the membrane was measured using Ag/AgCl

double junction reference electrodes pressed directly up to the membrane, pointed tip to tip. The voltage measured is presented in **Figure 44**.

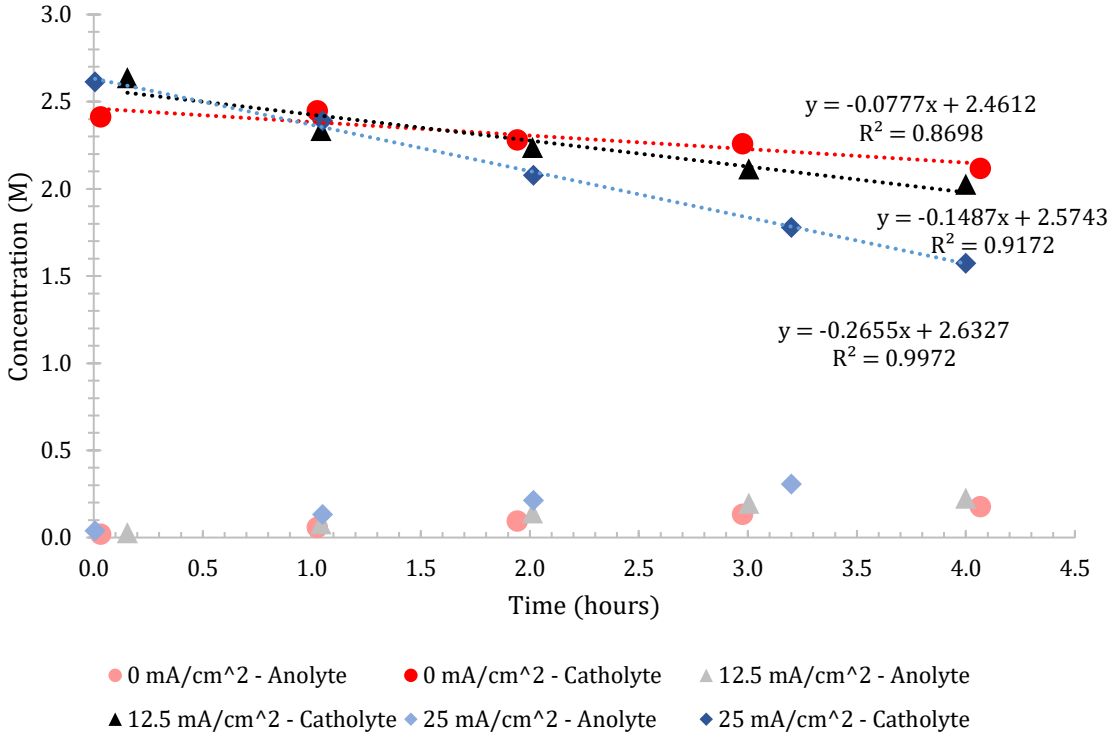

Figure 42. **Permeability tests of ethanol through ~25 µm HMT-PMBI 75% dm with a 2.5 M ethanol concentration gradients. The top three data sets in red, black, and blue, represent the concentration of ethanol in the catholyte. The bottom three data sets in rose, grey, and light blue, represent the concentration of ethanol in the anolyte of the experiments with corresponding colors. An electric current of 0, 12.5 and 2.5 mA/cm^2 was used. A supporting electrolyte of 0.5 M $KHCO_3$ was used and continuous bubbling of CO_2 in the catholyte.**

A rapid increase in $J_{EtOH\text{-}Cat}$ is observed as current density, and therefore electric field, increases. Added electric field doubles the flux at a current density of 12.5 mA/cm^2 and triples the flux at 25 mA/cm^2. This is observed in the $J_{EtOH\text{-}cat}$, and not the $J_{EtOH\text{-}An}$, as shown in **Figure 43**. With this specific set up, concentration gradient, electric field, the electroosmotic component of the total flux is highly dependent on an electric field. While this was an expected finding, it was not expected to have as much or more of an effect on the transport of a neutral molecule, such as ethanol.

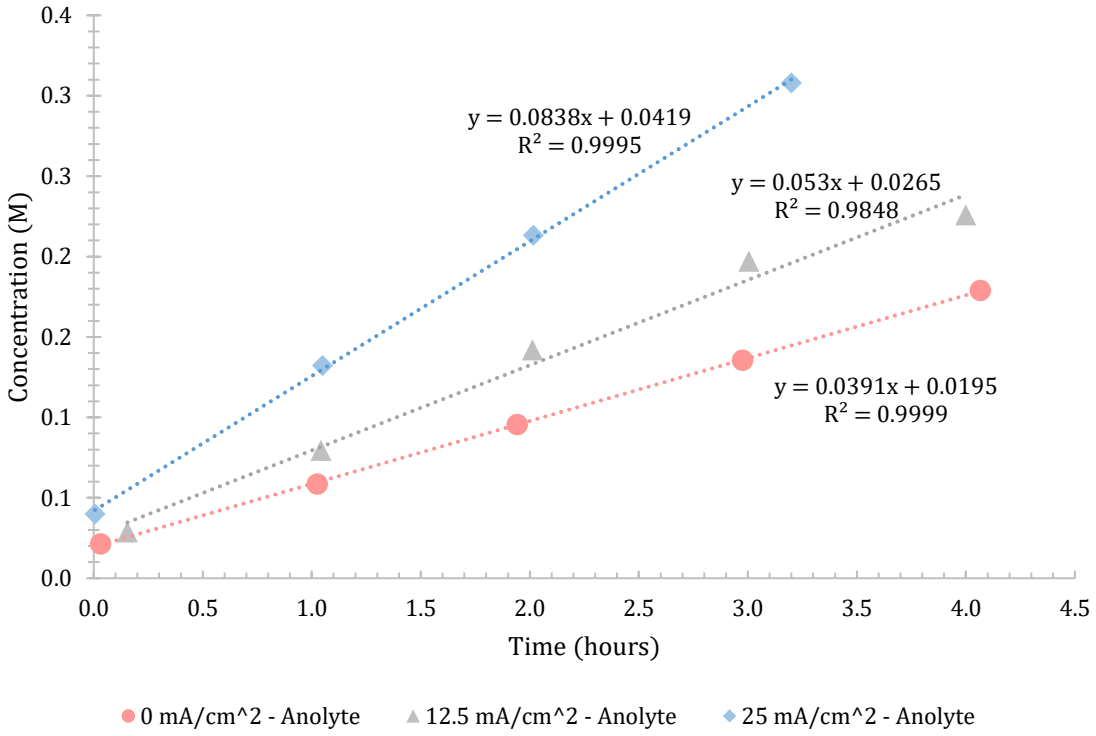

Figure 43. **Permeability tests of ethanol through ~25 µm HMT-PMBI 75% dm with a 2.5 M ethanol concentration gradients. The three data sets in rose, grey, and light blue, represent the concentration of ethanol in the anolyte of the experiments with corresponding colors. An electric current of 0, 12.5 and 2.5 mA/cm^2 was used. A supporting electrolyte of 0.5 M $KHCO_3$ was used and continuous bubbling of CO_2 in the catholyte.**

The flux of ethanol into the anolyte is not nearly as intense when increasing electric field. This suggests that the applied electric field is able to force ethanol into the membrane more easily than it can pull ethanol from the membrane. The affinity for ethanol to remain in the membrane is so high that the same forces which rapidly push ethanol into the membrane are unable to pull it out of the membrane.

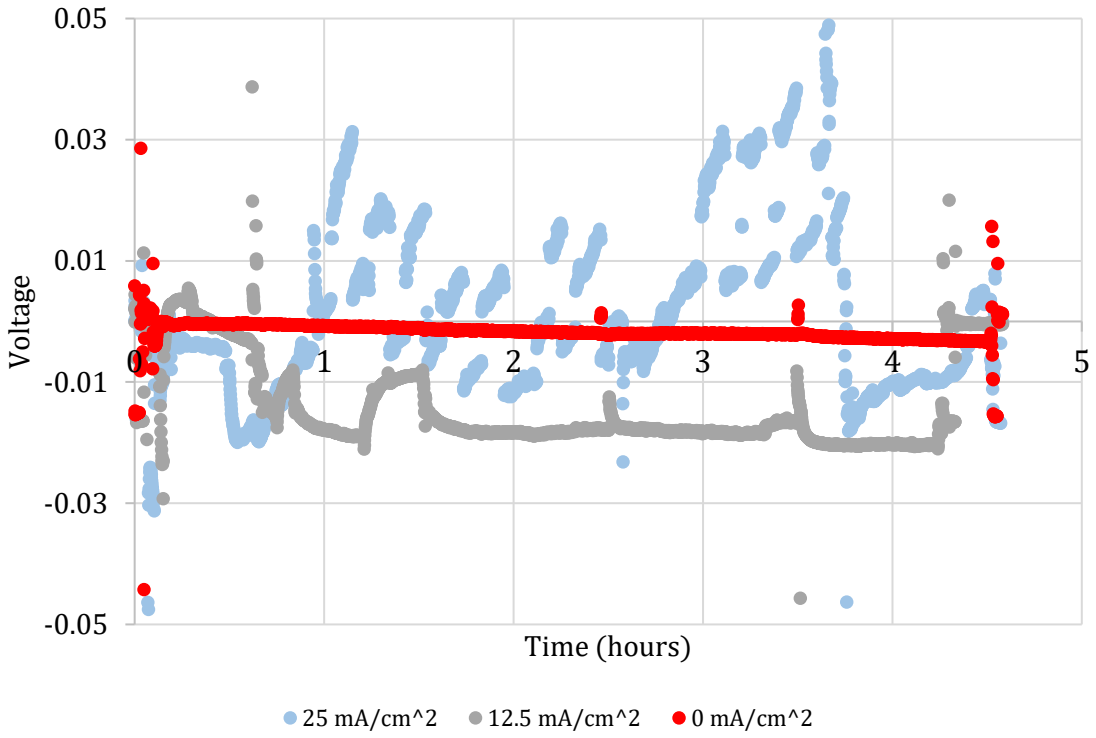

Figure 44. **The data for the test with 25 mA/cm^2 is anomolous and the voltage measured was extremely erratic. The voltage across them membrane in the other tests were constant and can be observed to vary when samples were taken from the H-cell.**

It can be observed (in **Figure 44**) that the voltage for the cell which ran 12.5 mA/cm^2, at a voltage of about 20 mV. The data for the test with an applied current of 25 mA/cm^2 is too poor to tell what voltage was established across the membrane. This erratic data could be due to bubbling of H_2 or O_2 production by either platinum electrode too close to the reference electrode.

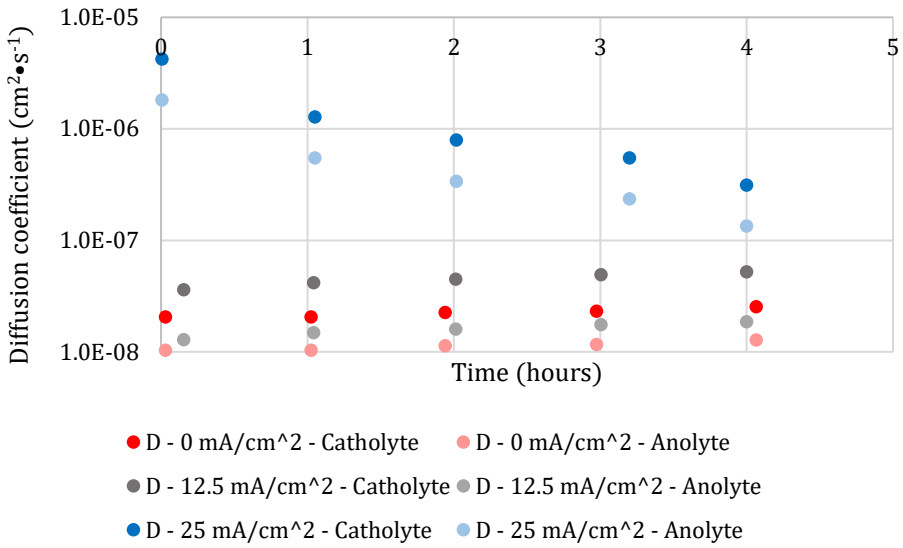

Figure 45. The diffusion coefficients of ethanol through HMT-PMBI 75% dm with an initial concentration gradient of 2.5 M ethanol. A current density of 0, 12.5, and 25 mA/cm^2 was used. The diffusion coefficients scale with applied current density. The y-axis is a logarithmic plot to better visualize the data.

Different from all other tests, a decrease in diffusion coefficients is observed for the test with an applied current density of 25 mA/cm^2, as observed in **Figure 45**. This is puzzling, as it was expected that the diffusion coefficient would increase with an applied electric field, rather than decrease. Due to the reliance on Fick's first law, it is difficult to describe the diffusion coefficient of a non-steady state system such as this. An interesting observation is that the diffusion coefficients for the test with 12.5 mA/cm^2 are stable or slightly increasing, similar to the previous tests with no applied current. Conclusions regarding the addition of the electric field can only be made for its contribution to the movement of ethanol into and through the membrane. Electric field gradients are proven to exacerbate the rate of ethanol uptake of HMT-PMBI 75% dm but not as intensely the rate of ethanol flux into the anolyte.

Chapter 4. Conclusions

The motivation of this project was to begin quantifying and documenting the transport and interactions of ethanol in AEM based CO_2 electrolysers. A combination of membrane characterization methods, diffusion NMR spectroscopy and *in situ* permeability measurements found that ethanol transport is highly dependent on the membrane chemistry, with a complex relationship with solution uptake, swelling, and IEC. Initial permeability measurements discovered non-steady state diffusion processes, whose intensity of deviation from steady state was highly dependent on membrane chemistry. HMT-PMBI 89% dm was found to be the least optimal membrane to abate ethanol diffusion in electrolyser-like conditions. Having the highest diffusion coefficients, large deviation from steady state conditions, and drastic SU and swelling indicate that HMT-PMBI is a suboptimal choice compared to HMT-PMBI 75% dm in all evaluated metrics.

Tensile strength was also used as a probe into the structural changes that occurred in each membrane when exposed to increasing ethanol concentrations. The crosslinked HMT-PMBI 75% dm 5% dx had an increase in elongation before break upon exposure to ethanol, proving as more robust than the uncrosslinked form. Overall, HMT-PMBI 75% presented a good balance between strength, elongation and was not significantly affected by ethanol exposure.

DOSY measurements were conducted for each membrane and showed significantly higher diffusion coefficients than the H-cell permeability tests. This is contradictory to what was expected. Brownian motion (self-diffusion) was expected to be significantly slower than diffusion due to a concentration or electric field gradient. This could indicate that this method is inaccurate and must be refined before being used further.

Two modifications of HMT-PMBI 75% dm were performed as based on literature syntheses. The intention was to evaluate potential decreases in diffusion of ethanol using conventional and ionic crosslinking. Literature showed drastic decreases in WU and swelling, which were hypothesized to translate to decreases in ethanol diffusion, solution uptake, and swelling when submitted to electrolyser-like conditions. HMT-PMBI 75% dm 5% dx was observed to be insoluble in a range of ethanol solutions, up to 95% ethanol. This insolubility was anticipated to yield better performance but was surprisingly not realized. HMT-PMBI 75% dm 5% dx performed similarly to HMT-PMBI 75% dm but had higher changes in diffusion coefficients during the permeability tests. The crosslinked material outperformed pristine HMT-

PMBI 75% in three metrics, SU, TPS, and tensile strength before and after ethanol soaks. Contrary to the conventionally crosslinked material, HMT-PMBI 75% dm 25% dz showed good performance. The ionically crosslinked membrane had ethanol diffusion coefficients higher, but similar to HMT-PMBI 75% dm. It also was the only membrane to show negative IPS. This has important implications when considering adopting these membranes in MEA-style electrolysers, where membrane swelling can negatively impact the cell.

Future studies may require further exploration of mathematical solutions to non-steady state diffusion, as the change in diffusion coefficients over time is an issue that makes comparing membranes a complicated task. These increases in diffusion rate may translate into large inefficiencies in fully built electrolysers. While a method of degradation or membrane deterioration was not identified, the effect of ethanol on the hydrocarbon AEMs studies presents a challenge for synthetic chemists. The phenomenon of ethanol uptake and transport seems to be strongly connected to the number of exchangeable and unexchangeable charge groups. It is suggested that IEC measurements be performed in ethanol solutions to evaluate whether the swelling and solvation of the polymer by ethanol releases ions that were previously inaccessible. If this is the case, this would challenge new membranes to compromise conductivity to reduce ethanol uptake and transport. The methods of crosslinking used to modify HMT-PMBI 75% dm in this work both involve increasing the IEC of the polymer, while both attempting to decrease uptake and swelling. It is suggested that a novel technique be employed to crosslink HMT-PMBI 75% dm without increasing its IEC. Functionalization of the hexamethyl – p terphenyl group rather than the available nitrogen atoms could yield a potential starting point.

The field of CO_2 electrolysis is growing at an increasing pace and optimisation of energetic efficiency and maximum operating current density have been identified as the main metrics to measure its potential to be adopted commercially. If electrolysers must be efficient and have high current density, however inefficiencies that scale with current density, such as ethanol product crossover must be understood and addressed while the field is still in these early stages.

References

(1) Arto, I.; Dietzenbacher, E. Drivers of the Growth in Global Greenhouse Gas Emissions. *Environ Sci Technol* **2014**, *48* (10), 5388–5394. https://doi.org/10.1021/es5005347.

(2) Ritchie, H.; Roser, M. *CO_2 Emissions How Much CO_2 Does the World Emit? Which Countries Emit the Most?* https://ourworldindata.org/co2-emissions#article-citation, accessed March 15, 2024.

(3) Lashof, D. A.; Ahujah, D. R. *Relative Contributions of Greenhouse Gas Emissions to Global Warming*.

(4) Lamb, W. F.; Wiedmann, T.; Pongratz, J.; Andrew, R.; Crippa, M.; Olivier, J. G. J.; Wiedenhofer, D.; Mattioli, G.; Khourdajie, A. Al; House, J.; Pachauri, S.; Figueroa, M.; Saheb, Y.; Slade, R.; Hubacek, K.; Sun, L.; Ribeiro, S. K.; Khennas, S.; De La Rue Du Can, S.; Chapungu, L.; Davis, S. J.; Bashmakov, I.; Dai, H.; Dhakal, S.; Tan, X.; Geng, Y.; Gu, B.; Minx, J. A Review of Trends and Drivers of Greenhouse Gas Emissions by Sector from 1990 to 2018. *Environmental Research Letters*. IOP Publishing Ltd July 1, 2021. https://doi.org/10.1088/1748-9326/abee4e.

(5) Battin, T. J.; Luyssaert, S.; Kaplan, L. A.; Aufdenkampe, A. K.; Richter, A.; Tranvik, L. J. The Boundless Carbon Cycle. *Nature Geoscience*. September 2009, pp 598–600. https://doi.org/10.1038/ngeo618.

(6) Tomkins, P.; Müller, T. E. Evaluating the Carbon Inventory, Carbon Fluxes and Carbon Cycles for a Long-Term Sustainable World. *Green Chemistry*. Royal Society of Chemistry 2019, pp 3994–4013. https://doi.org/10.1039/c9gc00528e.

(7) Falkowski, P.; Scholes, † R J; Boyle, E.; Canadell, ‡ J; Canfield, ‡ D; Elser, ‡ J; Gruber, ‡ N; Hibbard, ‡ K; Högberg, ‡ P; Linder, ‡ S; Mackenzie, ‡ F T; Iii, ‡ B Moore; Pedersen, ‡ T; Rosenthal, ‡ Y; Seitzinger, ‡ S; Smetacek, ‡ V; Steffen, ‡ W. *The Global Carbon Cycle: A Test of Our Knowledge of Earth as a System*; 2000. https://www.science.org.

(8) Dion, J.; Kanduth, A.; Moorhouse, J.; Beugin, D. Canadas-Net-Zero-Future_FINAL-2. **2021**.

(9) International Renewable Energy Agency. *RENEWABLE POWER GENERATION COSTS IN 2022*; 2023.

(10) Energy Information Administration, U. *Monthly Energy Review – February 2024*; 2024. www.eia.gov/mer.

(11) Yukon Energy. *NEWS RELEASE - Grid Scale Battery*; 2022. https://yukonenergy.ca/energy-in-yukon/projects-facilities/battery-storage (accessed 2024-03-17).

(12) Nel ASA. *Nel Plans Gigafactory in Michigan Nel Hydrogen*; 2023. https://nelhydrogen.com/articles/in-depth/nel-plans-gigafactory-in-michigan/ (accessed 2024-03-17).

(13) Metz, B.; Davidson, O.; de Coninck, H.; Loos, M.; Meyer, L. *CARBON DIOXIDE CAPTURE AND STORAGE*; Cambridge, UK, 2005.

(14) Hepburn, C.; Adlen, E.; Beddington, J.; Carter, E. A.; Fuss, S.; Mac Dowell, N.; Minx, J. C.; Smith, P.; Williams, C. K. The Technological and Economic Prospects for CO2 Utilization and Removal. *Nature*. Nature Publishing Group November 7, 2019, pp 87–97. https://doi.org/10.1038/s41586-019-1681-6.

(15) Bushuyev, O. S.; De Luna, P.; Dinh, C. T.; Tao, L.; Saur, G.; van de Lagemaat, J.; Kelley, S. O.; Sargent, E. H. What Should We Make with CO2 and How Can We Make It? *Joule*. Cell Press May 16, 2018, pp 825–832. https://doi.org/10.1016/j.joule.2017.09.003.

(16) De Luna, P.; Hahn, C.; Higgins, D.; Jaffer, S. A.; Jaramillo, T. F.; Sargent, E. H. What Would It Take for Renewably Powered Electrosynthesis to Displace Petrochemical Processes? *Science*. American Association for the Advancement of Science 2019. https://doi.org/10.1126/science.aav3506.

(17) Orella, M. J.; Román-Leshkov, Y.; Brushett, F. R. Emerging Opportunities for Electrochemical Processing to Enable Sustainable Chemical Manufacturing. *Current Opinion in Chemical Engineering*. Elsevier Ltd June 1, 2018, pp 159–167. https://doi.org/10.1016/j.coche.2018.05.002.

(18) Liang, S.; Altaf, N.; Huang, L.; Gao, Y.; Wang, Q. Electrolytic Cell Design for Electrochemical CO2 Reduction. *Journal of CO2 Utilization*. Elsevier Ltd January 1, 2020, pp 90–105. https://doi.org/10.1016/j.jcou.2019.09.007.

(19) He, R.; Xu, N.; Hasan, I. M. ul; Peng, L.; Li, L.; Huang, H.; Qiao, J. Advances in Electrolyzer Design and Development for Electrochemical CO2 Reduction. *EcoMat*. John Wiley and Sons Inc July 1, 2023. https://doi.org/10.1002/eom2.12346.

(20) Gabardo, C. M.; O'Brien, C. P.; Edwards, J. P.; McCallum, C.; Xu, Y.; Dinh, C. T.; Li, J.; Sargent, E. H.; Sinton, D. Continuous Carbon Dioxide Electroreduction to Concentrated Multi-Carbon Products Using a Membrane Electrode Assembly. *Joule* **2019**, *3* (11), 2777–2791. https://doi.org/10.1016/j.joule.2019.07.021.

(21) Samu, A. A.; Szenti, I.; Kukovecz, Á.; Endrődi, B.; Janáky, C. Systematic Screening of Gas Diffusion Layers for High Performance CO2 Electrolysis. *Commun Chem* **2023**, *6* (1). https://doi.org/10.1038/s42004-023-00836-2.

(22) Yang, K.; Kas, R.; Smith, W. A.; Burdyny, T. Role of the Carbon-Based Gas Diffusion Layer on Flooding in a Gas Diffusion Electrode Cell for Electrochemical CO2Reduction. *ACS Energy Lett* **2021**, *6* (1), 33–40. https://doi.org/10.1021/acsenergylett.0c02184.

(23) Pelayo García de Arquer, F.; Dinh, C.-T.; Ozden, A.; Wicks, J.; McCallum, C.; Kirmani, A. R.; Nam, D.-H.; Gabardo, C.; Seifitokaldani, A.; Wang, X.; Li, Y. C.; Li, F.; Edwards, J.; Richter, L. J.; Thorpe, S. J.; Sinton, D.; Sargent, E. H. *CO 2 Electrolysis to Multicarbon Products at Activities Greater than 1 A Cm −2*. http://science.sciencemag.org/.

(24) Xing, Z.; Hu, L.; Ripatti, D. S.; Hu, X.; Feng, X. Enhancing Carbon Dioxide Gas-Diffusion Electrolysis by Creating a Hydrophobic Catalyst Microenvironment. *Nat Commun* **2021**, *12* (1). https://doi.org/10.1038/s41467-020-20397-5.

(25) Masel, R. I.; Liu, Z.; Yang, H.; Kaczur, J. J.; Carrillo, D.; Ren, S.; Salvatore, D.; Berlinguette, C. P. An Industrial Perspective on Catalysts for Low-Temperature CO2 Electrolysis. *Nature Nanotechnology*. Nature Research February 1, 2021, pp 118–128. https://doi.org/10.1038/s41565-020-00823-x.

(26) Qiao, J.; Liu, Y.; Hong, F.; Zhang, J. A Review of Catalysts for the Electroreduction of Carbon Dioxide to Produce Low-Carbon Fuels. *Chemical Society Reviews*. Royal Society of Chemistry January 21, 2014, pp 631–675. https://doi.org/10.1039/c3cs60323g.

(27) Chen, Y.; Wrubel, J. A.; Vise, A. E.; Intia, F.; Harshberger, S.; Klein, E.; Smith, W. A.; Ma, Z.; Deutsch, T. G.; Neyerlin, K. C. The Effect of Catholyte and Catalyst Layer Binders on CO2 Electroreduction Selectivity. *Chem Catalysis* **2022**, *2* (2), 400–421. https://doi.org/10.1016/j.checat.2022.01.011.

(28) Pham, T. H. M.; Zhang, J.; Li, M.; Shen, T. H.; Ko, Y.; Tileli, V.; Luo, W.; Züttel, A. Enhanced Electrocatalytic CO2 Reduction to C2+ Products by Adjusting the Local Reaction Environment with Polymer Binders. *Adv Energy Mater* **2022**, *12* (9). https://doi.org/10.1002/aenm.202103663.

(29) Lee, J. H.; Kattel, S.; Xie, Z.; Tackett, B. M.; Wang, J.; Liu, C. J.; Chen, J. G. Understanding the Role of Functional Groups in Polymeric Binder for Electrochemical Carbon Dioxide Reduction on Gold Nanoparticles. *Adv Funct Mater* **2018**, *28* (45). https://doi.org/10.1002/adfm.201804762.

(30) Hori, Y.; Konishi, H.; Futamura, T.; Murata, A.; Koga, O.; Sakurai, H.; Oguma, K. "deactivation of Copper Electrode" in Electrochemical Reduction of CO2. *Electrochim Acta* **2005**, *50* (27), 5354–5369. https://doi.org/10.1016/j.electacta.2005.03.015.

(31) He, J.; Huang, A.; Johnson, N. J. J.; Dettelbach, K. E.; Weekes, D. M.; Cao, Y.; Berlinguette, C. P. Stabilizing Copper for CO 2 Reduction in Low-Grade Electrolyte. *Inorg Chem* **2018**, *57* (23), 14624–14631. https://doi.org/10.1021/acs.inorgchem.8b02311.

(32) Mardle, P.; Cassegrain, S.; Habibzadeh, F.; Shi, Z.; Holdcroft, S. *Carbonate Ion Crossover in Zero-Gap, KOH-Anolyte CO 2 Electrolysis*.

(33) Rabinowitz, J. A.; Kanan, M. W. The Future of Low-Temperature Carbon Dioxide Electrolysis Depends on Solving One Basic Problem. *Nature Communications*. Nature Research December 1, 2020. https://doi.org/10.1038/s41467-020-19135-8.

(34) Lee, J.; Lim, J.; Roh, C. W.; Whang, H. S.; Lee, H. Electrochemical CO2 Reduction Using Alkaline Membrane Electrode Assembly on Various Metal Electrodes. *Journal of CO2 Utilization* **2019**, *31*, 244–250. https://doi.org/10.1016/j.jcou.2019.03.022.

(35) Durst, J.; Siebel, A.; Simon, C.; Hasché, F.; Herranz, J.; Gasteiger, H. A. New Insights into the Electrochemical Hydrogen Oxidation and Evolution Reaction Mechanism. *Energy Environ Sci* **2014**, *7* (7), 2255–2260. https://doi.org/10.1039/c4ee00440j.

(36) Cheng, T.; Wang, L.; Merinov, B. V.; Goddard, W. A. Explanation of Dramatic PH-Dependence of Hydrogen Binding on Noble Metal Electrode: Greatly Weakened Water Adsorption at High PH. *J Am Chem Soc* **2018**, *140* (25), 7787–7790. https://doi.org/10.1021/jacs.8b04006.

(37) Wright, A. G.; Fan, J.; Britton, B.; Weissbach, T.; Lee, H. F.; Kitching, E. A.; Peckham, T. J.; Holdcroft, S. Hexamethyl-: P -Terphenyl Poly(Benzimidazolium): A Universal Hydroxide-Conducting Polymer for Energy Conversion Devices. *Energy Environ Sci* **2016**, *9* (6), 2130–2142. https://doi.org/10.1039/c6ee00656f.

(38) Thomas, O. D.; Peckham, T. J.; Thanganathan, U.; Yang, Y.; Holdcroft, S. Sulfonated Polybenzimidazoles: Proton Conduction and Acid-Base Crosslinking. *J Polym Sci A Polym Chem* **2010**, *48* (16), 3640–3650. https://doi.org/10.1002/pola.24147.

(39) Thomas, O. D.; Soo, K. J. W. Y.; Peckham, T. J.; Kulkarni, M. P.; Holdcroft, S. Anion Conducting Poly(Dialkyl Benzimidazolium) Salts. *Polym Chem* **2011**, *2* (8), 1641–1643. https://doi.org/10.1039/c1py00142f.

(40) Thomas, O. D.; Soo, K. J. W. Y.; Peckham, T. J.; Kulkarni, M. P.; Holdcroft, S. A Stable Hydroxide-Conducting Polymer. *J Am Chem Soc* **2012**, *134* (26), 10753–10756. https://doi.org/10.1021/ja303067t.

(41) Wright, A. G.; Holdcroft, S. Hydroxide-Stable Ionenes. *ACS Macro Lett* **2014**, *3* (5), 444–447. https://doi.org/10.1021/mz500168d.

(42) Lee, H. J.; Choi, J.; Han, J. Y.; Kim, H. J.; Sung, Y. E.; Kim, H.; Henkensmeier, D.; Ae Cho, E.; Jang, J. H.; Yoo, S. J. Synthesis and Characterization of Poly(Benzimidazolium) Membranes for Anion Exchange Membrane Fuel Cells. *Polymer Bulletin* **2013**, *70* (9), 2619–2631. https://doi.org/10.1007/s00289-013-0978-0.

(43) Le, X. T.; Bui, T. H.; Viel, P.; Berthelot, T.; Palacin, S. On the Structure-Properties Relationship of the AMV Anion Exchange Membrane. *J Memb Sci* **2009**, *340* (1–2), 133–140. https://doi.org/10.1016/j.memsci.2009.05.025.

(44) Schibli, E. M.; Stewart, J. C.; Wright, A. A.; Chen, B.; Holdcroft, S.; Frisken, B. J. The Nanostructure of HMT-PMBI, a Sterically Hindered Ionene. *Macromolecules* **2020**, *53* (12), 4908–4916. https://doi.org/10.1021/acs.macromol.0c00978.

(45) Biancolli, A. L. G.; Barbosa, A. S.; Kodama, Y.; de Sousa, R. R.; Lanfredi, A. J. C.; Fonseca, F. C.; Rey, J. F. Q.; Santiago, E. I. Unveiling the Influence of Radiation-Induced Grafting Methods on the Properties of Polyethylene-Based Anion-Exchange Membranes for Alkaline Fuel Cells. *J Power Sources* **2021**, *512*. https://doi.org/10.1016/j.jpowsour.2021.230484.

(46) Wheeler, D. G.; Mowbray, B. A. W.; Reyes, A.; Habibzadeh, F.; He, J.; Berlinguette, C. P. Quantification of Water Transport in a CO2electrolyzer. *Energy Environ Sci* **2020**, *13* (12), 5126–5134. https://doi.org/10.1039/d0ee02219e.

(47) Etzold, B. J. M.; Krewer, U.; Thiele, S.; Dreizler, A.; Klemm, E.; Turek, T. Understanding the Activity Transport Nexus in Water and CO2 Electrolysis: State of the Art, Challenges and Perspectives. *Chemical Engineering Journal*. Elsevier B.V. November 15, 2021. https://doi.org/10.1016/j.cej.2021.130501.

(48) Mardle, P.; Cassegrain, S.; Habibzadeh, F.; Shi, Z.; Holdcroft, S. *Carbonate Ion Crossover in Zero-Gap, KOH-Anolyte CO 2 Electrolysis*.

(49) Reyes, A.; Jansonius, R. P.; Mowbray, B. A. W.; Cao, Y.; Wheeler, D. G.; Chau, J.; Dvorak, D. J.; Berlinguette, C. P. Managing Hydration at the Cathode Enables Efficient CO2Electrolysis at Commercially Relevant Current Densities. *ACS Energy Lett* **2020**, *5* (5), 1612–1618. https://doi.org/10.1021/acsenergylett.0c00637.

(50) Peng, J.; Roy, A. L.; Greenbaum, S. G.; Zawodzinski, T. A. Effect of CO2 Absorption on Ion and Water Mobility in an Anion Exchange Membrane. *J Power Sources* **2018**, *380*, 64–75. https://doi.org/10.1016/j.jpowsour.2018.01.071.

(51) Gangrade, A. S.; Cassegrain, S.; Chandra Ghosh, P.; Holdcroft, S. Permselectivity of Ionene-Based, Aemion® Anion Exchange Membranes. *J Memb Sci* **2022**, *641*. https://doi.org/10.1016/j.memsci.2021.119917.

(52) Ma, M.; Zheng, Z.; Yan, W.; Hu, C.; Seger, B. Rigorous Evaluation of Liquid Products in High-Rate CO2/CO Electrolysis. *ACS Energy Lett* **2022**, *7* (8), 2595–2601. https://doi.org/10.1021/acsenergylett.2c01288.

(53) Khan, M. A.; Nabil, S. K.; Al-Attas, T.; Yasri, N. G.; Roy, S.; Rahman, M. M.; Larter, S.; Ajayan, P. M.; Hu, J.; Kibria, M. G. Zero-Crossover Electrochemical CO2 Reduction to Ethylene with Co-Production of Valuable Chemicals. *Chem Catalysis* **2022**, *2* (8), 2077–2095. https://doi.org/10.1016/j.checat.2022.06.018.

(54) Eriksson, B.; Asset, T.; Spanu, F.; Lecoeur, F.; Dupont, M.; Garcés-Pineda, F. A.; Galán-Mascarós, J. R.; Cavaliere, S.; Rozière, J.; Jaouen, F. Mitigation of Carbon Crossover in CO 2 Electrolysis by Use of Bipolar Membranes . *J Electrochem Soc* **2022**, *169* (3), 034508. https://doi.org/10.1149/1945-7111/ac580e.

(55) Li, Y. C.; Yan, Z.; Hitt, J.; Wycisk, R.; Pintauro, P. N.; Mallouk, T. E. Bipolar Membranes Inhibit Product Crossover in CO2 Electrolysis Cells. *Adv Sustain Syst* **2018**, *2* (4). https://doi.org/10.1002/adsu.201700187.

(56) Larrazábal, G. O.; Strøm-Hansen, P.; Heli, J. P.; Zeiter, K.; Therkildsen, K. T.; Chorkendorff, I.; Seger, B. Analysis of Mass Flows and Membrane Cross-over in CO2 Reduction at High Current Densities in an MEA-Type Electrolyzer. *ACS Appl Mater Interfaces* **2019**, *11* (44), 41281–41288. https://doi.org/10.1021/acsami.9b13081.

(57) Zhang, J.; Luo, W.; Züttel, A. Crossover of Liquid Products from Electrochemical CO2 Reduction through Gas Diffusion Electrode and Anion Exchange Membrane. *J Catal* **2020**, *385*, 140–145. https://doi.org/10.1016/j.jcat.2020.03.013.

(58) McCallum, C.; Gabardo, C. M.; O'Brien, C. P.; Edwards, J. P.; Wicks, J.; Xu, Y.; Sargent, E. H.; Sinton, D. Reducing the Crossover of Carbonate and Liquid Products during Carbon Dioxide Electroreduction. *Cell Rep Phys Sci* **2021**, *2* (8). https://doi.org/10.1016/j.xcrp.2021.100522.

(59) Wang, N.; Miao, R. K.; Lee, G.; Vomiero, A.; Sinton, D.; Ip, A. H.; Liang, H.; Sargent, E. H. Suppressing the Liquid Product Crossover in Electrochemical CO 2 Reduction . *SmartMat* **2021**, *2* (1), 12–16. https://doi.org/10.1002/smm2.1018.

(60) Weissbach, T.; Wright, A. G.; Peckham, T. J.; Sadeghi Alavijeh, A.; Pan, V.; Kjeang, E.; Holdcroft, S. Simultaneous, Synergistic Control of Ion Exchange Capacity and Cross-Linking of Sterically-Protected Poly(Benzimidazolium)s. *Chemistry of Materials* **2016**, *28* (21), 8060–8070. https://doi.org/10.1021/acs.chemmater.6b03902.

(61) Cassegrain, S.; Saatkamp, T.; Mardle, P.; Gangrade, A.; Hui, J.; Holdcroft, S. Zwitterionic Ionenes toward Processable, Low Water-Containing Anion Exchange Membranes: Synthesis, Characterization, and Application in Electrochemical CO2 Reduction. *Chemistry of Materials* **2024**, *36* (1), 197–210. https://doi.org/10.1021/acs.chemmater.3c01919.

(62) Wang, J.; Wang, J.; Zhang, S. Synthesis and Characterization of Cross-Linked Poly(Arylene Ether Ketone) Containing Pendant Quaternary Ammonium Groups for Anion-Exchange Membranes. *J Memb Sci* **2012**, *415–416*, 205–212. https://doi.org/10.1016/j.memsci.2012.04.054.

(63) Wang, L.; Hickner, M. A. Low-Temperature Crosslinking of Anion Exchange Membranes. *Polym Chem* **2014**, *5* (8), 2928–2935. https://doi.org/10.1039/c3py01490h.

(64) Zhou, J.; Ünlü, M.; Anestis-Richard, I.; Kohl, P. A. Crosslinked, Epoxy-Based Anion Conductive Membranes for Alkaline Membrane Fuel Cells. *J Memb Sci* **2010**, *350* (1–2), 286–292. https://doi.org/10.1016/j.memsci.2010.01.003.

(65) Zhu, L.; Zimudzi, T. J.; Li, N.; Pan, J.; Lin, B.; Hickner, M. A. Crosslinking of Comb-Shaped Polymer Anion Exchange Membranes via Thiol-Ene Click Chemistry. *Polym Chem* **2016**, *7* (14), 2464–2475. https://doi.org/10.1039/c5py01911g.

(66) Shirole, A.; Bakvand, P. M.; Jannasch, P. Hydroxide Ion Conducting Membranes Dually Functionalized with Cationic and Zwitterionic Groups. *ACS Appl Energy Mater* **2023**, *6* (13), 7240–7249. https://doi.org/10.1021/acsaem.3c00953.

(67) Ding, L.; Song, X.; Wang, L.; Zhao, Z. Enhancing Proton Conductivity of Polybenzimidazole Membranes by Introducing Sulfonate for Vanadium Redox Flow Batteries Applications. *J Memb Sci* **2019**, *578*, 126–135. https://doi.org/10.1016/j.memsci.2019.02.050.

(68) Xiong, P.; Zhang, L.; Chen, Y.; Peng, S.; Yu, G. A Chemistry and Microstructure Perspective on Ion-Conducting Membranes for Redox Flow Batteries. *Angewandte Chemie - International Edition*. John Wiley and Sons Inc November 15, 2021, pp 24770–24798. https://doi.org/10.1002/anie.202105619.

(69) Chen, Y.; Xiong, P.; Xiao, S.; Zhu, Y.; Peng, S.; He, G. Ion Conductive Mechanisms and Redox Flow Battery Applications of Polybenzimidazole-Based Membranes. *Energy Storage Materials*. Elsevier B.V. March 1, 2022, pp 595–617. https://doi.org/10.1016/j.ensm.2021.12.012.

(70) Aguiar, A. O.; Yi, H.; Asatekin, A. Fouling-Resistant Membranes with Zwitterion-Containing Ultra-Thin Hydrogel Selective Layers. *J Memb Sci* **2023**, *669*. https://doi.org/10.1016/j.memsci.2022.121253.

(71) Bengani, P.; Kou, Y.; Asatekin, A. Zwitterionic Copolymer Self-Assembly for Fouling Resistant, High Flux Membranes with Size-Based Small Molecule Selectivity. *J Memb Sci* **2015**, *493*, 755–765. https://doi.org/10.1016/j.memsci.2015.07.025.

(72) He, M.; Gao, K.; Zhou, L.; Jiao, Z.; Wu, M.; Cao, J.; You, X.; Cai, Z.; Su, Y.; Jiang, Z. Zwitterionic Materials for Antifouling Membrane Surface Construction. *Acta Biomaterialia*. Acta Materialia Inc August 1, 2016, pp 142–152. https://doi.org/10.1016/j.actbio.2016.03.038.

(73) Schlogl, R. *THE SIGNIFICANCE OF CONVECTION IN TRANSPORT PROCESSES ACROSS POROUS MEMBRANES*; 1956.

(74) Lakshminarayanaiah, N. Transport Phenomena in Artificial Membranes. *Chem Rev* **1965**, *65* (5), 491–565. https://doi.org/10.1021/cr60237a001.

(75) Agarwal, C.; Goswami, A. Nernst Planck Approach Based on Non-Steady State Flux for Transport in a Donnan Dialysis Process. *J Memb Sci* **2016**, *507*, 119–125. https://doi.org/10.1016/j.memsci.2016.02.021.

(76) Wang, L.; Magliocca, E.; Cunningham, E. L.; Mustain, W. E.; Poynton, S. D.; Escudero-Cid, R.; Nasef, M. M.; Ponce-González, J.; Bance-Souahli, R.; Slade, R. C. T.; Whelligan, D. K.; Varcoe, J. R. An Optimised Synthesis of High Performance Radiation-Grafted

Anion-Exchange Membranes. *Green Chemistry* **2017**, *19* (3), 831–843. https://doi.org/10.1039/c6gc02526a.

(77) Bruker. *Diff50 Probe*. https://www.bruker.com/en/products-and-solutions/mr/nmr/mr-microsc...

(78) Piotto, M.; Saudek, V.; Sklen~2, V. *Gradient-Tailored Excitation for Single-Quantum NMR Spectroscopy of Aqueous Solutions*; 1992; Vol. 2.

(79) Liu, M.; Mao, X.-A.; Ye, C.; Huang, H.; Nicholson, J. K.; Lindon, J. C. *Improved WATERGATE Pulse Sequences for Solvent Suppression in NMR Spectroscopy*; 1998; Vol. 132.

(80) Evilia, R. F. Quantitative NMR Spectroscopy. *Analytical Letters*. 2001, pp 2227–2236. https://doi.org/10.1081/AL-100107290.

(81) Li, J.; Wilmsmeyer, K. G.; Madsen, L. A. Anisotropic Diffusion and Morphology in Perfluorosulfonate Ionomers Investigated by NMR. *Macromolecules* **2009**, *42* (1), 255–262. https://doi.org/10.1021/ma802106g.

(82) Kerssebaum, R.; Salnikov, G. *DOSY and Diffusion by NMR A Tutorial for TopSpin 2.0*; 2002.

(83) Sanders, K. J.; Aguilera, A. R.; Keffer, J. R.; Balcom, B. J.; Halalay, I. C.; Goward, G. R. Transient Lithium Metal Plating on Graphite: Operando 7Li Nuclear Magnetic Resonance Investigation of a Battery Cell Using a Novel RF Probe. *Carbon N Y* **2022**, *189*, 377–385. https://doi.org/10.1016/j.carbon.2021.12.082.